

# H $\alpha$ kinematics of the *Spitzer* Infrared Nearby Galaxies Survey – II\*

I. Dicaire,<sup>1</sup>† C. Carignan,<sup>1</sup>†‡ P. Amram,<sup>2</sup>‡ O. Hernandez,<sup>1</sup>‡ L. Chemin,<sup>3</sup> O. Daigle,<sup>1,2</sup>‡ M.-M. de Denus-Baillargeon,<sup>1,4</sup> C. Balkowski,<sup>3</sup> A. Boselli,<sup>2</sup> K. Fathi<sup>5</sup> and R. C. Kennicutt<sup>6</sup>

<sup>1</sup>Laboratoire d’Astrophysique Expérimentale, Observatoire du mont Mégantic & Département de physique, Université de Montréal, CP 6128, succ. centre ville, Montréal, Québec, Canada H3C 3J7

<sup>2</sup>Laboratoire d’Astrophysique de Marseille, Observatoire Astronomique Marseille-Provence, Université de Provence & CNRS, 2 place Le Verrier, 13248 Marseille Cedex 4, France

<sup>3</sup>Observatoire de Paris, section Meudon, GEPI, CNRS-UMR 8111 & Université Paris 7, 5 Pl. Janssen, 92195 Meudon, France

<sup>4</sup>Institut Fresnel, CNRS & Universités Aix Marseille, 13397 Marseille Cedex 20, France

<sup>5</sup>Instituto de Astrofísica de Canarias C/ Via Lactea, s/n E38205 – La Laguna, Tenerife, Spain

<sup>6</sup>Institute of Astronomy, University of Cambridge, Madingley Road, Cambridge CB3 0HA

Accepted 2007 December 14. Received 2007 December 10; in original form 2007 October 30

## ABSTRACT

This is the second part of an H $\alpha$  kinematics follow-up survey of the *Spitzer* Infrared Nearby Galaxies Survey (SINGS) sample. The aim of this paper is to shed new light on the role of baryons and their kinematics and on the dark/luminous matter relation in the star-forming regions of galaxies, in relation with studies at other wavelengths. The data for 37 galaxies are presented. The observations were made using Fabry–Perot interferometry with the photon-counting camera FaNTOMM on four different telescopes, namely the Canada–France–Hawaii 3.6-m, the ESO La Silla 3.6-m, the William Herschel 4.2-m and the Observatoire du mont Mégantic 1.6-m telescopes. The velocity fields are computed using custom IDL routines designed for an optimal use of the data. The kinematical parameters and rotation curves are derived using the GIPSY software. It is shown that non-circular motions associated with galactic bars affect the kinematical parameters fitting and the velocity gradient of the rotation curves. This leads to incorrect determinations of the baryonic and dark matter distributions in the mass models derived from those rotation curves.

**Key words:** surveys – instrumentation: interferometers – techniques: radial velocities – galaxies: ISM – galaxies: kinematics and dynamics – dark matter.

## 1 INTRODUCTION

Understanding star formation mechanisms and their physical connection to the interstellar medium (ISM) properties of galaxies is crucial for resolving astrophysical issues such as the physical nature of the Hubble sequence, the nature and triggering of starbursts,

and the interpretation of observations of the high-redshift universe. These scientific objectives constitute the core science programme of the *Spitzer* Infrared Nearby Galaxies Survey (SINGS) (Kennicutt et al. 2003). Since the science drivers of the project are dependent of many variables, the SINGS project requires a comprehensive set of data including infrared (IR) imaging and spectroscopic data, broadband imaging in the visible and near-IR as well as ultraviolet (UV) imaging and spectrophotometry. The *Spitzer* data and ancillary observations of the SINGS galaxies will also provide valuable tools for understanding the physics of galaxy formation and evolution.

The formation of individual stars from the collapse of dense molecular clouds is relatively well known, e.g. the intensity of star formation is strongly correlated with the column density of gas and stars (Kennicutt 1998b). However, the large-scale processes driving star formation are still poorly understood. For instance, the effect of gas dynamics on the regulation of star formation is somewhat unknown. Since young stars are often associated with spiral arms, it is thought that protostars are formed from compressed gas along

\*Based on observations made with the ESO 3.60-m telescope at La Silla Observatories under programme ID 076.B-0859 and on observations obtained at the Canada–France–Hawaii Telescope (CFHT) which is operated by the National Research Council of Canada, the Institut National des Sciences de l’Univers of the Centre National de la Recherche Scientifique of France and the University of Hawaii.

†E-mail: isabelle@astro.umontreal.ca (ID); claude.carignan@umontreal.ca (CC)

‡Visiting Astronomer, Canada–France–Hawaii Telescope, operated by the National Research Council of Canada, the Centre National de la Recherche Scientifique de France and the University of Hawaii.

large-scale shock fronts. Moreover, the star formation history varies greatly along the Hubble sequence. Elliptical galaxies, being gravitationally supported by velocity dispersion, have exhausted their gas reservoir and hence star-forming processes have ceased (Kennicutt 1998a). Nevertheless, some elliptical galaxies having a rotating disc are still forming stars (e.g. NGC 2974, Jeong et al. 2007). Spiral galaxies, on the other hand, continue to form stars and are supported by rotation. Understanding the effect of gas dynamics on star formation would certainly help improving our understanding of galaxy formation. Indeed, a Schmidt law modulated by rotation seems to better fit the data than a simple (gas column density) Schmidt law (Kennicutt 1989; Martin & Kennicutt 2001; Boissier et al. 2003).

This paper presents the second part of an H $\alpha$  kinematics survey of the SINGS galaxies. The 37 galaxies showing H $\alpha$  emission were observed by means of Fabry–Perot (FP) interferometry. The paper is organized as follows. Section 2 describes the composition of the SINGS sample and the hardware used for the observations. The data reduction process, using a custom IDL pipeline designed for an optimal use of the data, is introduced in Section 3. In Section 4, the details of the kinematical analysis that has been done on the SINGS galaxies are described. Section 5 presents the observational results in the form of velocity fields, monochromatic maps, position–velocity (PV) diagrams, and rotation curves. In Section 6, the effect of the bar on the observed kinematics is discussed. Finally, the scientific applications of the kinematical results presented in this paper are reviewed in Section 7.

## 2 OBSERVATIONS

### 2.1 The sample

The sample, as described by Kennicutt et al. (2003), is composed of 75 nearby ( $\Delta < 30$  Mpc, for  $H_0 = 70 \text{ km s}^{-1} \text{ Mpc}^{-1}$ ) galaxies covering, in a 3D parameter space, a wide range of physical properties:

- (i) morphological type: associated with gas fraction, star formation rate (SFR) per unit mass and bulge/disc structure;
- (ii) luminosity: associated with galaxy mass, internal velocity and mean metallicity;
- (iii) Far-IR (FIR)/optical luminosity ratio: associated with dust temperature, dust optical depth, and inclination.

In particular, there are roughly a dozen galaxies in each RC3 type (E–S0, Sa–Sab, Sb–Sbc, Sc–Scd, Sd–Sm, Im–I0) leading to an extensive set of combinations of luminosity and FIR/optical luminosity ratio. In particular, a factor of  $10^5$  in IR luminosity and  $10^3$  in  $L_{\text{FIR}}/L_{\text{opt}}$  is covered by the sample. The 75 galaxies also represent a vast range of other galaxy properties such as nuclear activity, surface brightness, inclination, CO/H $\text{I}$  ratio, spiral arm structure, bar structure and environment. The galaxies were chosen as far as possible from the Galactic plane in order to avoid Galactic extinction and high density of foreground stars.

Since gas fraction is correlated with morphological type (Boselli et al. 2001), not all the 75 galaxies are H $\alpha$  emitters. In fact, H $\alpha$  was not detected for ten galaxies (E–S0 and Irr types), thus kinematical information could not be extracted for those galaxies from emission lines. H $\alpha$  kinematics for 28 galaxies of the SINGS sample have already been published in Daigle et al. (2006a). This paper presents the second part of the follow-up survey, namely the H $\alpha$  kinematics of the remaining 37 galaxies. Table 1 presents the basic galaxy parameters.

### 2.2 Observing runs

The observations have been obtained with the same instrumental set-up consisting of a scanning FP interferometer, an imaging device designed for faint fluxes, and a narrow-band ( $\sim 15 \text{ \AA}$ ) interference filter. For imaging, a photon-counting camera (FaNTOMM) and an Andor commercial (L3CCD) camera were used. Each instrument was attached to a focal reducer at the Cassegrain or Nasmyth focus of the telescope. The focal reducers used were Panoramix at the Observatoire du mont Mégantic (OmM) 1.6-m telescope, Cigale at the European Southern Observatory (ESO) La Silla 3.6-m telescope, MOS/FP at the Canada–France–Hawaii 3.6-m telescope (CFHT), and GHFaS at the William Herschel 4.2-m telescope (WHT). Table 2 describes the various characteristics of the instruments.

The spectral profiles for every pixel in the field of view (FOV) were obtained by scanning the free spectral range (FSR) of the FP. The FSR is the wavelength interval between two adjacent transmission peaks:

$$\text{FSR} = \lambda_0/p, \quad (1)$$

where  $\lambda_0$  is the rest wavelength and  $p$  the interference order. The number of channels needed to scan the FSR must be at least 2.2 times the FP *finesse*  $F$  for a good sampling (Nyquist criteria). The *finesse* is a dimensionless parameter representing the spectral resolving power  $R$  of the scanned line and is related to the full width half-maximum (FWHM) of the transmitted line:

$$F = \frac{R}{p} = \frac{\text{FSR}}{\text{FWHM}}. \quad (2)$$

The FP etalon used for the observations has a high interference order (typically  $p = 765$  at H $\alpha$ ) and is capable of achieving high values for the *finesse* and spectral resolution. A typical observation would be to scan the FP etalon in 48 channels with an exposure time of 15 s per channel, then repeat the process for 15 cycles. However, when the sky transparency is not excellent during an exposure, the etalon is scanned more rapidly with an exposure time of 10 s per channel so that the atmospheric conditions can be averaged out more efficiently. The resulting data cube is a set of interferograms stacked together, where each one represents an image of the object modulated by the interference pattern for a given FP spacing.

The filter set used has 24 narrow-band H $\alpha$  filters covering the galaxies' systemic velocities ranging from  $-300$  to  $100\,000 \text{ km s}^{-1}$ . Sometimes, the filter was tilted by a few degrees to adjust its central wavelength to the Doppler shifted galaxy emission. Narrow-band filters, used to select the proper order that will go through the etalon, allow for the H $\alpha$  emission to pass while at the same time blocking most of the night sky emission.

The photon-counting cameras FaNTOMM I and II (Hernandez et al. 2003) consist of a GaAs Hamamatsu photomultiplier tube having a quantum efficiency of  $\sim 23$  per cent coupled to a Dalsa commercial CCD. The absence of readout noise for this camera enables one to scan very rapidly the FP interferometer whereas CCDs need long exposures to overcome their readout noise. Consequently, FaNTOMM can achieve high signal-to-noise ratios (S/N) and thus is ideal for faint fluxes like the emission found in galaxies (Gach et al. 2002). Additionally, a camera using a low light level CCD (L3CCD) made by Andor Technology was also used as the imaging device. L3CCDs have high quantum efficiency ( $\sim 80$  per cent) and subelectron readout noise ( $\sigma < 0.1 \text{ e}^-$ ). This kind of sensor differs from traditional CCDs in the sense that the signal is amplified before it reaches the output circuitry which is the major source of noise. Gain is created by passing electrons through a multiplication register

**Table 1.** Observational data for the SINGS H $\alpha$  kinematics sample.

Galaxy name	$\alpha$ (J2000) (h m s)	$\delta$ (J2000) ( $^{\circ}$ ' '')	Type RC3	$\Delta^a$ (Mpc)	$D_{25}^{b,i}$ (arcmin)	$B_T^{b,i,c}$	$M_B^{b,i,d}$	$V_{\text{sys}}^e$ (km s $^{-1}$ )
NGC 24	00 09 56.7	-24 57 44	SA(s)c	8.2	5.8	12.19	-17.38	554
NGC 337	00 59 50.3	-07 34 44	SB(s)d	24.7	2.9	12.06	-19.90	1650
NGC 855	02 14 03.6	+27 52 38	E	9.6	2.6	13.30	-16.61	610
NGC 1097	02 46 19.0	-30 16 30	SB(r'1)b	16.9	9.3	10.23	-20.91	1275
NGC 1291	03 17 18.6	-41 06 29	SB(l)0/a	9.7	9.8	9.39	-21.75	839
NGC 1482	03 54 39.3	-20 30 09	SA0	22.0	2.5	13.10	-18.61	1655
NGC 1512	04 03 54.3	-43 20 56	SB(r)ab	10.4	8.9	11.13	-18.96	896
NGC 1566	04 20 00.4	-54 56 16	SAB(rs)	18.0	8.3	10.33	-20.95	1496
NGC 1705	04 54 13.5	-53 21 40	SA0	5.8	1.9	12.77	-16.05	628
Ho II	08 19 05.0	+70 43 12	Im	3.5	7.9	11.10	-16.62	157
DDO 053	08 34 07.2	+66 10 54	Im	3.5	1.5	14.70	-13.02	19
NGC 2841	09 22 02.6	+50 58 35	SA(r)b	9.8	8.1	10.09	-19.87	638
Ho I	09 40 32.3	+71 10 56	IAB(s)m	3.5	3.6	13.00	-14.72	143
NGC 3034	09 55 52.2	+69 40 47	I0	3.5	11.2	9.30	-18.42	203
Ho IX	09 57 32.0	+69 02 45	Im	3.5	2.5	14.30	-13.42	46
NGC 3190	10 18 05.6	+21 49 55	SA(s)a	17.4	4.4	12.12	-19.08	1271
IC 2574	10 28 21.2	+68 24 43	SAB(s)m	3.5	13.2	10.80	-16.92	57
NGC 3265	10 31 06.8	+28 47 47	E	20.0	1.3	13.00	-18.50	1421
Mrk 33	10 32 31.9	+54 24 03	Im	21.7	1.0	13.20	-18.50	1461
NGC 3351	10 43 57.7	+11 42 13	SB(r)b	9.3	7.4	10.53	-19.31	778
NGC 3627	11 20 15.0	+12 59 30	SAB(s)b	8.9	9.1	9.65	-20.10	727
NGC 3773	11 38 13.0	+12 06 43	SA0	18.3	1.2	12.90	-18.40	987
NGC 4254	12 18 49.6	+14 24 59	SA(s)c	20.0	5.4	10.44	-21.07	2407
NGC 4450	12 28 29.6	+17 05 06	SA(s)ab	20.0	5.2	10.90	-20.61	1954
NGC 4559	12 35 57.7	+27 57 35	SAB(rs)cd	11.6	10.7	10.46	-19.86	816
NGC 4594	12 39 59.4	-11 37 23	SA(s)a	13.7	8.7	8.98	-21.70	1091
NGC 4631	12 42 08.0	+32 32 26	SB(s)d	9.0	15.5	9.75	-20.02	606
NGC 4736	12 50 53.0	+41 07 14	SA(r)ab	5.3	11.2	8.99	-19.63	308
DDO 154	12 54 05.2	+27 08 59	IB(s)m	5.4	3.0	13.94	-14.72	376
NGC 4826	12 56 43.7	+21 40 52	SA(rs)ab	5.6	10.0	9.36	-19.38	408
DDO 165	13 06 24.8	+67 42 25	Im	3.5	3.5	12.80	-14.92	37
NGC 5033	13 13 27.5	+36 35 38	SA(s)c	13.3	10.7	10.75	-19.87	875
NGC 5408	14 03 20.9	-41 22 40	IB(s)m	4.5	1.6	12.20	-16.07	509
NGC 5474	14 05 01.6	+53 39 44	SA(s)cd	6.9	4.8	11.28	-17.91	273
NGC 6822	19 44 56.6	-14 47 21	IB(s)m	0.6	15.5	9.31	-14.58	-57
NGC 7552	23 16 11.0	-42 34 59	SB(s)ab	22.3	3.4	11.25	-20.49	1585
NGC 7793	23 57 49.8	-32 35 28	SA(s)d	3.2	9.3	9.63	-17.90	230

<sup>a</sup> $\Delta$ : distance. Taken from Kennicutt et al. (2003). <sup>b</sup> $D_{25}^{b,i}$ : apparent major diameter at the 25 mag arcsec $^{-2}$  in B. Taken from the RC3. <sup>c</sup> $B_T^{b,i}$ : total apparent magnitude in B. Taken from the RC3. <sup>d</sup> $M_B^{b,i}$ : total absolute magnitude in B. Calculated from  $\Delta$  and  $B_T^{b,i}$ . <sup>e</sup> $V_{\text{sys}}$ : systemic velocity. Taken from Kennicutt et al. (2003).

**Table 2.** Telescope and instrument characteristics.

Telescope	Instrument	Pixel size (arcsec)	FOV (arcmin)
OmM	FaNTOMM	1.61	19.43
OmM	FaNTOMM II	1.54	18.55
OmM	L3CCD	1.07	12.89
ESO	FaNTOMM	0.42	5.02
CFHT	FaNTOMM	0.48	5.84
WHT	GHafas	0.40	4.82

where an electron will create a second one by avalanche multiplication. More details about the L3CCD can be found in Daigle et al. (2004) and Daigle, Carignan & Blais-Ouellette (2006c).

The observations of the sample were spread over nine different observing runs over a three year period. Five runs took place at the OmM 1.6-m telescope where FaNTOMM is a permanent instrument. A second-generation instrument, called FaNTOMM II, has been

built recently and was tested successfully on the faint dwarf galaxy DDO 154 during one of these runs. Also, a new instrument for the La Silla NTT is under development and regarding this matter, the L3CCD camera was used to test its capabilities on very faint fluxes like galaxies. Therefore, four galaxies were observed with this camera during the same run at the OmM Observatory. Two runs took place at the ESO La Silla 3.6-m telescope and one at the CFHT 3.6-m telescope, both where FaNTOMM I is a visitor instrument. A last observing run took place at the WHT 4.2-m telescope with the new instrument GHafas (Carignan et al. 2007). The FP observations parameters for each galaxy can be found in Table 3.

### 3 DATA REDUCTION

This section introduces the few steps towards obtaining radial velocities (RVs) and monochromatic maps from raw interferograms. In particular,

- (i) wavelength calibration;

**Table 3.** Journal of the FP observations.

Galaxy	Date	$\lambda_c^a$	FWHM <sup>b</sup>	$T_{\max}^c$	$t_{\text{exp}}^d$	$t_{\text{ch}}^e$	$p^f$	FSR <sup>g</sup>	$F^h$	$R^i$	$n_{\text{ch}}^j$	step $\lambda^k$
NGC 24 <sup>l</sup>	2005/11/04	6581	19.8	60	150	2.50	765	392	19.7	15071	60	0.14
NGC 337 <sup>l</sup>	2005/11/02	6598	18.2	73	150	2.50	765	392	20.5	15657	60	0.14
NGC 855 <sup>m</sup>	2003/11/27	6584	15.5	74	190	4.75	609	492	13.2	8010	40	0.27
NGC 1097 <sup>l</sup>	2005/11/07	6598	18.2	73	470	7.83	765	392	20.0	15321	60	0.14
NGC 1291 <sup>l</sup>	2005/11/06	6584	15.5	74	385	6.42	765	392	20.5	15669	60	0.14
NGC 1482 <sup>l</sup>	2005/11/08	6608	16.2	69	115	1.92	765	392	20.3	15561	60	0.14
NGC 1512 <sup>l</sup>	2005/11/03	6584	15.5	74	740	2.67	765	392	17.5	13389	60	0.14
NGC 1566 <sup>l</sup>	2005/11/02	6598	18.2	73	150	2.50	765	392	20.7	15864	60	0.14
NGC 1705 <sup>l</sup>	2005/11/03	6581	19.8	60	130	2.17	765	392	20.0	15282	60	0.14
Ho II <sup>m</sup>	2005/02/05	6563	30.4	80	204	4.25	765	392	17.7	13527	48	0.18
DDO 053 <sup>n</sup>	2006/04/07	6563	30.4	80	96	2.00	765	392	18.1	13885	48	0.18
NGC 2841 <sup>m</sup>	2005/02/03	6584	15.5	74	240	5.00	765	392	12.7	9731	48	0.18
Ho I <sup>n</sup>	2006/04/05	6563	30.4	80	176	3.67	765	392	14.2	10869	48	0.18
NGC 3034 <sup>m</sup>	2007/03/01	6581	19.8	60	384	8.00	765	392	17.2	13181	48	0.18
Ho IX <sup>m</sup>	2005/05/10	6563	30.4	80	228	4.75	765	392	15.9	12185	48	0.18
NGC 3190 <sup>m</sup>	2004/11/03	6598	18.2	73	144	3.00	765	392	15.6	11905	48	0.18
IC 2574 <sup>m</sup>	2005/02/03	6563	30.4	80	180	3.75	765	392	16.6	12713	48	0.18
NGC 3265 <sup>m</sup>	2007/03/01	6598	18.2	73	100	2.08	765	392	18.8	14396	48	0.18
Mrk 33 <sup>n</sup>	2006/04/08	6598	18.2	73	48	1.00	765	392	16.7	12798	48	0.18
NGC 3351 <sup>m</sup>	2005/02/03	6584	15.5	74	156	3.25	765	392	18.0	13750	48	0.18
NGC 3627 <sup>m</sup>	2005/02/06	6584	15.5	74	144	3.00	765	392	16.6	12670	48	0.18
NGC 3773 <sup>n</sup>	2006/04/08	6584	15.5	74	76	1.58	765	392	17.2	13127	48	0.18
NGC 4254 <sup>m</sup>	2005/02/14	6621	18.0	68	240	5.00	765	392	17.4	13825	48	0.18
NGC 4450 <sup>l</sup>	2002/04/07	6607	12.0	69	60	2.50	793	381	12.1	4604	24	0.35
NGC 4559 <sup>m</sup>	2005/02/06	6584	15.5	74	408	8.50	765	391	16.5	12631	48	0.18
NGC 4594 <sup>o</sup>	2007/07/05	6585	15.5	75	64	5.00	765	392	16.5	12623	48	0.18
NGC 4631 <sup>m</sup>	2005/02/01	6584	15.5	74	180	3.75	765	392	18.0	13757	48	0.18
NGC 4736 <sup>m</sup>	2005/05/11	6563	30.4	80	216	4.50	765	392	16.7	12745	48	0.18
DDO 154 <sup>m</sup>	2007/02/22	6581	19.8	60	320	8.00	765	392	17.1	13097	40	0.21
NGC 4826 <sup>n</sup>	2006/04/07	6563	30.4	80	128	2.67	765	392	17.2	13121	48	0.18
DDO 165 <sup>n</sup>	2006/04/06	6563	30.4	80	172	3.58	765	392	17.1	13091	48	0.18
NGC 5033 <sup>m</sup>	2005/05/10	6584	15.5	74	460	9.58	765	392	16.7	12782	48	0.18
NGC 5408 <sup>n</sup>	2006/04/07	6581	19.8	60	108	2.25	765	392	17.1	13083	48	0.18
NGC 5474 <sup>m</sup>	2007/02/28	6581	19.8	60	108	2.25	765	392	17.2	13157	48	0.18
NGC 6822 <sup>l</sup>	2005/11/08	6563	30.4	80	60	1.00	765	392	19.8	15121	60	0.14
NGC 7552 <sup>l</sup>	2005/11/02	6598	18.2	73	120	2.00	765	392	19.8	15160	60	0.14
NGC 7793 <sup>l</sup>	2005/11/08	6563	30.4	80	100	1.67	765	392	19.7	15040	60	0.14

<sup>a</sup> $\lambda_c$ : non-tilted filter central wavelength at 20°C (in Å). <sup>b</sup>FWHM: non-tilted filter full width half-maximum at 20°C (in Å). <sup>c</sup> $T_{\max}$ : non-tilted filter transmission at  $\lambda_c$  and at 20°C (in per cent). <sup>d</sup> $t_{\text{exp}}$ : total exposure time (in min). <sup>e</sup> $t_{\text{ch}}$ : total exposure time per channel (in min). <sup>f</sup> $p$ : interference order at H $\alpha$ . <sup>g</sup>FSR: free spectral range at H $\alpha$  (in km s $^{-1}$ ). <sup>h</sup> $F$ : finesse. <sup>i</sup> $R$ : resolution according to the finesse. <sup>j</sup> $n_{\text{ch}}$ : number of FP channels. <sup>k</sup>step  $\lambda$ : wavelength difference between channels (in Å). <sup>l</sup>ESO: European Southern Observatory, La Silla, Chile, 3.6-m telescope. <sup>m</sup>OMM: Observatoire du mont Mégantic, Québec, Canada, 1.6-m telescope. <sup>n</sup>CFHT: Canada–France–Hawaii Telescope, Hawaii, USA, 3.6-m telescope. <sup>o</sup>WHT: William Herschel Telescope, La Palma, Spain, 4.2-m telescope.

- (ii) spectral smoothing and sky emission subtraction;
- (iii) adaptive spatial binning and map extraction;
- (iv) WCS astrometry.

For a more complete description of the data reduction steps, we refer to Hernandez et al. (2005a), Daigle et al. (2006a,b) and Chemin et al. (2006a). The software used can be found at <http://www.astro.umontreal.ca/fantomm/reduction>.

### 3.1 Wavelength calibration

The raw data cube, obtained during an acquisition, must be wavelength corrected since the transmitted wavelength  $\lambda$  is a function of the angle  $\theta$  of the incoming light beam:

$$p\lambda = 2ne \cos \theta, \quad (3)$$

where  $p$  is the interference order at  $\lambda_0(6562.78 \text{ \AA})$ ,  $n$  is the index of the medium and  $e$  is the distance between the parallel plates of

the etalon. The wavelength calibration is made by scanning the neon line at 6598.95 Å just before and after a three hour acquisition, in the same conditions as the observation itself. This enables one to calculate the phase shift needed to assign a wavelength to a particular FP spacing, for every pixel of the field. This phase map transforms raw interferograms into a wavelength-sorted data cube. Since one can only know the transmitted wavelength value  $\pm$ FSR, an uncertainty remains on the zero-point of the velocity scale. Comparison with other kinematical work will remove this uncertainty. Note that the data cubes are not flux calibrated.

### 3.2 Spectral smoothing and sky emission subtraction

A Hanning smoothing was performed on every spectrum of the wavelength-sorted data cubes in order to remove any artefacts caused by the discrete sampling. After that, the strong night sky emission lines were subtracted. The method used for this is to

reconstruct a sky cube using the sky dominated regions and interpolating it in the galaxy region. This sky cube was then subtracted from the data cube. This method has proven to be very successful at eliminating sky residuals compared with subtracting a median sky spectrum where both spatial and spectral inhomogeneities in the interference filter can lead to high sky residuals.

### 3.3 Adaptive spatial binning and map extraction

In order to increase the S/N in the diffuse and/or faint interstellar regions (e.g. interarm regions) of the observed galaxies, an adaptive spatial binning was applied to the data cubes. This technique is based on Voronoi diagrams where pixels are accreted into bins until the desired S/N ( $\sim 5$ , typically chosen) is reached. In high-intensity emission regions like the galactic centre and spiral arms, the S/N exceeds by far the targeted minimal value and hence the high spatial resolution is maintained. This is an improvement over the usual Gaussian smoothing where the kernel convolution would dilute the signal in high-S/N regions.

Next, the final steps are the integration of the flux under the H $\alpha$  line for every bin, yielding a monochromatic map, and the barycentre computation, yielding a velocity field, following the procedure described by Daigle et al. (2006b). The RVs are given in the heliocentric rest frame. A continuum map and a velocity dispersion map are also computed by the algorithm. The determination of the continuum threshold is a critical step in the data reduction as it defines the position of the barycentre of the line. This is done by iterative procedures.

### 3.4 WCS astrometry

Finally, WCS coordinates are attached to the computed maps using the task koords in the KARMA package (Gooch 1996). No references to the World Coordinate System are obtained during the acquisition and are necessary since the major axes position angle (PA) of the galaxy is field-orientation dependent. Besides, WCS astrometry is needed to combine the H $\alpha$  kinematics with ancillary SINGS surveys. The coordinates are added by comparing positions of stars between a reference file (a red-band DSS image for instance) and the FP non-binned continuum image.

## 4 KINEMATICAL PARAMETERS FITTING

Rotation curves are computed using the task rotcur available in the GIPSY software (Vogelaar & Terlouw 2001). rotcur derives the kinematical parameters for a particular galaxy by fitting tilted rings to the observed velocity field. More precisely, a least-squares fitting is done to the function

$$V_{\text{obs}}(x, y) = V_{\text{sys}} + V_{\text{rot}}(r) \cos \theta \sin i + V_{\text{exp}}(r) \sin \theta \sin i. \quad (4)$$

Here  $V_{\text{obs}}(x, y)$  denotes the RV at the pixel coordinates  $(x, y)$ ,  $V_{\text{sys}}$  the systemic velocity,  $V_{\text{rot}}(r)$  the rotational velocity for the corresponding radius  $r$ ,  $\theta$  the azimuthal angle from the major axis in the plane of the galaxy,  $i$  the inclination angle of the galaxy and  $V_{\text{exp}}$  the expansion velocity. Since GIPSY does not take into account the field rotation of the supplied velocity field with respect to WCS coordinates, the velocity fields were all rotated in order to compute accurate PAs of the kinematical major axis.

Fitting the kinematical parameters was done in a three-step process. First, the systemic velocity  $V_{\text{sys}}$  and the kinematical centre  $(x_{\text{pos}}, y_{\text{pos}})$  are fitted while keeping fixed the inclination  $i$  and PA. The starting parameters used are the photometric  $i$  and PA given by

the HyperLeda catalogue and for  $V_{\text{sys}}$ , the value used for selecting the interference filter. The starting values for the galactic centre are the photometric centre corresponding to the maximum value near the galactic centre in the continuum map for spiral galaxies or in the *Spitzer* 3.6- $\mu\text{m}$  image for distorted and irregular galaxies. Then, a second fitting is done by letting  $i$ , PA and  $V_{\text{rot}}$  vary with radius while keeping fixed the new-found values for  $V_{\text{sys}}$ ,  $x_{\text{pos}}$  and  $y_{\text{pos}}$ . Finally, rotcur is run again, with only  $V_{\text{rot}}$  as the varying parameter. The computed rotation curve is thus derived with fixed kinematical parameters so that the sample could be homogeneous, even though some velocity fields (e.g. NGC 3627) were better modelled with parameters varying with radius.

The ring width used in the fitting procedure was set to be greater than three times the pixel width for a good sampling. The result is 5 arcsec for the OmM observations and 2 arcsec for the ESO, CFHT and WHT observations. Also, additional rotcur runs were done for the approaching and receding sides separately in order to model any asymmetries arising between the two sides. Finally, the expansion velocity  $V_{\text{exp}}$  was fixed to zero for all galaxies, thus assuming pure circular rotation. Letting  $V_{\text{exp}}$  vary with radius did not change significantly the rotation velocities in the computed regions.

Two rotcur parameters remain to be explained, namely the free angle and the weighting function. To diminish the importance of deprojection errors, RVs in an opening angle (called the free angle) of typically  $35^\circ$  about the minor axis were rejected from the least-square fitting and a  $\cos(\theta)$  (where  $\theta = \text{angle from the major axis}$ ) weighting function was applied to give more importance to points near the major axis. Naturally, for more face-on galaxies, the projected velocities along the line of sight possess little information about rotational velocities resulting in large errors for the kinematical parameters.

Afterwards, the GIPSY output was analysed by IDL routines (mainly computing averages and standard deviations). The determination of constant values for  $i$  and PA throughout the galaxy is performed by eliminating radii where non-circular motions and warps can occur. For a non-barred galaxy, this results in discarding radii located in the galactic centre and outer spiral arms where one usually finds a substantial scatter in  $i$  and PA values. For a barred galaxy, this is complicated by the fact that important non-circular motions are present in the bar region, therefore this region was excluded from the fit. Also, for barred and non-barred galaxies, rings containing too few points or dominated by one side of the galaxy were discarded.

## 5 RESULTS

This section presents the H $\alpha$  monochromatic and RV maps as well as the rotation curves for each galaxy in order of increasing right ascension. Appendix A briefly describes the observed kinematics for each galaxy of the sample. In Appendix B, four images per galaxy are first shown: DSS blue image when available (top left-hand panel), *Spitzer* 3.6- $\mu\text{m}$  image (top right-hand panel), H $\alpha$  monochromatic image (middle left-hand panel) and the corresponding H $\alpha$  velocity field (middle right-hand panel). The blue images show the intermediate ( $\sim 10^9$  yr) stellar population and the 3.6- $\mu\text{m}$ -old stellar population, tracer of the total mass of galaxies, while the H $\alpha$  monochromatic maps show the gas ionized by massive ( $M > 8 M_\odot$ ), young ( $\sim 10^6$  yr) OB stars (Kennicutt 1998a; Boselli et al. 2001). These four maps are WCS oriented and represent the same FOV. For each galaxy, the FOV is adjusted so that the H $\alpha$  morphology and kinematics as well as the large-scale stellar morphology are displayed

**Table 4.** Photometric and kinematical parameters.

Galaxy name	Photometric		Kinematic	
	PA	$i$	PA	$i$
NGC 24	225	78	$226 \pm 1$	$75 \pm 3$
NGC 337	130	53	$121 \pm 5$	$52 \pm 6$
NGC 1097	140	37	$133 \pm 1$	$55 \pm 1$
NGC 1512	253	65	$260 \pm 1$	$35 \pm 14$
NGC 1566	212	56	$214 \pm 2$	$32 \pm 14$
NGC 2841	147	68	$150 \pm 1$	$70 \pm 1$
NGC 3351	193	42	$193 \pm 1$	$41 \pm 2$
NGC 3627	173	57	$173 \pm 7$	$65 \pm 7$
NGC 4254	45	28	$69 \pm 3$	$31 \pm 6$
NGC 4450	355	43	$353 \pm 5$	$49 \pm 17$
NGC 4559	330	67	$323 \pm 3$	$68 \pm 5$
NGC 4736	285	35	$292 \pm 2$	$36 \pm 7$
DDO 154	219	48	$236 \pm 17$	$59 \pm 32$
NGC 4826	295	60	$291 \pm 1$	$53 \pm 1$
NGC 5033	351	66	$353 \pm 2$	$71 \pm 2$
NGC 7793	264	53	$277 \pm 3$	$47 \pm 9$

with great detail. The maps and the rotation curves can be found at <http://www.astro.umontreal.ca/fantomm/singsII/>.

Moreover, a PV diagram is provided for each galaxy when the extraction of the kinematical parameters was possible. They represent a slice in the data cube along the kinematical major axis. The black line, superposed on the diagrams, represents a cut in the model velocity field. A data cube slice along the kinematical major axis showing a rotation curve which superposes well on the velocities of the maximum intensity of the ionized gas emission implies that there are no significant non-circular motions nor any kinematical twist. Lastly, rotation curves can be found in Appendix C. The definition of the errors used is either the largest velocity difference between both sides and the approaching or receding side separately, or the rotcur intrinsic error if it is greater.

The kinematical parameters inclination and PA found by the technique described in Section 4 are presented in Table 4. Fig. 1 compares the kinematical parameters with respect to the photometric values. As expected, the agreement is better for the PAs than for the inclinations. The two points that stand out are NGC 1512 ( $i_{\text{phot}} = 65^\circ$  and  $i_{\text{kin}} = 35^\circ$ ) and NGC 1566 ( $i_{\text{phot}} = 56^\circ$  and  $i_{\text{kin}} = 32^\circ$ ). In both cases, the explanation is quite clear: the photometric parameters are mainly representative of the bar which contributes a large part of the light resulting in more edge-on values. Only looking at the B or 3.6- $\mu\text{m}$  images in Figs B7 and B8, one can see that the outer isophotes are much more face-on.

Finally, on the overall 37 galaxies exhibiting H $\alpha$  emission, it was not possible to extract rotation curves for 21 of them due to either poor spatial coverage, absence of large-scale rotation or extremely perturbed discs.

## 6 DISCUSSION

In this paper, the rotation curves given in Appendix C were obtained from the kinematical parameters derived using tilted-ring models which assume pure circular motions. Even if we tried to avoid the zones obviously affected by non-circular motions, there is still considerable work needed to extract rotation curves that are truly representative of the mass distribution, and can be used for mass modelling purposes. This is especially true for barred systems, which account for about one-third of the galaxies in Table 1.

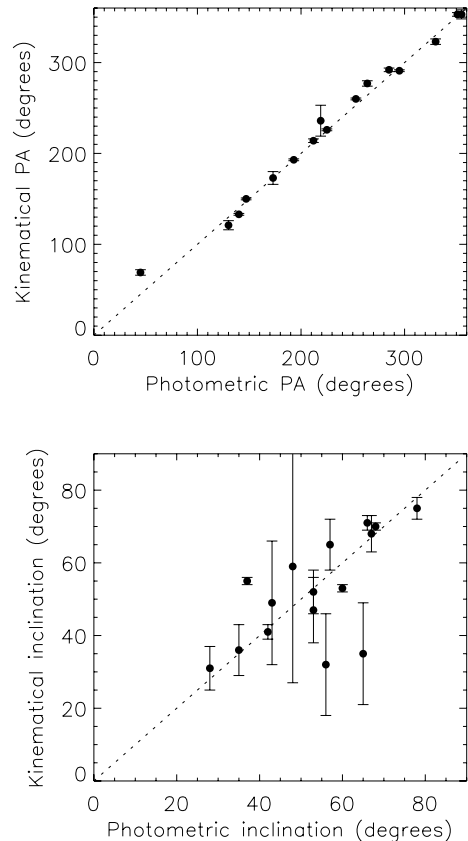


**Figure 1.** Comparison between photometric and kinematical parameters. Top: PA. Bottom: inclination. The dotted line represents agreeing parameters.

The idea behind obtaining an accurate determination of the gravitational potential is correlated with the dark halo modelling. For instance, there has been significant debate about the shape of dark matter density profiles, especially regarding their inner slope. Based on cosmological  $N$ -body simulations (Navarro et al. 1996, 1997, hereafter collectively NFW), the dark matter halo profile appears to be independent of halo mass with an inner logarithmic slope equal to  $-1$ . Nevertheless, recent higher resolution simulations suggest that the density profiles do not converge to a single power law at small radii. At the smallest resolved scales (0.5 per cent of the virial radius), profiles usually have slopes between  $-1$  and  $-1.5$  (Moore et al. 1999; Ghigna et al. 2000; Jing & Suto 2000; Fukushige & Makino 2001; Klypin et al. 2001; Power et al. 2003; Navarro et al. 2004; Diemand et al. 2004).

In addition, all simulations find density profiles that are inconsistent with the isothermal profile found in observations. In the outer regions, the determination of the dark halo slope based on mapping the outer density profile of galaxies is difficult, owing mainly to a lack of mass tracers at large radii. In the inner regions, the unknown value of the stellar mass-to-light ratio further complicates the determination of the mass distribution. This has led to dedicated analysis on dwarf and low surface brightness (LSB) galaxies that are believed to be dark matter dominated at all radii (de Blok & McGaugh 1997; Carignan & Beaulieu 1989; Swaters 1999). It has been suggested that rotation curves of dwarf and LSB galaxies rise less steeply than predicted by numerical simulations based on the cold dark matter paradigm (Moore 1994; Flores & Primack 1994; de Blok & McGaugh 1997; McGaugh & de Blok 1998; de Blok et al. 2001a, b).

However, a number of observational uncertainties cast doubt over these early claims. These include beam smearing for H $\alpha$  rotation curves (Swaters et al. 2000; van den Bosch et al. 2000), high inclination angles and H $\alpha$  long-slit alignment errors (Swaters et al. 2003a) and non-circular motions close to the centre of galaxies (Swaters et al. 2003b). Many of these uncertainties can be quantified or eliminated by measuring high-resolution 2D velocity fields (Barnes et al. 2004). At optical wavelengths, these can be obtained via FP interferometry (e.g. Blais-Ouellette et al. 1999) or integral field spectroscopy (e.g. Andersen & Bershady 2003; Courteau et al. 2003).

There are ways to extract the true kinematics that reflect the gravitational potential. One is to derive the potential directly from the 2D velocity field or the 3D data cube (this is work in preparation). The other way is to derive the bar parameters using the *Spitzer* images, compare with numerical simulations, and apply the necessary corrections for, e.g. the streaming motions induced by the bars (see Hernandez 2005b; Perez, Fux & Freeman 2004). This detailed work will be done in another paper (Hernandez et al., in preparation), but we can illustrate what needs to be done by using three of the barred systems in our sample.

The galaxy NGC 3351, better known as Messier 95, is a SB $b$  galaxy, member of the Leo group. Situated at a distance of 9.3 Mpc, this starburst galaxy has a large-scale stellar bar which has a deprojected value of 47 arcsec for the semimajor axis (Martin 1995). Outside this bar, the H $\alpha$  velocity field is fairly regular and the kinematical PA and inclination found by GIPSY agree well with the photometric values. Thus, the gas outside the bar is thought to be in circular orbits so that the rotation curve represents accurately the kinematics of this galaxy. The small deviations from circular motions are due to streaming along the inner ring. The H $\alpha$  rotation curve shows a more or less constant velocity beginning at the end of the stellar bar with peaks corresponding to the 70 arcsec inner ring. Fig. 2 displays the tilted-ring model results and one can see, outside the bar, the fairly regular values for the PA and inclination as a function of the radius.

However, inside the large-scale bar, the H $\alpha$  velocity field shows the perturbed kinematics expected for this barred system. The

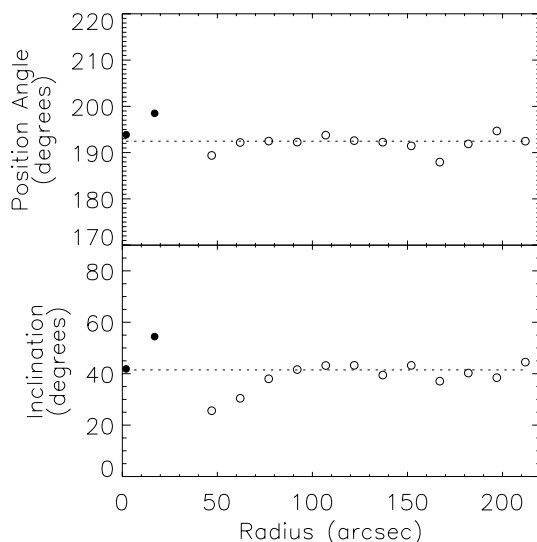


**Figure 2.** Tilted-ring model for NGC 3351. The dotted line shows the fitted PA ( $193^\circ$ ) and inclination ( $41^\circ$ ). The stellar bar ends at a radius of 47 arcsec. So, the filled circles give the values inside the bar and the empty circles the values outside the bar region.

twisted isovelocity contours indicate that a pure circular rotation model will present a poor fit to the data and hence kinematical information extracted in this region will be incorrect. This is illustrated in Fig. 2 where the filled circles represent the values computed in the bar region. It is thus imperative to take into account the bar location when deriving kinematical parameters.

Furthermore, bar modelling is crucial in order to properly compute the rotation curve in this region. Numerical computations were performed with GADGET, a tree-based  $N$ -body + SPH code developed by Springel, Yoshida & White (2001). For the needs of the simulations, an initial stellar population is set up to reproduce a disc galaxy with an already formed bulge. The initial positions and velocities of the stellar particles are drawn from a superposition of two axisymmetric Miyamoto–Nagai discs (Miyamoto & Nagai 1975) of mass, respectively,  $10^{10}$  and  $10^{11} \text{ M}_\odot$ , of scalelengths, respectively, 1 and 3.5 kpc and common scaleheight of 0.5 kpc. Velocity dispersions are computed solving numerically the Jeans equations. The total number of stellar particles is  $1.1 \times 10^6$ . The run includes a dark halo made of  $2.2 \times 10^6$  live particles distributed in a Plummer sphere of scalelength 50 kpc and of mass, respectively,  $2.42$  and  $6.46 \times 10^{11} \text{ M}_\odot$ . The total mass of the gas is  $0.11 \times 10^{11} \text{ M}_\odot$ . Finally, the total mass of the simulated galaxy is  $7.67 \times 10^{11} \text{ M}_\odot$ .

Numerical simulations of the kinematical effect of the bar are shown in Fig. 3. The input model for the galaxy is pure rotation and the corresponding rotation velocities along the major and minor axes are shown in faint blue and green lines. Afterwards, the code simulates galaxy evolution where a bar is developing. The difference in orientation between the major axis and the bar corresponds to different evolving times which are given in units of millions years. For NGC 3351, the kinematical PA ( $\text{PA}_{\text{kin}} = 193^\circ$ ) is almost perpendicular to the bar, with  $\text{PA}_{\text{bar}} = 113^\circ$  using the value found by Menéndez-Delmestre et al. (2007). The results of the simulations are shown in the form of RV maps and stellar densities superposed. For an  $80^\circ$  difference between the major axis and the bar PAs, the overall effect is an artificial increase in the velocity gradient. This can be explained by gas moving along  $x1$  orbits (parallel to the bar) where the velocity is greater at the perigalacticon (near the centre) than at the apogalacticon (near the end of the bar). The true kinematics of this galaxy will therefore be obtained by correcting this artificial increase in the velocity gradient. Until then, rotation velocities inside the bar region are not given for the final rotation curve. See the galaxy description in Appendix A for additional evidences of non-circular motions.

Another galaxy displaying a perturbed velocity field is NGC 337. This asymmetric SB $d$  galaxy features an off-centre stellar bar having a PA of  $162^\circ$  and a deprojected value of 35 arcsec for the bar semimajor axis (Menéndez-Delmestre et al. 2007). Since the photometric major axis of this galaxy is  $130^\circ$ , the bar has an intermediate orientation with respect to the major axis. Numerical simulations have been done for this bar position and the results are illustrated in the middle panel of Fig. 3. The simulated velocity field displays the characteristic Z-shape of the isocontours similar to what is seen in the H $\alpha$  velocity map. One characteristic is the velocity gradient along the minor axis (green line in Fig. 3). Another feature is the relative agreement between the input rotation velocities (faint blue line) and the computed ones (triangle symbols show averaged red and blue points calculated using the method presented in Section 4). The rotation curve in the bar region is thus provided for this galaxy since these perturbations are confined to the minor axis which is excluded from the fit. The tilted-ring model for this galaxy, presented in Fig. 4, illustrates the small differences for the fitted

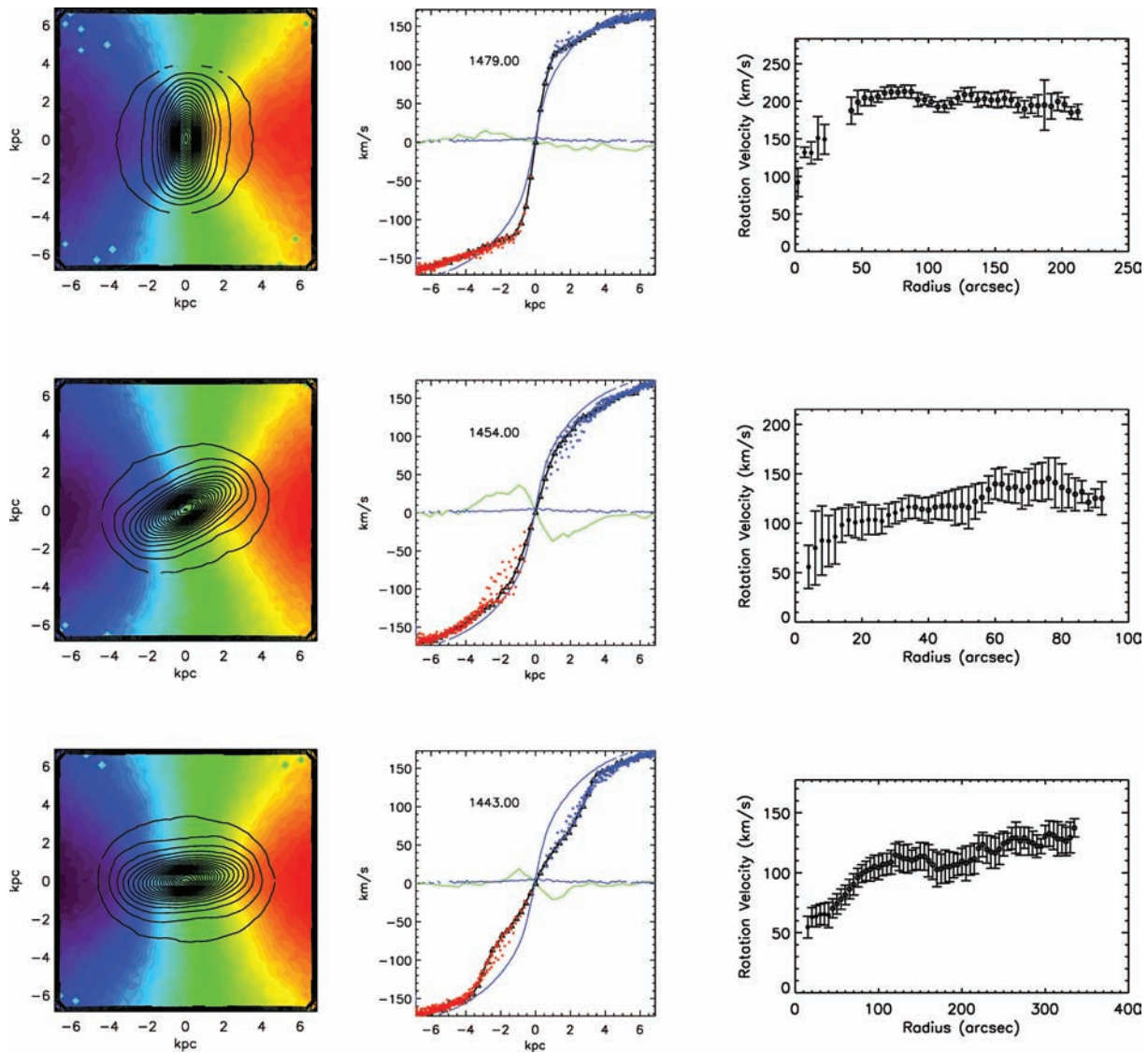


**Figure 3.** Three different bar orientations with respect to the major axis. Top: NGC 3351, perpendicular position. Middle: NGC 337, intermediate position. Bottom: NGC 4559, parallel position. Left-hand panels: Density contours of the bar superposed on the velocity field of the model. Middle panels: The thin blue and green lines represent the rotation velocities along the major and minor axes, respectively, for an input model with pure rotation. The dots (blue for the approaching side and red for the receding side) represent the observed velocities. Right-hand panels: Rotation curves derived in this study.

values between the bar region (filled circles) and spiral arms (open circles).

After having completed the kinematical fitting procedure, one can look at the *Spitzer* IRAC 3.6- $\mu$ m image in order to compare the bar location with the velocity residuals. Since the eastern side is approaching and the western side is receding, the spiral arms seem to be trailing in an anticlockwise direction. The velocity residuals from the pure circular rotation model indicate positive residuals east of the bar as well as negative residuals on the southern end of the bar, suggesting an inflow of gas towards the bar.

Two other barred galaxies having a bar orientation intermediate to the major axis are NGC 1566 and 3627, but their Seyfert activity and warped disc, respectively, make difficult the kinematical analysis regarding the effects of the bar. Their rotation curves are provided at the end of this paper.

Finally, the last barred system discussed in this paper is NGC 4559, an SABcd galaxy having a small bar roughly aligned

with the major axis ( $\text{PA}_{\text{bar}} \sim 340^\circ$  versus  $\text{PA}_{\text{kin}} = 323^\circ$ ). Numerical simulations have been done for a bar parallel to the major axis and are presented in the bottom panel of Fig. 3. The small velocity gradient seen in the PV diagram and in the rotation curve is in agreement with the predicted behaviour seen in the simulation. The rotation velocities are artificially lowered by the radial motions in the bar, resulting in an underestimation of the luminous mass in the central regions. It is thus vital to model the bar in order to determine the accurate mass distribution. The radial mass distribution of the gas was analysed between the three time-steps to verify that modifications of the inner part of the rotation curve was not an effect of migration of the gas during the run.

Further bar modelling enables the bar length to be calculated. Using the Fourier moment analysis on azimuthal profiles derived using *J* and *K* 2MASS images (see Aguerri, Beckman & Prieto 1998; Aguerri et al. 2000), the deprojected value for the bar semi-major axis is  $30 \pm 5$  arcsec. For example, the tilted-ring model for

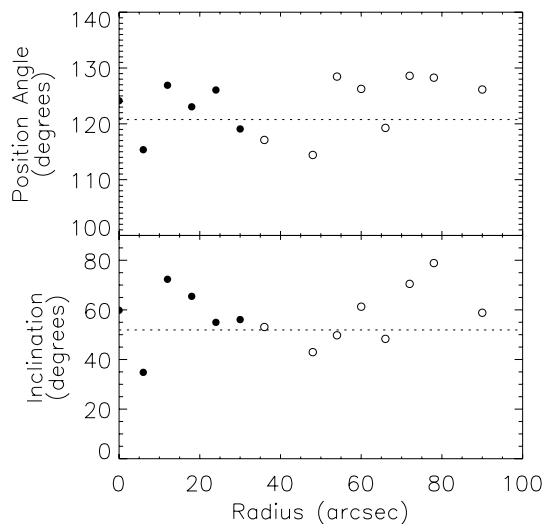


**Figure 4.** Tilted-ring model for NGC 337. The dotted line shows the fitted PA ( $121^\circ$ ) and inclination ( $52^\circ$ ). The stellar bar ends at a radius of 35 arcsec. So, the filled circles give the values inside the bar and the empty circles the values outside the bar region.

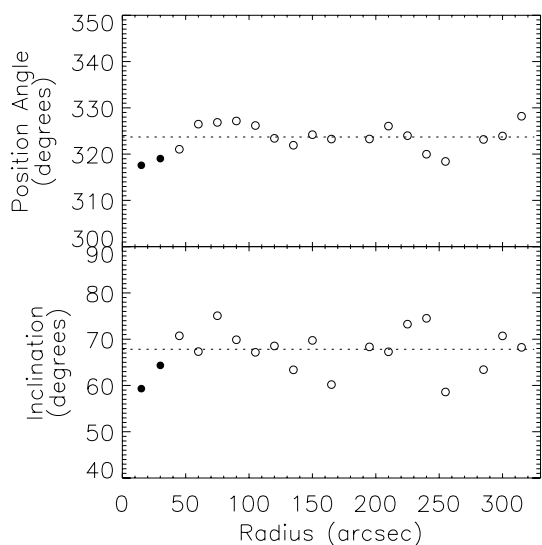


**Figure 5.** Tilted-ring model for NGC 4559. The dotted line shows the fitted PA ( $323^\circ$ ) and inclination ( $68^\circ$ ) values. The stellar bar ends at a radius of  $\sim 30$  arcsec.

NGC 4559 shows that it is difficult to assess which radii are affected by the bar (see Fig. 5). However, the  $\text{H}\alpha$  velocity field displays streaming motions outside the bar as well, therefore the velocities are perturbed to at least a radius of  $\sim 40$  arcsec. Deriving the form of the gravitational potential directly from 2D kinematics and/or using numerical simulations of the bar, are thus essential to perform in order to study properly the mass distribution and solve the dark halo density profile inconsistencies.

## 7 CONCLUSIONS

We have presented in this paper the second and last part of the  $\text{H}\alpha$  kinematics follow-up survey of the SINGS sample. The goal of this kinematical follow-up is to better understand the role of baryons and of the dark/luminous matter relation in star-forming regions of

galaxies. The shape of the velocity field in the central galactic regions, drawn through its  $\text{H}\alpha$  component, is indeed directly related to the baryonic luminous disc and the star formation processes. The SINGS sample will provide a unique opportunity to link the kinematics with numerous observations and studies at other wavelengths.

The data have been obtained from high-resolution FP observations using the FaNTOMM camera and a L3CCD detector. The SINGS sample of galaxies has been observed at the OmM 1.6-m telescope, ESO La Silla 3.6-m telescope, CFHT 3.6-m telescope and WHT 4.2-m telescope. The velocity fields were obtained by using a data reduction pipeline written in IDL and the rotation curves were computed by the rotcur task from the GIPSY software. When fitting the kinematical parameters, care was taken to avoid the zones obviously affected by non-circular motions. However, we have demonstrated that for barred systems, different bar characteristics considerably modify the central velocity gradient of the computed rotation curves in the pure circular rotation hypothesis. Therefore, numerical modelling of barred galaxies is crucial in order to extract rotation curves that are truly representative of the gravitational potential and hence of the mass distribution in those galaxies. In the meantime, the dark matter distribution of the SINGS galaxies, using the rotation curves derived here, will be presented in a forthcoming paper.

Not only will these observations provide the high spatial resolution data needed for constraining the dark matter density profiles of galaxies, but they will be helpful for studying these profiles as a function of morphological type. Furthermore, they will help to delineate the role of gas kinematics in regulating the SFR. For instance, Palouš, Ehlerov & Elmegreen (2002) have argued that the probability of collapse of molecular clouds leading to star formation is greatly enhanced in slowly rotating gas discs compared to high velocity rotation. Moreover, Chemin et al. (2003) and Fathi et al. (2007) have suggested that the star-forming inner and nuclear rings in the nearby galaxies NGC 3627 and 628 (respectively) are driven by a rotating asymmetry because their location in the host disc are in agreement with Lindblad resonances caused by a bar pattern speed. Gas dynamical processes therefore are important in regulating the star formation history of galaxies and the  $\text{H}\alpha$  kinematics presented in this paper will help understanding the star formation processes.

## ACKNOWLEDGMENTS

We would like to thank Jacques Boulesteix, Jean-Luc Gach, Philippe Balard and Olivier Boissin for helping with the instrumentation and part of the observations and the staff of the four Observatories, where the data were obtained, for their continuing support. The William Herschel Telescope is operated on the island of La Palma by the Isaac Newton Group in the Spanish Observatorio del Roque de los Muchachos of the Instituto de Astrofísica de Canarias. We acknowledge support from the Natural Sciences and Engineering Research Council of Canada and the Fonds Québécois de la recherche sur la nature et les technologies. The Digitized Sky Surveys (DSS images) were produced at the Space Telescope Science Institute under US Government grant NAG W-2166. The images of these surveys are based on photographic data obtained using the Oschin Schmidt Telescope on Palomar Mountain and the UK Schmidt Telescope. The plates were processed into the present compressed digital form with the permission of these institutions. The IR images were obtained by the *Spitzer Space Telescope*, which is operated by the Jet Propulsion Laboratory, California Institute of Technology under a contract with NASA.

## REFERENCES

- Afanasiev V. L., Sil'chenko O. K., 1999, AJ, 117, 1725  
 Afanasiev V. L., Sil'chenko O. K., 2005, A&A, 429, 825  
 Agüero E. L., Díaz R. J., Bajaja E., 2004, A&A, 414, 453  
 Aguerri J. A. L., Beckman J. E., Prieto M., 1998, AJ, 116, 2136  
 Aguerri J. A. L., Muñoz-Tuñón C., Varela A. M., Prieto M., 2000, A&A, 361, 841  
 Andersen D. R., Bershady M. A., 2003, ApJ, 599, L79  
 Barbieri C. V., Fraternali F., Oosterloo T., Bertin G., Boomsma R., Sancisi R., 2005, A&A, 439, 947  
 Barnes E. I., Sellwood J. A., Kosowsky A., 2004, AJ, 128, 2724  
 Blais-Ouellette S., Carignan C., Amram P., Côté S., 1999, AJ, 118, 2123  
 Blais-Ouellette S., Amram P., Carignan C., 2001, AJ, 121, 1952  
 Bohuski T. J., Burbidge E. M., Burbidge G. R., Smith M. G., 1972, ApJ, 175, 329  
 Boissier S., Prantzos N., Boselli A., Gavazzi G., 2003, MNRAS, 346, 1215  
 Boselli A., Gavazzi G., Donas J., Scoggio M., 2001, AJ, 121, 753  
 Bosma A., 1981, AJ, 86, 1791  
 Braun R., Walterbos R. A. M., Kennicutt R. C. Jr., 1992, Nat, 360, 442  
 Bridges T. J., Ashman K. M., Zepf S. E., Carter D., Hanes D. A., Sharples R. M., Kavelaars J. J., 1997, MNRAS, 284, 376  
 Bureau M., Carignan C., 2002, AJ, 123, 1316  
 Burstein D., Krumm N., Salpeter E. E., 1987, AJ, 94, 883  
 Buta R., 1988, ApJS, 66, 233  
 Carignan C., Beaulieu S., 1989, ApJ, 347, 760  
 Carignan C., Freeman K. C., 1988, ApJ, 332, L33  
 Carignan C., Puche D., 1990, AJ, 100, 394  
 Carignan C., Purton C., 1998, ApJ, 506, 125  
 Carignan C., Hernandez O., Beckman J. E., Fathi K., 2007, preprint (arXiv:0705.4093)  
 Carter D., Jenkins C. R., 1993, MNRAS, 263, 1049  
 Cayatte V., van Gorkom J. H., Balkowski C., Kotanyi C., 1990, AJ, 100, 604  
 Chemin L., Cayatte V., Balkowski C., Marcellin M., Amram P., van Driel W., Flores H., 2003, A&A, 405, 89  
 Chemin L. et al., 2006a, MNRAS, 366, 812  
 Chemin L., Carignan C., Drouin N., Freeman K. C., 2006b, AJ, 132, 2527  
 Colina L., Garcia Vargas M. L., Mas-Hesse J. M., Alberdi A., Krabbe A., 1997, ApJ, 484, L41  
 Cortea S., Andersen D. R., Bershady M. A., McArthur L. A., Rix H.-W., 2003, ApJ, 594, 208  
 Daigle O., Gach J.-L., Guillaume C., Carignan C., Balard P., Boisin O., 2004, in Garnett J. D., Beletic J. W., eds, Proc. SPIE Vol. 5499, Optical and Infrared Detectors for Astronomy. SPIE, Bellingham, p. 219  
 Daigle O., Carignan C., Amram P., Hernandez O., Chemin L., Balkowski C., Kennicutt R., 2006a, MNRAS, 367, 469  
 Daigle O., Carignan C., Hernandez O., Chemin L., Amram P., 2006b, MNRAS, 368, 1016  
 Daigle O., Carignan C., Blais-Ouellette S., 2006c, in Dorn D. A., Holland A. D., eds, Proc. SPIE Vol. 6276, High Energy, Optical, and Infrared Detectors for Astronomy II. SPIE, Bellingham, p. 62761F  
 de Blok W. J. G., McGaugh S. S., 1997, MNRAS, 290, 533  
 de Blok W. J. G., Walter F., 2000, ApJ, 537, L95  
 de Blok W. J. G., McGaugh S. S., Rubin V. C., 2001a, AJ, 122, 2396  
 de Blok W. J. G., McGaugh S. S., Bosma A., Rubin V. C., 2001b, ApJ, 552, L23  
 Devereux N. A., Kenney J. D., Young J. S., 1992, AJ, 103, 784  
 Diemand J., Moore B., Stadel J., 2004, MNRAS, 353, 624  
 Dumas G., Mundell C., Emsellem E., Nagar N., 2007, MNRAS, 379, 1249  
 Elfhag T., Booth R. S., Hoeglund B., Johansson L. E. B., Sandqvist A., 1996, A&S, 115, 439  
 Fathi K., Storchi-Bergmann T., Riffel R. A., Wing C., Axon D. J., Robinson A., Capetti A., Marconi A., 2006, ApJ, 641, L25  
 Fathi K., Beckman J. E., Zurita A., Relano M., Knapen J. H., Daigle O., Hernandez O., Carignan C., 2007, A&A, 466, 905  
 Flores R. A., Primack J. R., 1994, ApJ, 427, L1  
 Fukushige T., Makino J., 2001, ApJ, 557, 533  
 Gach J.-L. et al., 2002, PASP, 114, 1043  
 Gerin M., Combes F., Nakai N., 1988, A&A, 203, 44  
 Ghigna S., Moore B., Governato, F., Lake G., Quinn T., Stadel J., 2000, ApJ, 544, 616  
 Golla G., Dettmar R.-J., Domgoerden H., 1996, A&A, 313, 439  
 Gooch R. E., 1996, in Jacoby G. H., Barnes J., eds, ASP Conf. Ser. Vol. 101, Astronomical Data Analysis Software and Systems V. Astron. Soc. Pac., San Francisco, p. 80  
 Gordon M. A., 1991, ApJ, 371, 563  
 Hägele G. F., Díaz Á. I., Cardaci M. V., Terlevich E., Terlevich R., 2007, MNRAS, 378, 163  
 Hawarden T. G., van Woerden H., Goss W. M., Mebold U., Peterson B. A., 1979, A&A, 76, 230  
 Haynes M. P., Giovanelli R., Kent B. R., 2007, ApJ, 665, L19  
 Helfer T. T., Thornley M. D., Regan M. W., Wong T., Sheth K., Vogel S. N., Blitz L., Bock D. C.-J., 2003, ApJS, 145, 259  
 Hernandez O., Gach J.-L., Carignan C., Boulesteix J., 2003, in Masanori I., Moorwood A. F. M., eds, Proc. SPIE Vol. 4841, Instrument Design and Performance for Optical/Infrared Ground-based Telescopes. SPIE, Bellingham, p. 1472  
 Hernandez O., Carignan C., Amram P., Chemin L., Daigle O., 2005a, MNRAS, 360, 1201  
 Hernandez O., Wozniak H., Carignan C., Amram P., Chemin L., Daigle O., 2005b, ApJ, 632, 253  
 Hoffman G. L., Lu N. Y., Salpeter E. E., Farhat B., Lamphier C., Roos T., 1993, AJ, 106, 39  
 Hota A., Saikia D. J., 2005, MNRAS, 356, 998  
 Jeong H., Bureau M., Yi S. K., Krajnović D., Davies R. L., 2007, MNRAS, 376, 1021  
 Jing Y. P., Suto Y., 2000, ApJ, 529, L69  
 Kennicutt R. C., Jr, 1989, ApJ, 344, 685  
 Kennicutt R. C., Jr, 1998a, ARA&A, 36, 189  
 Kennicutt R. C., Jr, 1998b, ApJ, 498, 541  
 Kennicutt R. C., Jr, et al., 2003, PASP, 115, 928  
 Klypin A., Kravtsov A. V., Bullock J. S., Primack J. R., 2001, ApJ, 554, 903  
 Knapp G. R., 1987, in de Zeeuw P. T., ed., Proc. IAU Symp. 127, Structure and Dynamics of Elliptical Galaxies. Reidel, Dordrecht, p. 145  
 Lake G., Schommer R. A., van Gorkom J. H., 1987, ApJ, 314, 57  
 Legrand F., Kunth D., Mas-Hesse J. M., Lequeux J., 1997, A&A, 326, 929  
 Lequeux J., Kunth D., Mas-Hesse J. M., Sargent W. L. W., 1995, A&A, 301, 18  
 Leroy A., Bolatto A. D., Simon J. D., Blitz L., 2005, ApJ, 625, 763  
 Lindblad P. O., Jorsater S., 1981, A&A, 97, 56  
 Martimbeau N., Carignan C., Roy J.-R., 1994, AJ, 107, 543  
 Martin P., 1995, AJ, 109, 2428  
 Martin C. L., Kennicutt R. C., 2001, ApJ, 555, 301  
 McGaugh S. S., de Blok W. J. G., 1998, ApJ, 499, 41  
 Mediavilla E., Guijarro A., Castillo-Morales A., Jiménez-Vicente J., Florido E., Arribas S., García-Lorenzo B., Battaner E., 2005, A&A, 433, 79  
 Méndez D. I., Esteban C., 2000, A&A, 359, 493  
 Menéndez-Delmestre K., Sheth K., Schinnerer E., Jarrett T. H., Scoville N. Z., 2007, ApJ, 657, 790  
 Meurer G. R., Staveley-Smith L., Killeen N. E. B., 1998, MNRAS, 300, 705  
 Meurer G. R. et al., 2006, ApJS, 165, 307  
 Miller B. W., 1995, ApJ, 446, L75  
 Miyamoto M., Nagai R., 1975, PASJ, 27, 533  
 Moore B., 1994, Nat, 370, 629  
 Moore B., Quinn T., Governato F., Stadel J., Lake G., 1999, MNRAS, 310, 1147  
 Muñoz-Tuñón C., Caon N., Aguerri J. A. L., 2004, AJ, 127, 58  
 Nakanishi H., Tosaki T., Kohno K., Sofue Y., Kuno N., 2007, PASJ, 59, 61  
 Navarro J. F., Frenk C. S., White S. D. M., 1996, ApJ, 462, 563  
 Navarro J. F., Frenk C. S., White S. D. M., 1997, ApJ, 490, 493  
 Navarro J. F., Hayashi E., Power C., Jenkins A. R., Frenk C. S., White S. D. M., Springel V., Stadel J., Quinn T., 2004, MNRAS, 349, 1039  
 Ondrechen M. P., van der Hulst J. M., Hummel E., 1989, ApJ, 342, 39  
 Palouš J., Ehlerov S., Elmegreen B. G., 2002, Ap&SS, 281, 101  
 Pence W. D., Taylor K., Atherton P., 1990, ApJ, 357, 415  
 Pérez I., Fux R., Freeman K., 2004, A&A, 424, 799  
 Power C., Navarro J. F., Jenkins A., Frenk C. S., White S. D. M., Springel V., Stadel J., Quinn T., 2003, MNRAS, 338, 14

- Puche D., Carignan C., 1988, AJ, 95, 1025  
 Rand R. J., 1994, A&A, 285, 833  
 Regan M. W., Sheth K., Teuben P. J., Vogel S. N., 2002, ApJ, 574, 126  
 Regan M. W. et al., 2006, ApJ, 652, 1112  
 Rownd B. K., Dickey J. M., Helou G., 1994, AJ, 108, 1638  
 Rubin V. C., 1994, AJ, 107, 173  
 Sanders D. B., Scoville N. Z., Soifer B. T., 1991, ApJ, 370, 158  
 Shopbell P. L., Bland-Hawthorn J., 1998, ApJ, 493, 129  
 Sofue Y., Handa T., Golla G., Wielebinski R., 1990, PASJ, 42, 745  
 Springel V., Yoshida N., White S. D. M., 2001, New Astron., 6, 79  
 Summers L. K., Stevens I. R., Strickland D. K., 2001, MNRAS, 327, 385  
 Swaters R. A., 1999, PhD thesis, Rijksuniversiteit, Groningen  
 Swaters R. A., Madore B. F., Trehella M., 2000, ApJ, 531, L107  
 Swaters R. A., Verheijen M. A. W., Bershady M. A., Andersen D. R., 2003a, ApJ, 587, L19  
 Swaters R. A., Madore B. F., van den Bosch F. C., Balcells M., 2003b, ApJ, 583, 732  
 Tempel E., Tenjes P., 2006, MNRAS, 371, 1269  
 Thean A. H. C., Mundell C. G., Pedlar A., Nicholson R. A., 1997, MNRAS, 290, 15  
 van den Bosch F. C., Robertson B. E., Dalcanton J. J., de Blok W. J. G., 2000, AJ, 119, 1579  
 van der Hulst J. M., Huchtmeier W. K., 1979, A&A, 78, 82  
 van Driel W., Buta R. J., 1991, A&A, 245, 7  
 van Driel W., Rots A. H., van Woerden H., 1988, A&A, 204, 39  
 Veilleux S., Rupke D. S., 2002, ApJ, 565, L63  
 Vogelaar M. G. R., Terlouw J. P., 2001, in Harrend Jr. F. R., Primini F. A., Payne H. E., eds, ASP Conf. Ser. Vol. 238, Astronomical Data Analysis Software and Systems. Astron. Soc. Pac., San Francisco, p. 358  
 Walsh D. E. P., van Gorkom J. H., Bies W. E., Katz N., Knapp G. R., Wallington S., 1990, ApJ, 352, 532  
 Walter F., Weiss A., Scoville N., 2002, ApJ, 580, L21  
 Walter F. et al., 2007, ApJ, 661, 102  
 Wong T., Blitz L., 2000, ApJ, 540, 771  
 Zhang X., Wright M., Alexander P., 1993, ApJ, 418, 100

## APPENDIX A: DESCRIPTION OF THE INDIVIDUAL GALAXIES

**NGC 24:** This galaxy is in the background of the Sculptor Group of galaxies (Puche & Carignan 1988). The tilted-ring model fitted to the velocity field gives a mean inclination of  $75 \pm 3^\circ$ , which is consistent with the photometric inclination but not with the H $\alpha$  kinematical inclination of  $64 \pm 3^\circ$  derived in Chemin et al. (2006b). As previously noted by these authors, the low-resolution H $\alpha$  data likely highly underestimate the inclination. A more detailed description and analysis of our H $\alpha$  data for this LSB galaxy will be presented in a forthcoming article (Chemin et al., in preparation).

**NGC 337:** The spiral arms of this barred galaxy are easily visible in the H $\alpha$  integrated map. The velocity field shows a central Z-shape of the velocities indicating that a strong disturbance caused by the bar. See more details in Section 6.

**NGC 855:** Not only bright H $\alpha$  emission can be seen in this dwarf elliptical galaxy, but CO emission has also been detected and star formation is an ongoing process (Nakanishi et al. 2007). The H $\alpha$  gas distribution is extended but the corresponding mass is much smaller than for spirals (Walsh et al. 1990).

**NGC 1097:** This large SBb galaxy exhibits a bright circumnuclear ring with an associated steep velocity gradient. Radial streaming motions from the nuclear ring to the galactic centre and a nuclear spiral are believed to be part of a mechanism by which gas is fuelled to the supermassive black hole (Fathi et al. 2006). Those large streaming motions are most likely responsible for the steep velocity gradient (up to nearly  $300 \text{ km s}^{-1}$ , see Fig. C1) seen towards the centre. The PA of the bar is aligned with both the galaxy's PA and companion, NGC 1097 A. The H $\alpha$  gas is distributed fairly

symmetrically in the prominent spiral arms and in the bar. Non-circular motions are found in and around the bar as shown by the S-shaped distortion of the H $\alpha$  velocities and the spiral arms display large streaming motions indicating the presence of strong density waves (Ondrechen, van der Hulst & Hummel 1989). CO emission is detected mostly in the nuclear ring and the high inferred H $_2$  mass can be explained by the secular action of the bar enhanced by the interaction with NGC 1097 A (Gerin, Combes & Nakai 1988).

**NGC 1291:** This early-type galaxy does not have enough detected ionized gas for detailed kinematical mapping. In fact, only nine H $\alpha$  regions distributed in a ring-like structure can be seen in the H $\alpha$  monochromatic and RV maps. The velocity range corresponding to these H $\alpha$  regions ( $835\text{--}855 \text{ km s}^{-1}$ ) is comparable to what is seen in H $\alpha$  observations, where the gas is distributed in a bright ring surrounding a large central hole devoid of gas (van Driel, Rots & van Woerden 1988), typical of what is seen in the bulge-dominated region of most early-type galaxies. The H $\alpha$  velocity field of this face-on galaxy looks quite regular and the associated rotation curve is essentially flat.

**NGC 1482:** The H $\alpha$  distribution of this early-type galaxy displays a bright central emission region and an eastern blob of H $\alpha$  emission. The measured velocity dispersion of the lines in the central region (some with  $\sigma \geq 100 \text{ km s}^{-1}$ ) is consistent with the gas being ejected from the centre. H $\alpha$  and [N II] images by Veilleux & Rupke (2002) revealed a galactic wind shaped like an hourglass extending above and below the plane of the galaxy. Both H $\alpha$  and H $\alpha$  observations show two bright blobs of emission located on either side of the disc that are rotating about the centre of the galaxy (Hota & Saikia 2005). The CO global profile presents a blueshifted component which is narrower and weaker than the redshifted one (Sanders, Scoville & Soifer 1991).

**NGC 1512:** This strongly barred galaxy hosts two rings inside the bar, a nuclear ring with strong H $\alpha$  emission and large velocity gradient and an inner ring located at the end of the bar with weak emission compared to the nuclear ring. The PA of the nuclear ring is not perfectly aligned with those of the outer ring and bar and the nuclear ring is off-centred with respect to the inner ring. This H $\alpha$  morphology is consistent with that presented by Buta (1988). Their rotation model shows that the nuclear ring must be expanding at a significant velocity (see also Lindblad & Jorsater 1981). This galaxy is likely to be gravitationally interacting with its neighbour NGC 1510, as shown by the perturbed H $\alpha$  velocity field (Hawarden et al. 1979). It is worth also mentioning the presence of very extended tidal arms in H $\alpha$  and in UV, outside our FOV (Meurer et al. 2006).

**NGC 1566:** The spiral arms of this grand-design galaxy are well traced in the  $3.6 \mu\text{m}$  and monochromatic images. Inside the 20 arcsec radius lies intense Doppler broadening typical of a Seyfert 1 galaxy but too strong to be sampled by the free spectral range of the FP interferometer used for our observations. Also, there is an expanding bubble of gas located near  $\alpha = 04^h 19^m 58^s$ ,  $\delta = -54^\circ 55' 13''$  associated with four strong H $\alpha$  regions in the north-west arm and exhibiting a strong velocity gradient. These results are consistent with the H $\alpha$  observations made by Pence, Taylor & Atherton (1990). See Agüero, Díaz & Bajaja (2004) for a dynamical analysis based on long-slit spectroscopy.

**NGC 1705:** This peculiar galaxy shows a rotating disc that is dominated by an intense ongoing starburst. Therefore, no kinematical parameters could be extracted. The double profiles and multiple arcs of material visible in H $\alpha$  suggest indeed violent ejections of gas. In contrast, H $\alpha$  synthesis observations revealed a rotating disc in a dominant dark matter halo (Meurer, Staveley-Smith & Killeen 1998).

Holmberg II: The H $\alpha$  content of this irregular galaxy shows weak rotation and a lack of spatial coverage, therefore no kinematical parameters or rotation curve could be extracted. Besides, the neutral gas appears compressed on the south-east with a large but faint component extending on the opposite side, indicating ram pressure stripping from the intergalactic medium (Bureau & Carignan 2002). The H $\text{I}$  velocity field displays a weak but clear rotating disc pattern. Like most of the dwarfs (see e.g. Carignan & Purton 1998), there is more luminous mass in H $\text{I}$  than in stars, but contrary to most dwarfs where dark matter dominates at nearly all radii, in Ho II, dark matter dominates only in the outer parts of the galaxy like in massive spirals.

DDO 053: This dwarf irregular galaxy has some diffuse H $\alpha$  but since our observations have little spatial coverage, no kinematical parameters are given for this galaxy. The H $\text{I}$  distribution is compact and shows two peaks of emission with one peak being associated with the brighter region visible in H $\alpha$  (Walter et al. 2007).

NGC 2841: The velocity field of this fast-rotating galaxy does not show any sign of perturbation. The RVs inside a 50 arcsec radius are not mapped in this H $\alpha$  study because of Doppler broadening of the line typical of Seyfert 1 galaxies. Inside the 50 arcsec radius, H $\alpha$  and [N II] images by Afanasiev & Sil'chenko (1999) seem to suggest that the excitation of the ionized gas is caused by shock wavefronts. Little CO is seen in this galaxy (Helfer et al. 2003).

Holmberg I: This dwarf galaxy has very little H $\alpha$  emission and the associated velocity field shows weak rotation. The H $\text{I}$  morphology is characterized by one giant hole enclosed by a ring-like structure. The south side of the H $\text{I}$  ring is located so that it encloses the H $\alpha$  emission (Walter et al. 2007).

NGC 3034 (M82): This starburst galaxy is seen nearly edge-on and the opacity of the gas renders impossible the extraction of the kinematical parameters. The almost hourglass shape of the H $\alpha$  distribution and the presence of double profiles above and below the disc indicates a remarkable outflow of gas perpendicular to the plane of the galaxy. Line splitting is also found in CO observations of the outflow and an estimated 10 per cent of the gas may be lost to the intergalactic medium (Walter, Weiss & Scoville 2002). The FP data presented here agree reasonably well with those of Shopbell & Bland-Hawthorn (1998), particularly the strong redshifting and blueshifting seen north and south of the disc, respectively. The differences in velocity between the two FP data sets are mainly due to the high interference order of our FP etalon which is designed for smaller radial velocity range and higher spectral resolution. Fast ejection of material is seen in the H $\alpha$  velocity field, splitting the H $\alpha$  line by  $\sim 300 \text{ km s}^{-1}$ .

Holmberg IX: There is no H $\alpha$  emission originating from this galaxy. However, an expanding bubble of gas can be seen  $\sim 2$  arcmin north-east of Holmberg IX. This large supershell ( $\sim 250$  pc) is thought to be one of the most X-ray luminous supernova remnants (Miller 1995). The position, velocity and abundance similarities between Holmberg IX and the superbubble suggest that they are related.

NGC 3190: This early-type galaxy has very little H $\alpha$ . A close companion lies just 5 arcsec north-west and both galaxies are in interaction. No kinematical parameters are given for this peculiar galaxy.

IC 2574: The H $\alpha$  integrated map of this dwarf spiral galaxy presents several supershells as well as large arc-like shaped H $\text{II}$  complexes indicating gas compressed by powerful star-forming events. The kinematics yields a slowly rising rotation curve until a value of  $V_{\text{rot}} \sim 70 \text{ km s}^{-1}$  is reached (Blais-Ouellette, Amram & Carignan 2001). Mass modelling using the H $\text{I}$  rotation curve from

Martimbeau, Carignan & Roy (1994) yields a dark matter contribution of 90 per cent which dominates at all radii. The H $\text{I}$  morphology is characterized by holes and several of the H $\alpha$  regions are located around the rims of the H $\text{I}$  holes. Finally, Leroy et al. (2005) have detected molecular gas in this star-forming galaxy.

NGC 3265: This dwarf elliptical galaxy has a small rotating H $\alpha$  disc of radius  $\sim 8$  arcsec in agreement with 21-cm line observations. The H $\text{I}$  rotation curve rises steeply until  $r = 20$  arcsec then goes flat and the RV map shows presence of non-circular motions or warping (Lake, Schommer & van Gorkom 1987). Since for the few elliptical galaxies detected in H $\text{I}$ , the gas content is not correlated with luminosity and the spatial distribution is not reminiscent of that found in spiral galaxies, the origin of the gas is thought to be external (Knapp 1987). Molecular gas is detected in this elliptical galaxy and star formation is an ongoing process in the centre (Gordon 1991). Both CO and H $\text{I}$  profiles have half-intensity widths of  $\sim 180 \text{ km s}^{-1}$ .

Mrk 33: The H $\alpha$  emission of this dwarf starburst galaxy, also known as Haro 2, reveals at least two star-forming regions in the galactic centre and the overall kinematics resemble a luminous oblong expanding shell. A more in-depth observation by Méndez & Esteban (2000) has shown three bright H $\alpha$  knots and faint filamentary structures. The presence of an extended X-ray emitting region lying within the supershell suggests a superbubble caused by a starburst-driven outflow (Lequeux et al. 1995; Legrand et al. 1997; Summers, Stevens & Strickland 2001). No kinematical parameters are given for this galaxy.

NGC 3351 (M95): The H $\alpha$  distribution in this barred galaxy shows a luminous centre with an H $\alpha$  ring and the corresponding velocity field presents evidence of strong non-circular motions in the centre. Kinematics inside this region reveal that the stellar bar is radially driving gas towards the star-forming H $\alpha$  ring at  $V = 25 \text{ km s}^{-1}$  (Hägele et al. 2007), from elongated  $x_1$  orbits to the  $x_2$  orbits closer to the bar. Furthermore, the detected excess in the central ISM content of the large-scale bar implies that the latter is transporting gas to smaller radii (Regan et al. 2006). Interestingly, CO observations have shown a small molecular bar aligned perpendicular to the large-scale stellar bar (Devereux, Kenney & Young 1992; Helfer et al. 2003). The earlier paper argues that a resonance caused by the stellar bar lies in the vicinity of the H $\alpha$  ring and nuclear molecular gas bar. The velocity gradient in the central regions is steep in both CO and H $\alpha$  data. There is also an inner ring at the end of the bar where the velocities are regular and not perturbed. Another H $\alpha$  kinematical analysis has been done for this galaxy by Buta (1988). Finally, two nuclear spiral arms residing inside the circumnuclear ring can be seen in *Spitzer* IRAC 3.6- $\mu\text{m}$  data.

NGC 3627 (M66): This member of the Leo triplet shows a highly perturbed H $\alpha$  morphology and velocity field. Streaming motions can be seen along the spiral arms and a warp can be fitted on the southern, receding side of the disc. The H $\alpha$  kinematics is consistent with CO and H $\text{I}$  data obtained by Helfer et al. (2003) and Regan et al. (2002), respectively. A molecular and H $\alpha$  ring has been found lying at the position of the ultraharmonic resonance induced by the bar pattern speed (Chemin et al. 2003). The proposed explanation for the asymmetric and perturbed gas morphology is a tidal interaction with NGC 3628 (Afanasiev & Sil'chenko 2005; see also Zhang, Wright & Alexander 1993).

NGC 3773: Visible in both H $\alpha$  and H $\text{I}$  data, this early-type galaxy displays gas concentration in its centre. There is no detectable rotation and the global profile is very narrow, both for the ionized and neutral gas (Burstein, Krumm & Salpeter 1987).

NGC 4254 (M99): The kinematical analysis of this grand design spiral galaxy has already been presented in the Virgo galaxy

cluster sample of Chemin et al. (2006a). The  $\text{H}\alpha$  velocity field presents significant streaming motions along the spiral structure. Recent observations by Haynes, Giovanelli & Kent (2007) reported an  $\text{H}\iota$  tail extending  $\sim 250$  kpc to the north of NGC 4254, perhaps the result of galaxy harassment as the galaxy enters the Virgo cluster.

NGC 4450: The FP data of this anemic galaxy have been presented in Chemin et al. (2006a). The  $\text{H}\alpha$  distribution is very clumpy and the velocity field perturbed in the innermost regions of the galaxy. A new tilted-ring model is fitted to the velocity field using rings of 4 arcsec width instead of 2 arcsec in our previous analysis. This allows one to derive a new major axis PA of  $353 \pm 5^\circ$  with a smaller error bar than in Chemin et al. (2006b). The values remain in agreement within the errors.

NGC 4559: The  $\text{H}\alpha$  velocity field of this late-type galaxy shows the presence of streaming motions in its centre and is somewhat patchy far from the centre. The  $\text{H}\iota$  disc, extending further out than the optical disc, is warped and lopsided in both distribution and kinematics (Barbieri et al. 2005). Their  $\text{H}\iota$  PV diagram revealed the presence of a thick  $\text{H}\iota$  layer rotating  $25\text{--}50 \text{ km s}^{-1}$  more slowly than the value for the thin disc.

NGC 4594 (M104): This early-type galaxy is better known as the Sombrero galaxy. The  $\text{H}\alpha$  observations display only one diffuse ionized region west of the nearly edge-on disc and the corresponding RVs are in agreement with the galaxy's systemic velocity. Stellar kinematics reveal for the rotation curve a rapid rise followed by a decrease which can be explained by the prominent galactic bulge (Carter & Jenkins 1993). Mass modelling using globular cluster kinematics has shown that the  $M/L$  value increases with radius, hence that M104 has a dark matter halo (Bridges et al. 1997). Another study of the dark matter distribution has been done by Tempel & Tenjes (2006).

NGC 4631: This galaxy is seen edge-on and its inclination renders impossible the extraction of the kinematical parameters. The interaction with the nearby dwarf galaxy is thought to be responsible for the warp seen on the south-east side of the  $\text{H}\alpha$  velocity field. Our  $\text{H}\alpha$  results are consistent with those of Golla, Dettmar & Domgoergen (1996). As for the  $\text{H}\iota$  data, the results obtained by Rand (1994) show that the maximum rotation velocity is  $140 \text{ km s}^{-1}$  and that the  $\text{H}\iota$  disc can be modelled as having two distinct velocity components. CO observations have demonstrated that the sources of these distinct velocities are the spiral arms within the gas disc (Sofue et al. 1990).

NGC 4736 (M94): This ringed galaxy exhibits a bright inner ring with a nearly constant rotational velocity of about  $195 \text{ km s}^{-1}$ . The dispersion velocities are typical of those seen in  $\text{H}\ii$  regions. The location of this  $\text{H}\alpha$  ring is consistent with resonances caused by the bar and by a larger oval distortion. CO observations reveal tightly wound spiral arms separated by a small nuclear bar that is perpendicular to the major axis PA of the galaxy (Helfer et al. 2003) as well as gas moving on elliptical orbits around the nuclear bar. Modelling of  $\text{H}\alpha$  and CO kinematics shows an inflow of material near the ends of the nuclear bar, an outflow between the bar and the ring, and an inflow of gas just outside the ring (Wong & Blitz 2000; Muñoz-Tuñón, Caon & Aguerri 2004). The slightly declining  $\text{H}\alpha$  rotation curve presented in this paper is consistent with CO and  $\text{H}\iota$  observations, but not in the central regions.

DDO 154: This dwarf irregular galaxy has only a few discrete  $\text{H}\ii$  regions and larger diffuse regions. The  $\text{H}\alpha$  velocity field shows large-scale but slow rotation ( $\sim 30 \text{ km s}^{-1}$ ) that can be measured to just below 2 arcmin. The 21-cm  $\text{H}\iota$  observations present a regular but extended gas disc having a slight warp at the south-west end (Carignan & Beaulieu 1989; Hoffman et al. 1993). Mass modelling

of this galaxy reveals that more than 90 per cent of the mass is found in the dark component (Carignan & Freeman 1988; Carignan & Purton 1998).

NGC 4826 (M64): The  $\text{H}\alpha$  distribution of this galaxy, confined to the inner disc, is more extended on the north-west receding side than on the approaching side, which is consistent with CO emission (Helfer et al. 2003). The  $\text{H}\iota$  gas, on the other end, extends far beyond the optical radius  $R_{25}$  and is also distributed asymmetrically. The  $\text{H}\iota$  velocity field reveals a counter-rotating gaseous disc outside the 2 arcmin diameter (Braun, Walterbos & Kennicutt 1992). A detailed kinematical study, based on  $\text{H}\alpha$  long-slit spectroscopy, reveals a transition region near the prominent dust lane ( $50'' \leq r \leq 70''$ ) where the gas motion is undergoing a change in its orbital direction, from prograde in the inner disc to retrograde in the outer disc (Rubin 1994). This situation, symptomatic of a merger, has been widely seen in elliptical galaxies, but rarely in disc galaxies.

DDO 165: The  $\text{H}\alpha$  map of this dwarf galaxy presents only four  $\text{H}\ii$  regions that may not be all physically related to the galaxy. The  $\text{H}\iota$  distribution is extended and is somewhat arc-like shaped (Walter et al. 2007).

NGC 5033: The  $\text{H}\alpha$  velocity field displays a strong velocity gradient ( $\sim 100 \text{ km s}^{-1} \text{ kpc}^{-1}$ ) in the centre of this galaxy, agreeing with CO emission (Helfer et al. 2003). The broad profiles found near the centre of the galaxy are characteristic of a Seyfert galaxy.  $[\text{O III}]$  and  $\text{H}\beta$  observations show, respectively, an asymmetric morphology and an off-centred active nucleus which can be understood in terms of a past merger (Mediavilla et al. 2005). The  $\text{H}\iota$  large-scale velocity field is well ordered and streaming motions can be seen near the spiral structures (see Bosma 1981; Thean et al. 1997). The  $\text{H}\alpha$  and  $\text{H}\iota$  rotation curves present a constant rotational velocity of  $\sim 215 \text{ km s}^{-1}$  and a warp developing beyond the optical disc.

NGC 5408: This irregular galaxy has a highly asymmetric  $\text{H}\alpha$  morphology with a bright nuclear region situated at one end of an elongated optical distribution. The FP observations are in agreement with those of Bohuski et al. (1972). The absence of large-scale motions is the reason why no kinematical parameters are given for this galaxy.

NGC 5474: The  $\text{H}\alpha$  distribution of this peculiar galaxy is composed of several  $\text{H}\ii$  regions and clumpy diffuse ionized gas which are rotating weakly. The  $\text{H}\iota$  disc also displays a clumpy but fairly symmetric distribution. The  $\text{H}\iota$  velocity field exhibits normal differential rotation but warping near the edge of the  $\text{H}\iota$  disc can be seen (Rownd, Dickey & Helou 1994, see also van der Hulst & Huchtmeier 1979).

NGC 6822: This nearby irregular galaxy does not exhibit strong rotation within the FOV of our observations, while some is seen in the  $\text{H}\iota$  data (de Blok & Walter 2000). The  $\text{H}\alpha$  emission is composed of  $\text{H}\ii$  regions and low-density regions of diffuse ionized gas. The  $\text{H}\iota$  distribution is far more extended and is dominated by holes and clouds.

NGC 7552: This SBab galaxy is completely dominated by its bar, making the extraction of kinematical parameters impossible. The velocity field shows a central S-shaped disturbance indicating non-circular motions caused by the bar. A steep velocity gradient ( $\sim 150 \text{ km s}^{-1} \text{ kpc}^{-1}$ ) is present in the nuclear region as well as a bright  $\text{H}\alpha$  centre representative of a LINER galaxy.

NGC 7793: The close-up view of this galaxy displays several  $\text{H}\ii$  regions and the corresponding  $\text{H}\alpha$  velocity field exhibits an S-shaped distortion of the velocities along the minor axis. A kinematical analysis of the fairly regular  $\text{H}\iota$  velocity field reveals a declining rotation curve (Carignan & Puche 1990). Deep FP observations of the diffuse gas have shown an extended  $\text{H}\alpha$  disc that is detected all the way to the edge of the  $\text{H}\iota$  disc.

## APPENDIX B: FIGURES

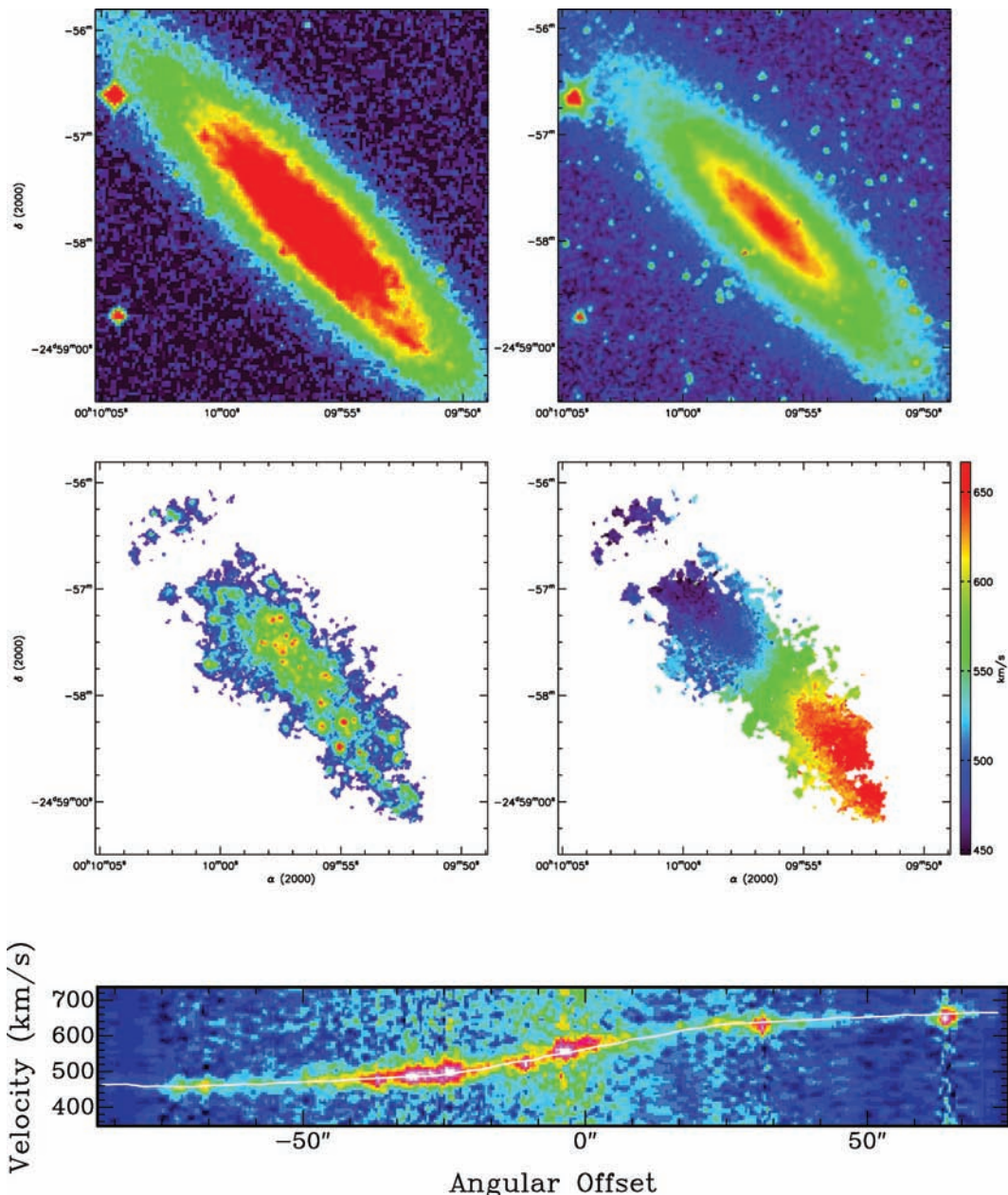


**Figure B1.** NGC 24. Top left-hand panel: DSS blue-band image. Top right-hand panel: *Spitzer* IRAC 3.6- $\mu$ m image. Middle left-hand panel:  $H\alpha$  integrated map. Middle right-hand panel:  $H\alpha$  velocity field. Bottom: PV diagram.

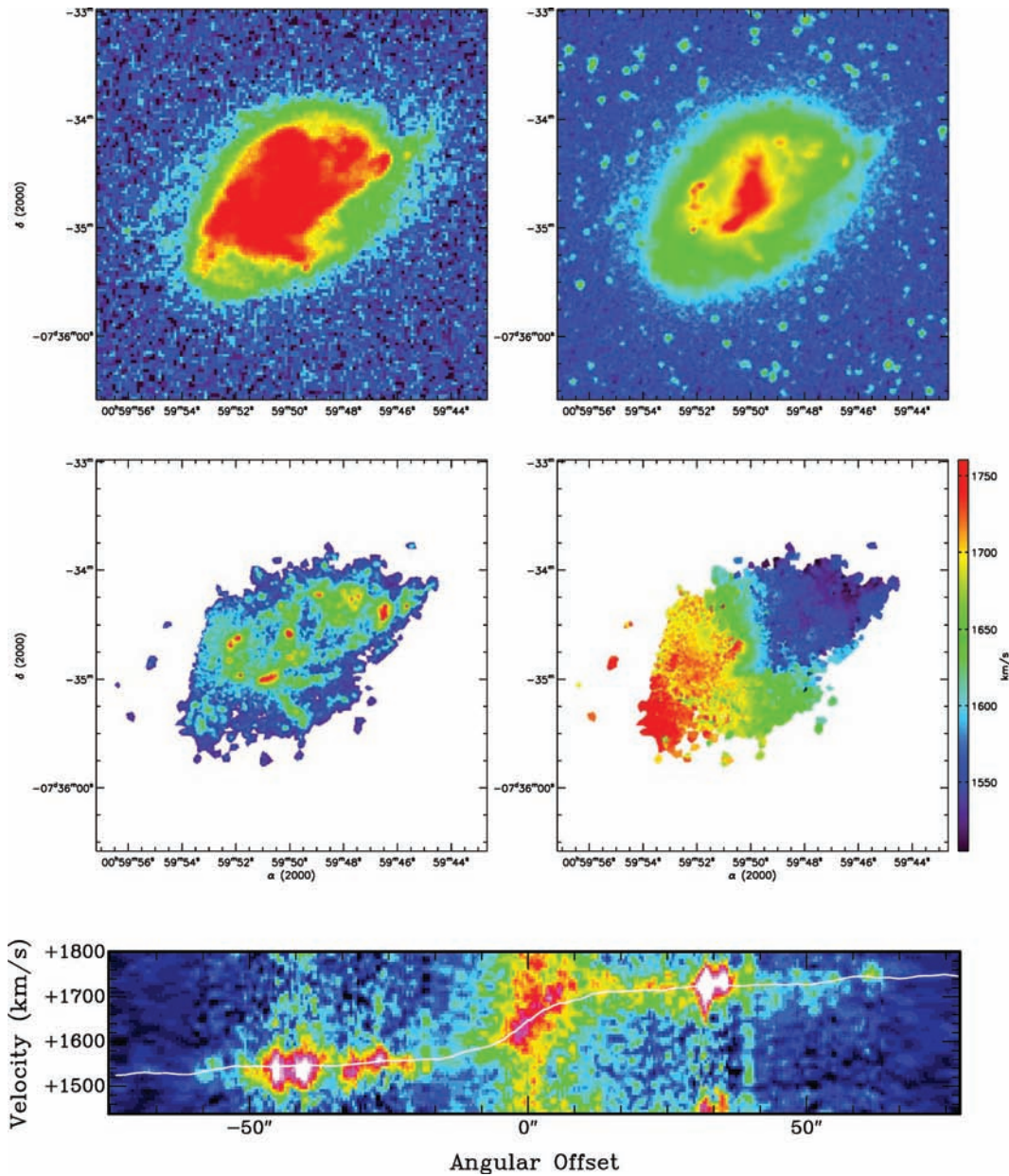


**Figure B2.** NGC 337. Top left-hand panel: DSS blue-band image. Top right-hand panel: *Spitzer* IRAC 3.6- $\mu$ m image. Middle left-hand panel: H $\alpha$  integrated map. Middle right-hand panel: H $\alpha$  velocity field. Bottom: PV diagram.

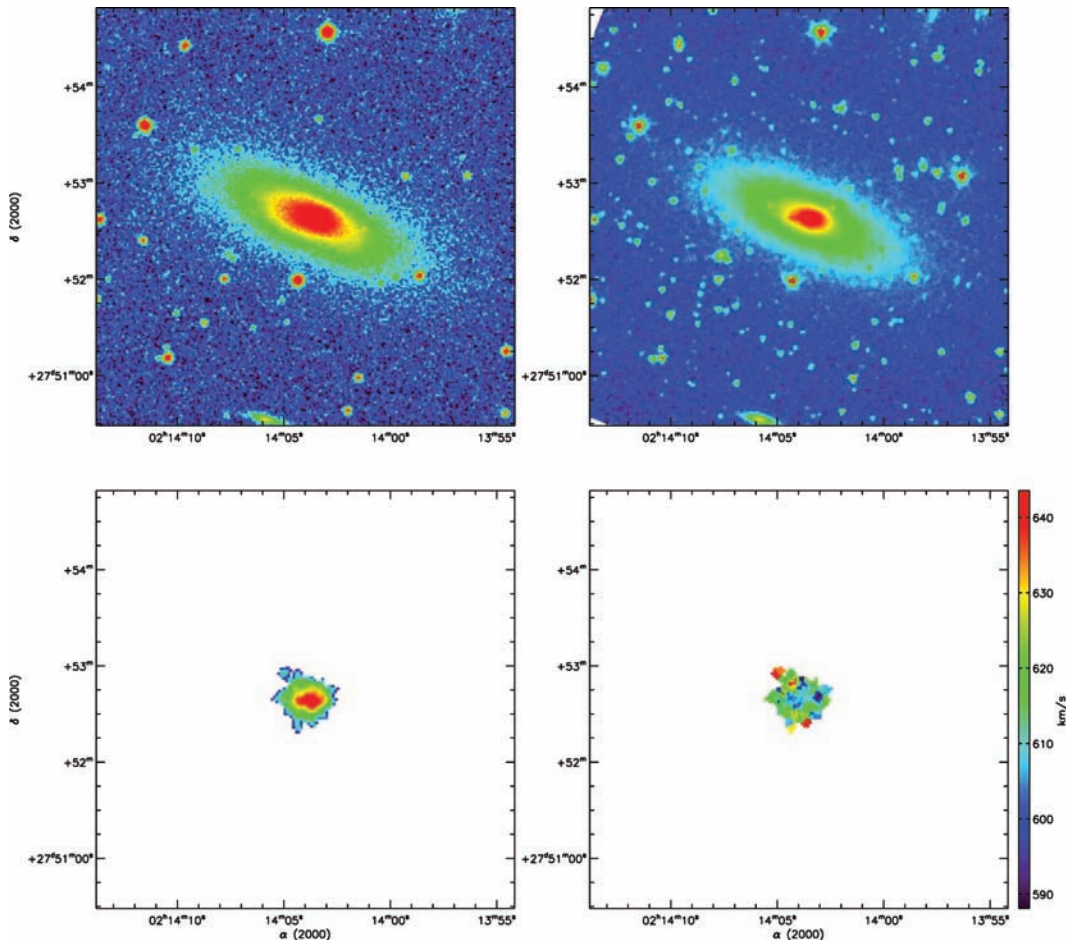


**Figure B3.** NGC 855. Top left-hand panel: DSS blue-band image. Top right-hand panel: *Spitzer* IRAC 3.6- $\mu$ m image. Bottom left-hand panel: H $\alpha$  integrated map. Bottom right-hand panel: H $\alpha$  velocity field.

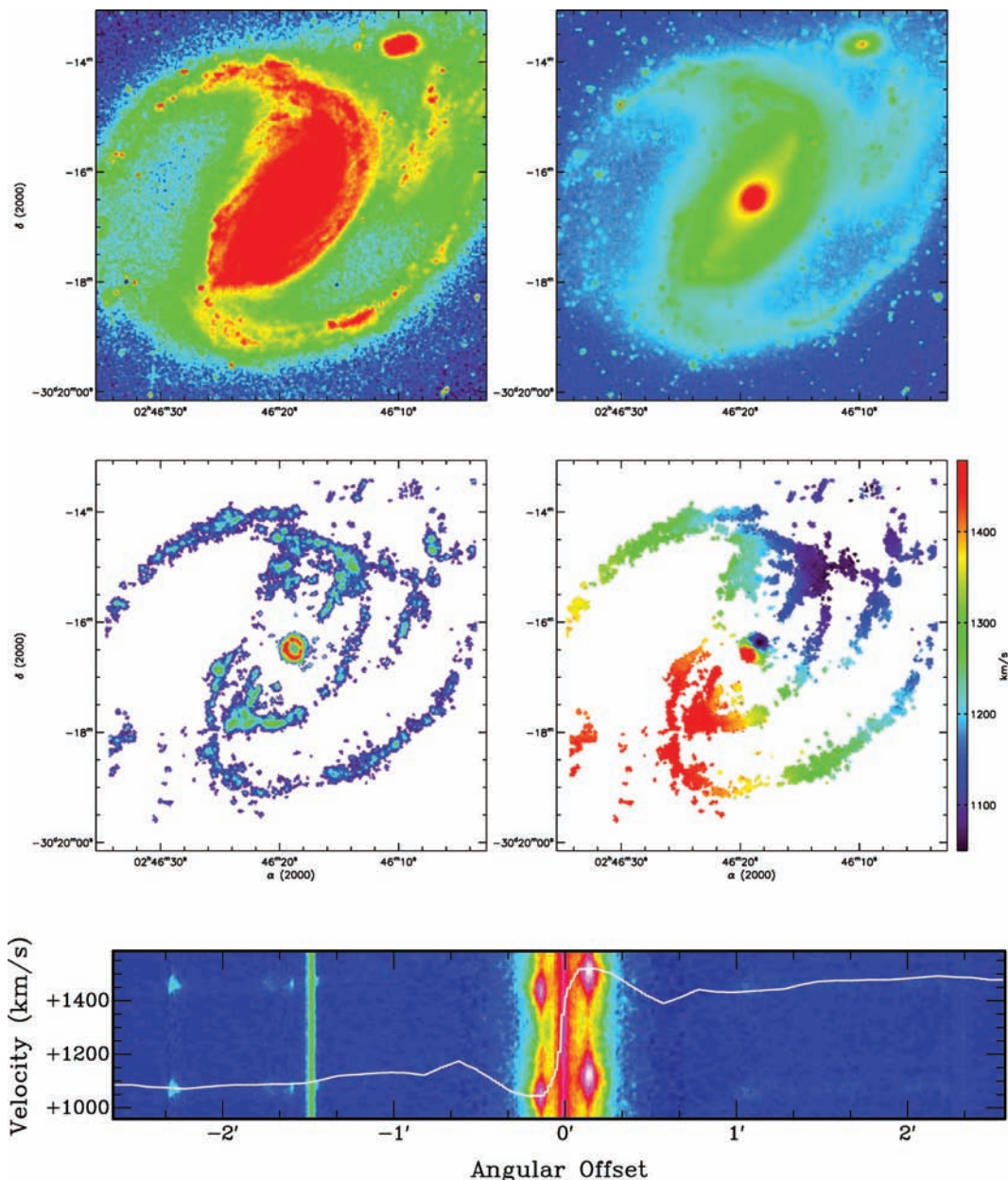


**Figure B4.** NGC 1097. Top left-hand panel: DSS blue-band image. Top right-hand panel: *Spitzer* IRAC 3.6-μm image. Middle left-hand panel:  $\text{H}\alpha$  integrated map. Middle right-hand panel:  $\text{H}\alpha$  velocity field. Bottom: PV diagram.

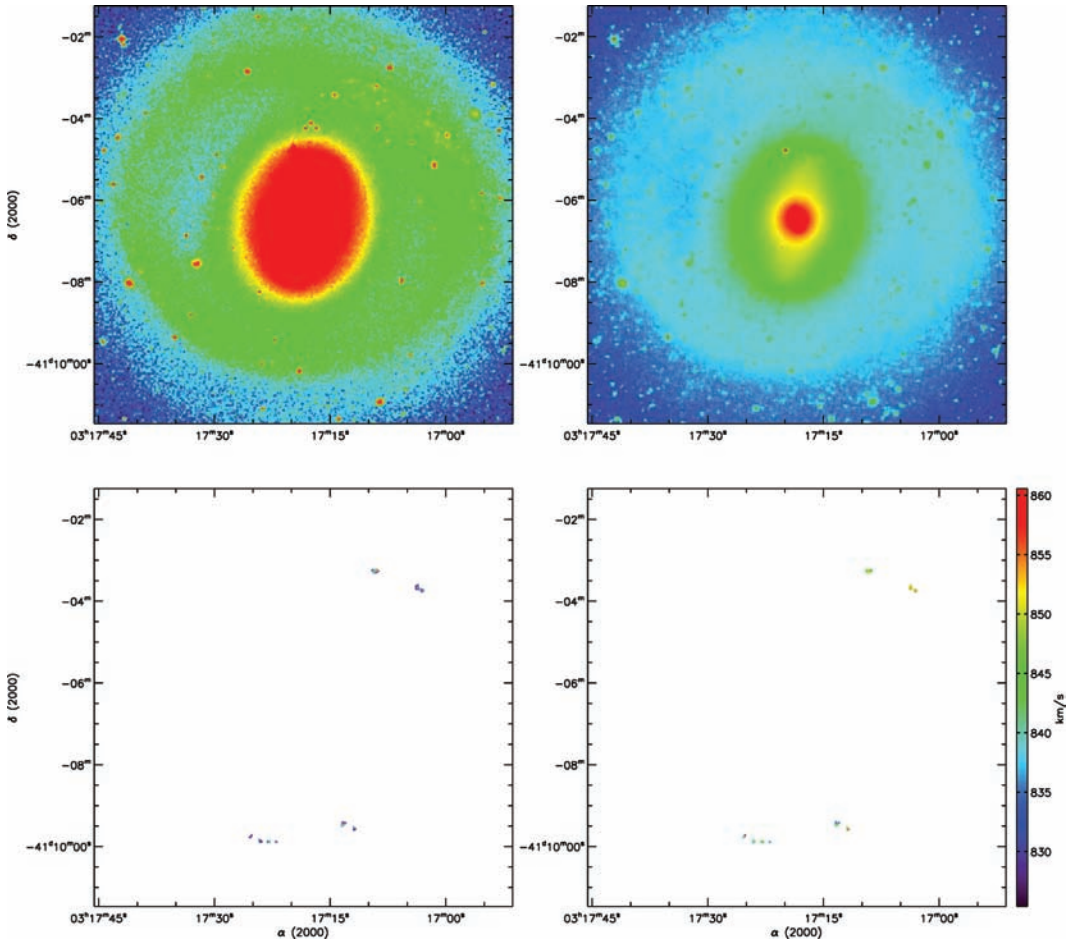


**Figure B5.** NGC 1291. Top left-hand panel: DSS blue-band image. Top right-hand panel: *Spitzer* IRAC 3.6- $\mu$ m image. Bottom left-hand panel: H $\alpha$  integrated map. Bottom right-hand panel: H $\alpha$  velocity field.

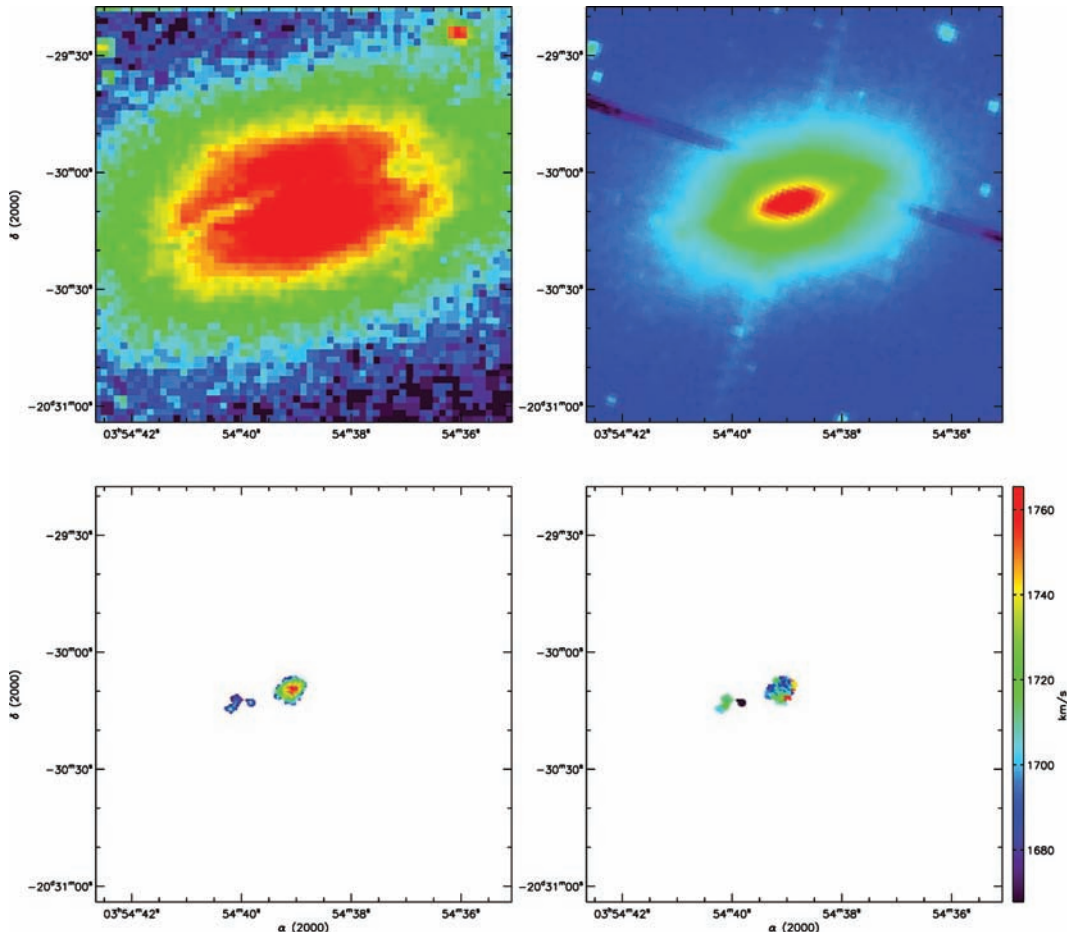


**Figure B6.** NGC 1482. Top left-hand panel: DSS blue-band image. Top right-hand panel: *Spitzer* IRAC 3.6- $\mu$ m image. Bottom left-hand panel: H $\alpha$  integrated map. Bottom right-hand panel: H $\alpha$  velocity field.

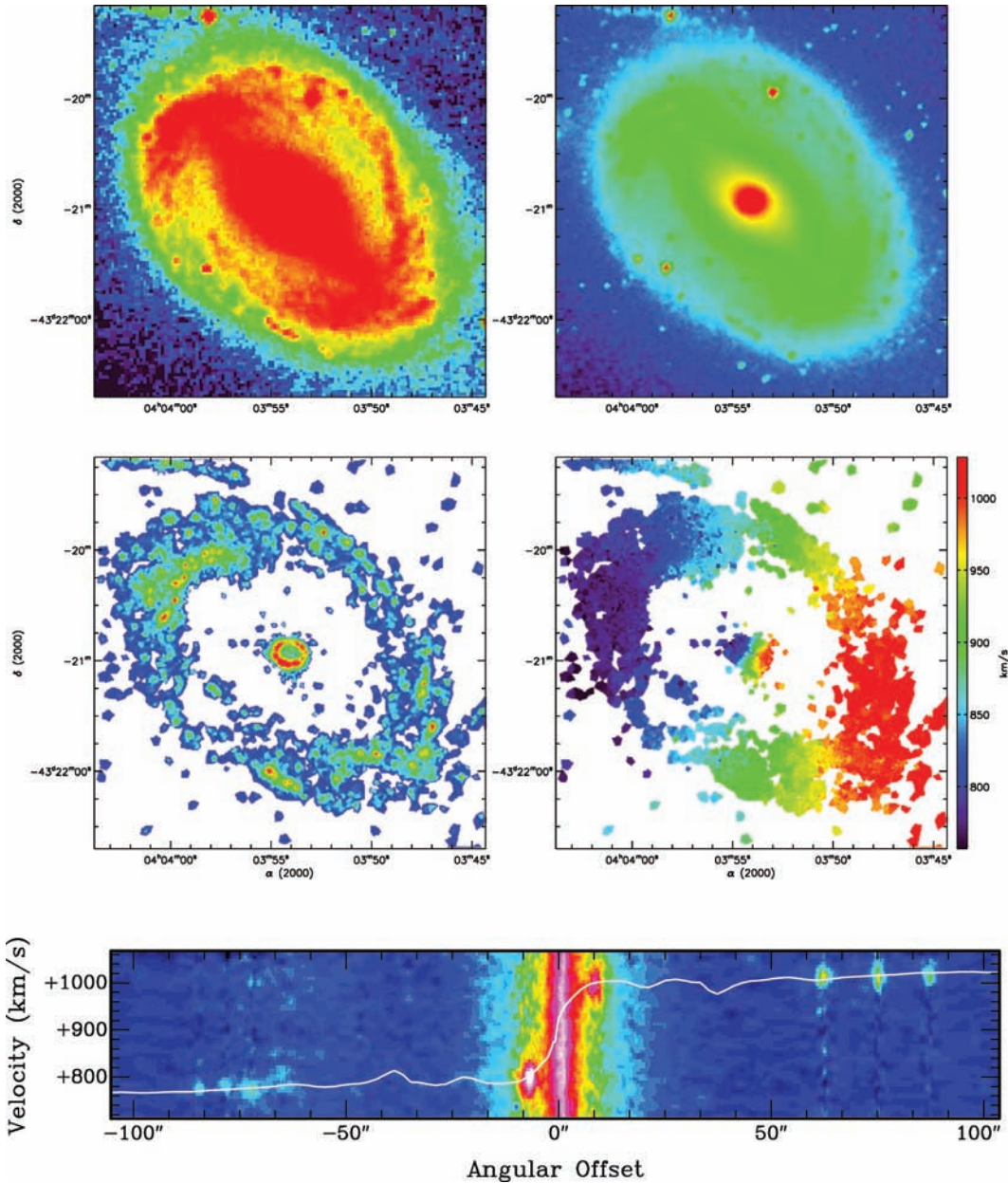


**Figure B7.** NGC 1512. Top left-hand panel: DSS blue-band image. Top right-hand panel: *Spitzer* IRAC 3.6-μm image. Middle left-hand panel: H $\alpha$  integrated map. Middle right-hand panel: H $\alpha$  velocity field. Bottom: PV diagram.

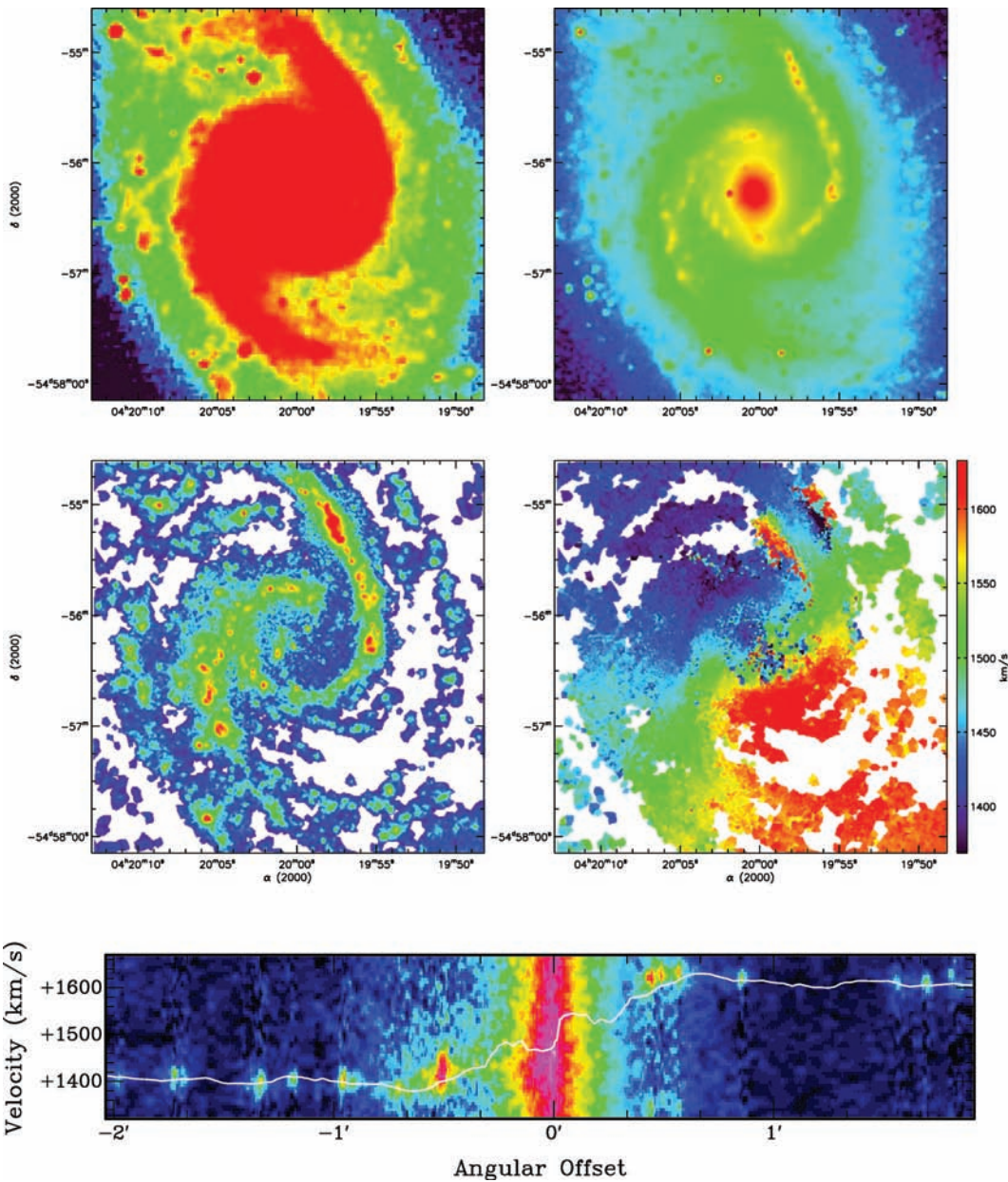


**Figure B8.** NGC 1566. Top left-hand panel: DSS blue-band image. Top right-hand panel: *Spitzer* IRAC 3.6-μm image. Middle left-hand panel:  $\text{H}\alpha$  integrated map. Middle right-hand panel:  $\text{H}\alpha$  velocity field. Bottom: PV diagram.

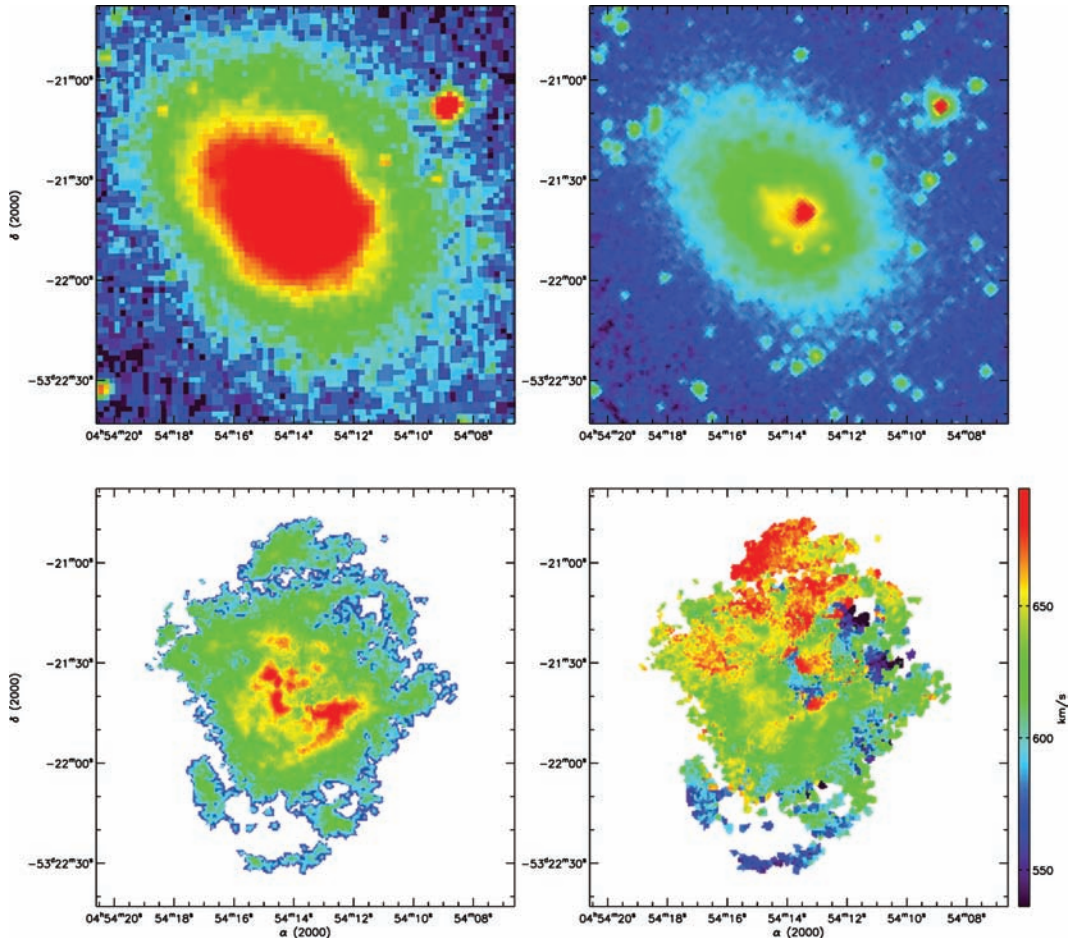


**Figure B9.** NGC 1705. Top left-hand panel: DSS blue-band image. Top right-hand panel: *Spitzer* IRAC 3.6- $\mu$ m image. Bottom left-hand panel: H $\alpha$  integrated map. Bottom right-hand panel: H $\alpha$  velocity field.

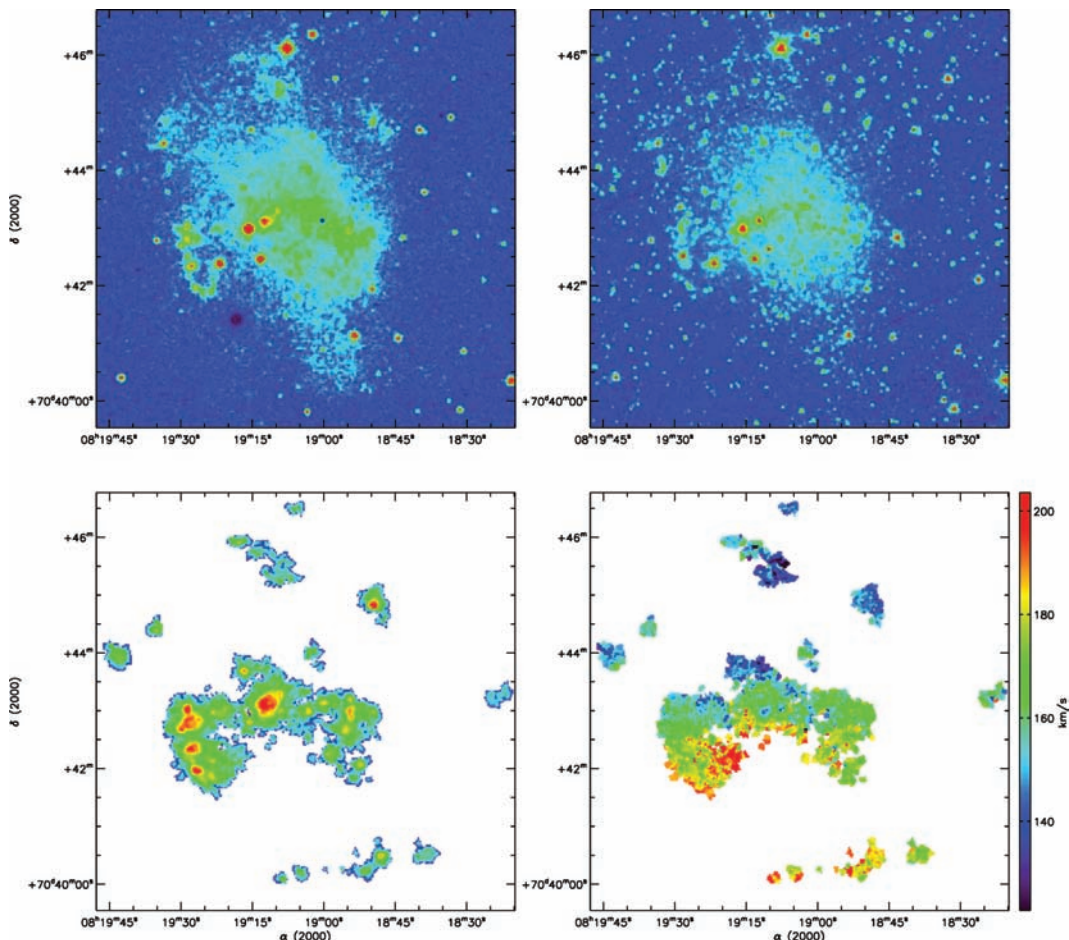


**Figure B10.** Holmberg II. Top left-hand panel: DSS blue-band image. Top right-hand panel: *Spitzer* IRAC 3.6- $\mu$ m image. Bottom left-hand panel: H $\alpha$  integrated map. Bottom right-hand panel: H $\alpha$  velocity field.

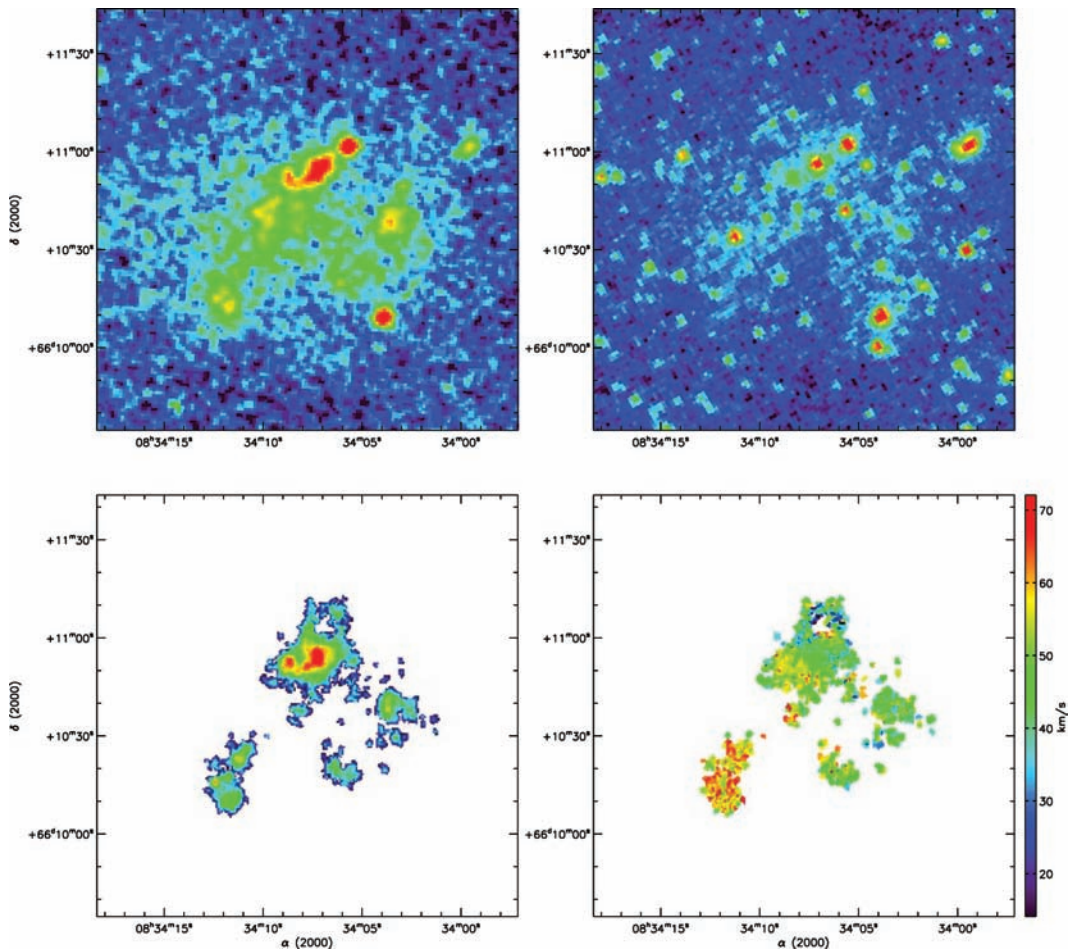


**Figure B11.** DDO 053. Top left-hand panel: DSS blue-band image. Top right-hand panel: *Spitzer* IRAC 3.6- $\mu$ m image. Bottom left-hand panel: H $\alpha$  integrated map. Bottom right-hand panel: H $\alpha$  velocity field.

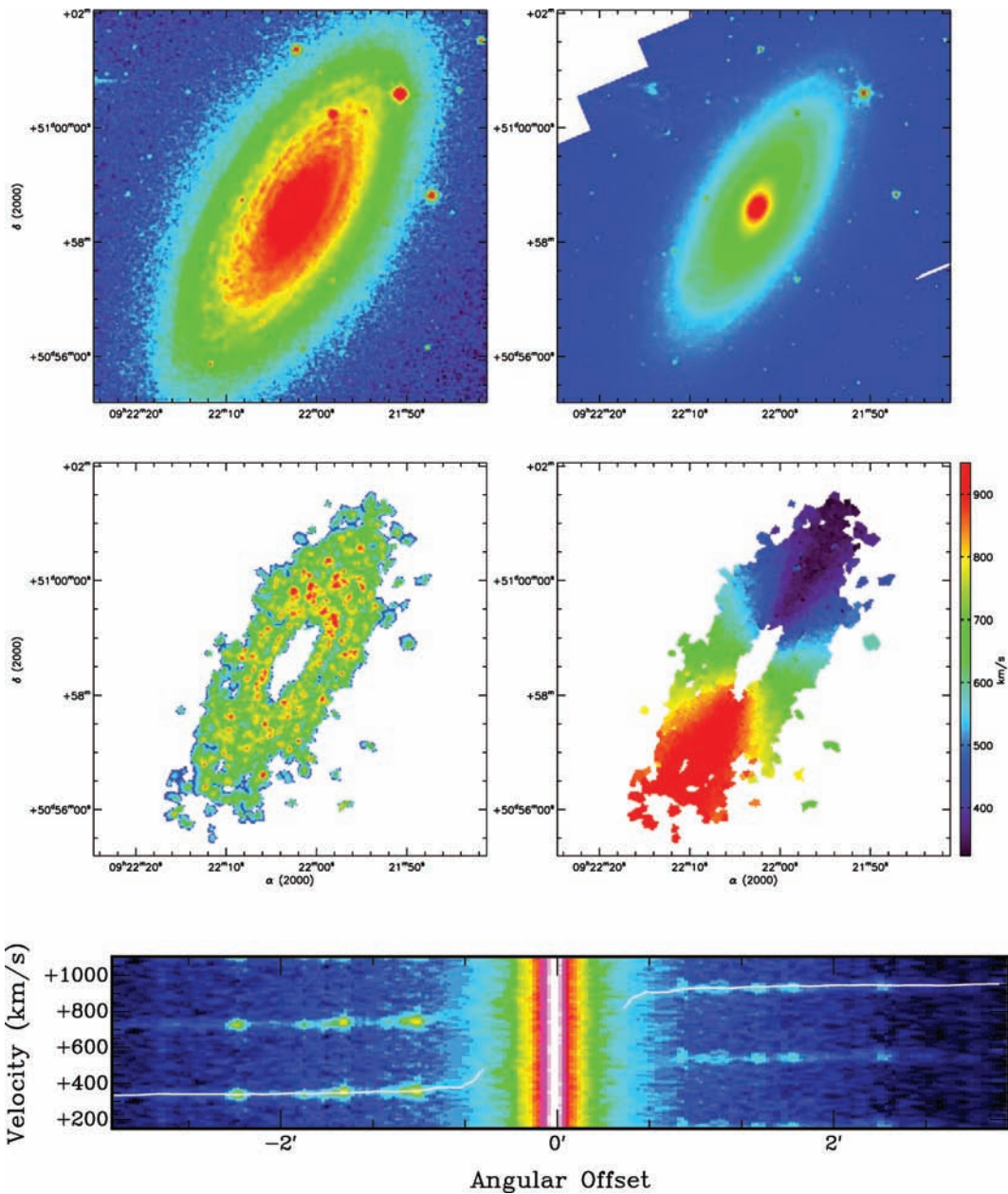


**Figure B12.** NGC 2841. Top left-hand panel: DSS blue-band image. Top right-hand panel: *Spitzer* IRAC 3.6-μm image. Middle left-hand panel:  $\text{H}\alpha$  integrated map. Middle right-hand panel:  $\text{H}\alpha$  velocity field. Bottom: PV diagram.

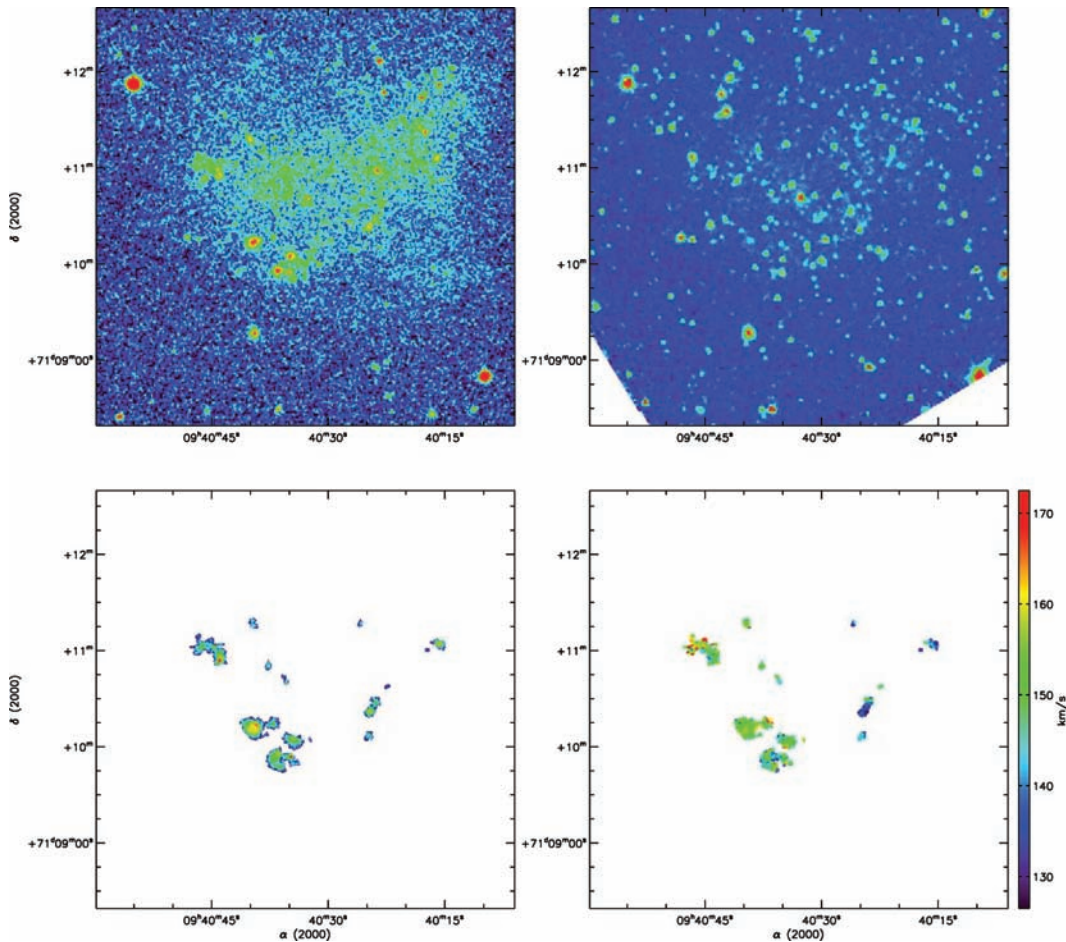


**Figure B13.** Holmberg I. Top left-hand panel: DSS blue-band image. Top right-hand panel: *Spitzer* IRAC 3.6- $\mu\text{m}$  image. Bottom left-hand panel:  $\text{H}\alpha$  integrated map. Bottom right-hand panel:  $\text{H}\alpha$  velocity field.

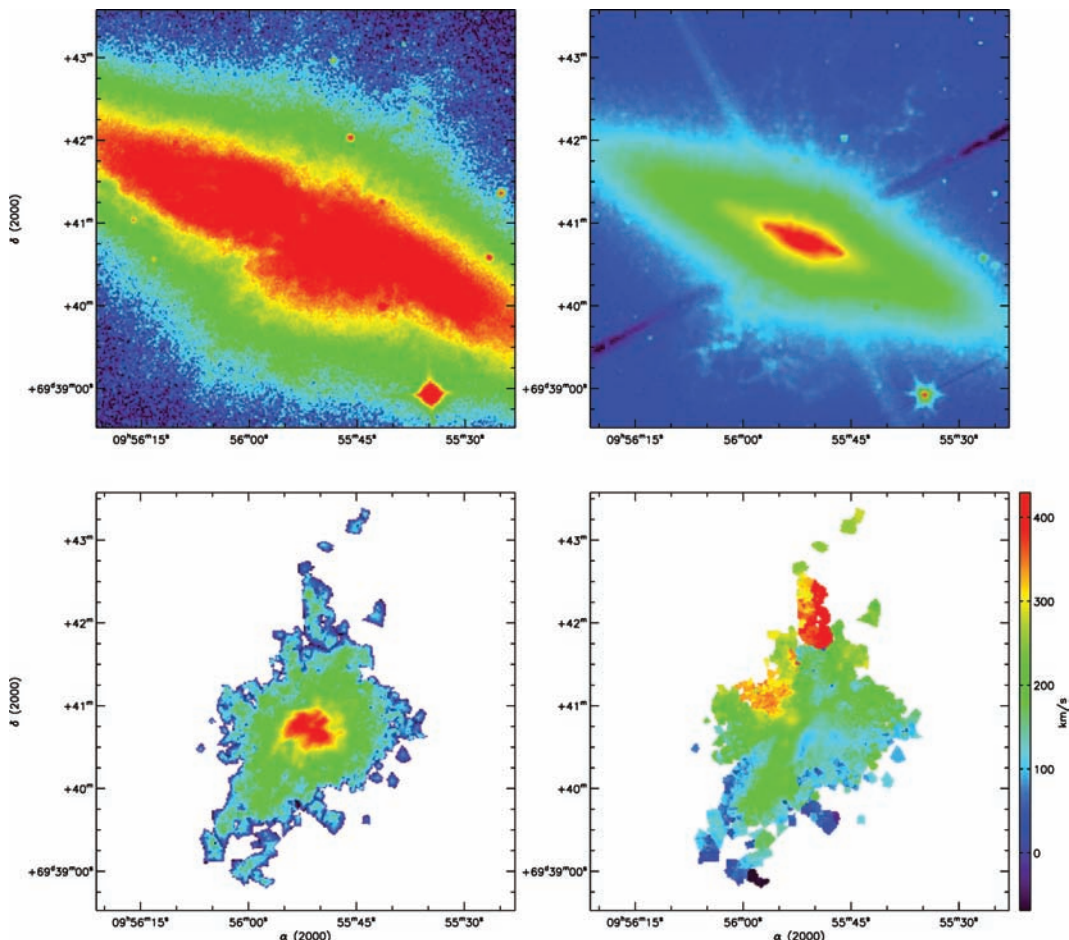


**Figure B14.** NGC 3034. Top left-hand panel: DSS blue-band image. Top right-hand panel: *Spitzer* IRAC 3.6- $\mu$ m image. Bottom left-hand panel: H $\alpha$  integrated map. Bottom right-hand panel: H $\alpha$  velocity field.

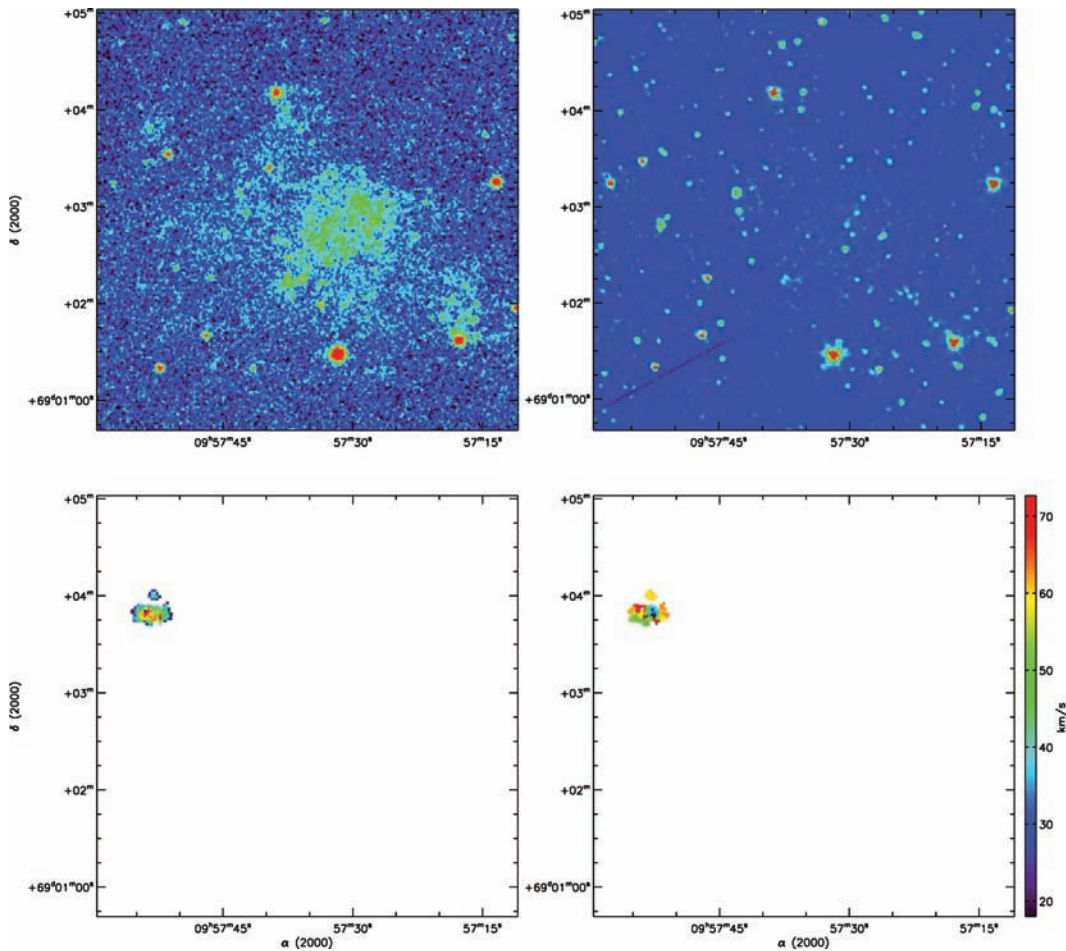


**Figure B15.** Holmberg IX. Top left-hand panel: DSS blue-band image. Top right-hand panel: *Spitzer* IRAC 3.6- $\mu$ m image. Bottom left-hand panel: H $\alpha$  integrated map. Bottom right-hand panel: H $\alpha$  velocity field.

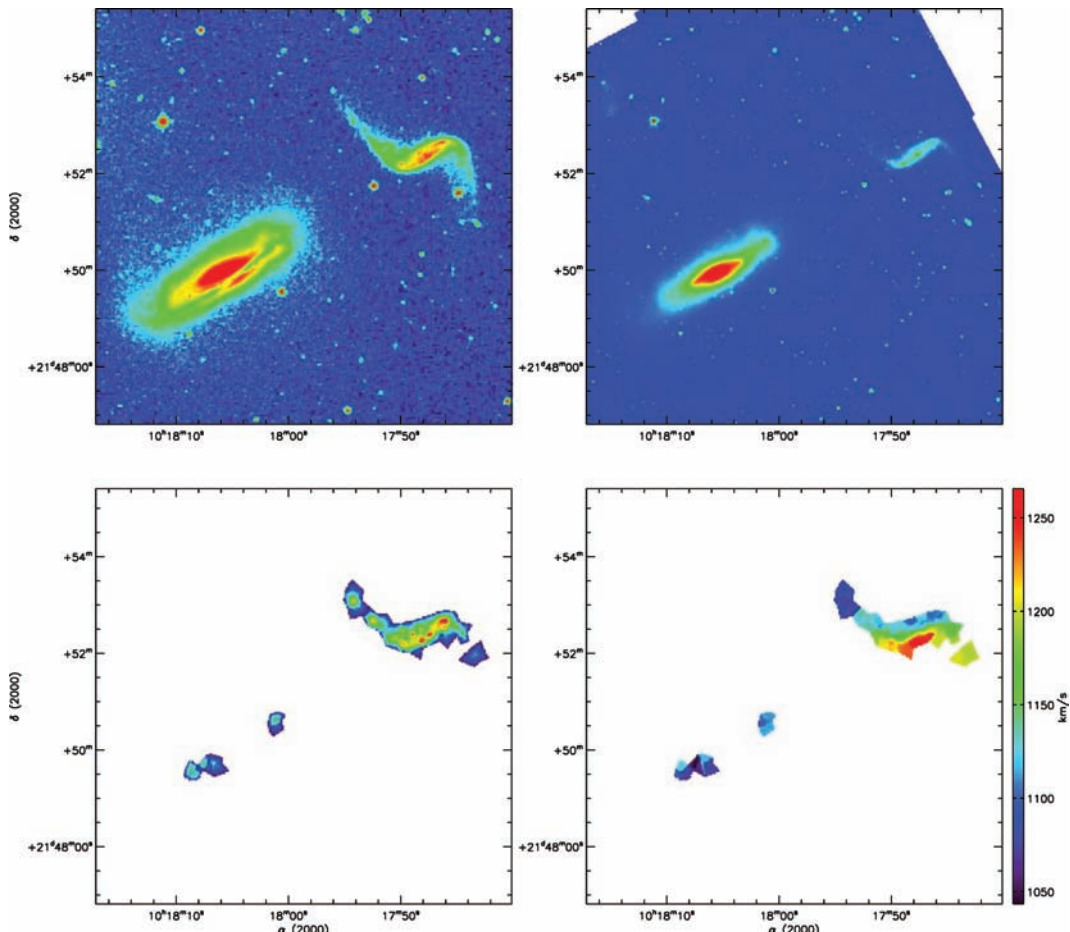


**Figure B16.** NGC 3190 (left-hand panels) with NGC 3187 (right-hand panels). Top left-hand panel: DSS blue-band image. Top right-hand panel: *Spitzer* IRAC 3.6- $\mu$ m image. Bottom left-hand panel: H $\alpha$  integrated map. Bottom right-hand panel: H $\alpha$  velocity field.

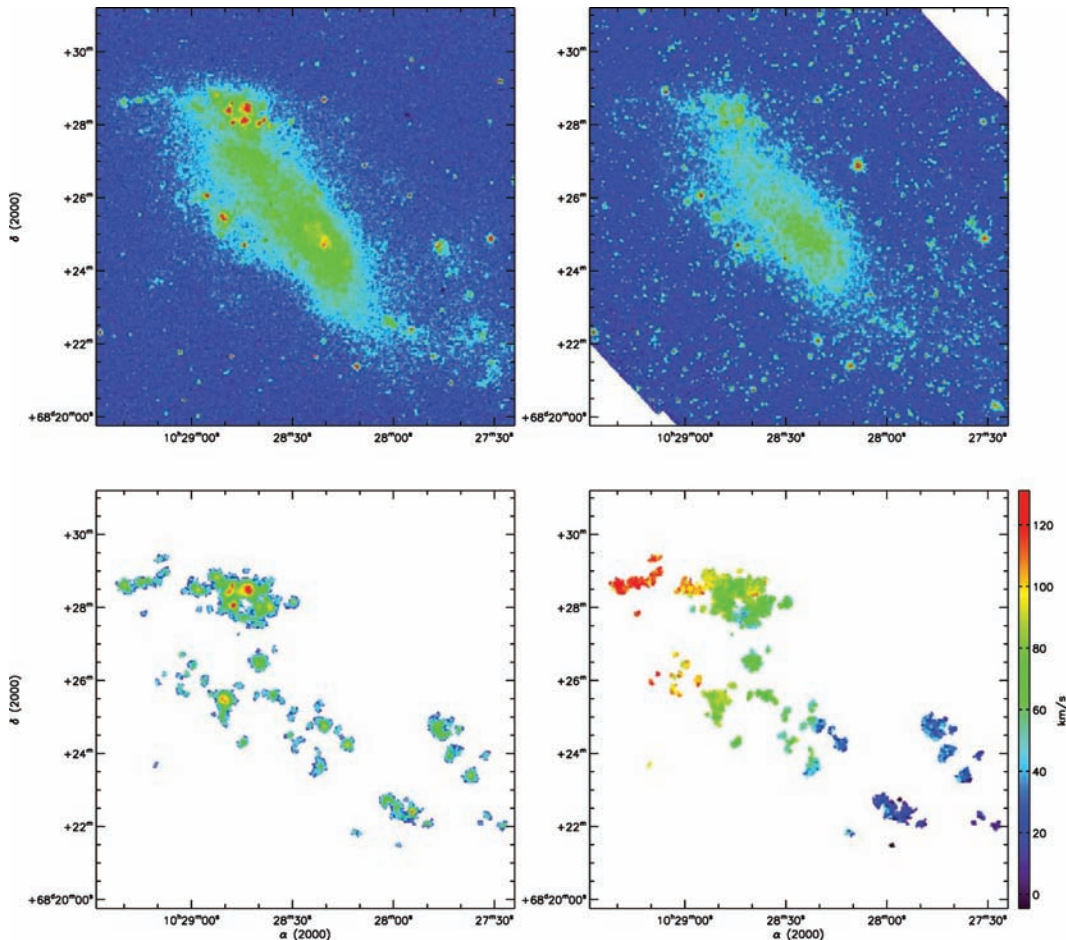


**Figure B17.** IC 2574. Top left-hand panel: DSS blue-band image. Top right-hand panel: *Spitzer* IRAC 3.6- $\mu$ m image. Bottom left-hand panel: H $\alpha$  integrated map. Bottom right-hand panel: H $\alpha$  velocity field.

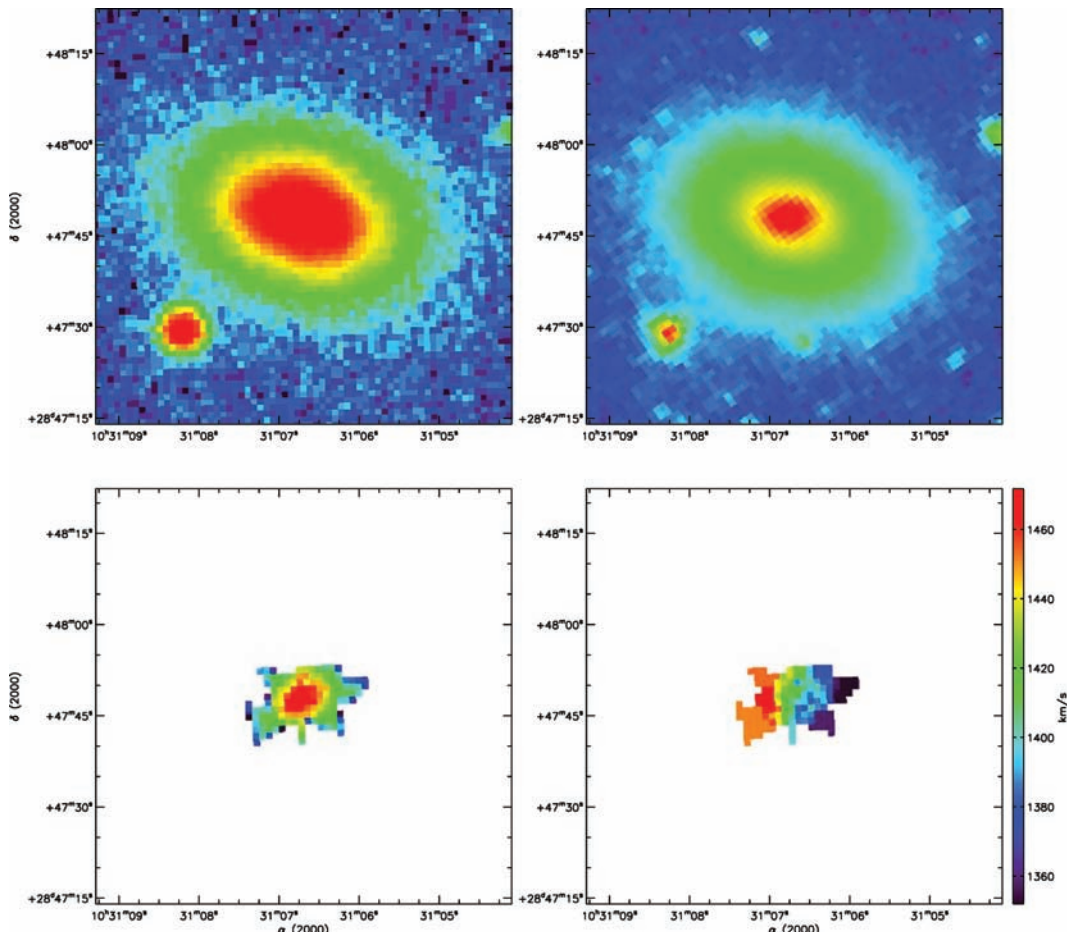


**Figure B18.** NGC 3265. Top left-hand panel: DSS blue-band image. Top right-hand panel: *Spitzer* IRAC 3.6- $\mu$ m image. Bottom left-hand panel: H $\alpha$  integrated map. Bottom right-hand panel: H $\alpha$  velocity field.

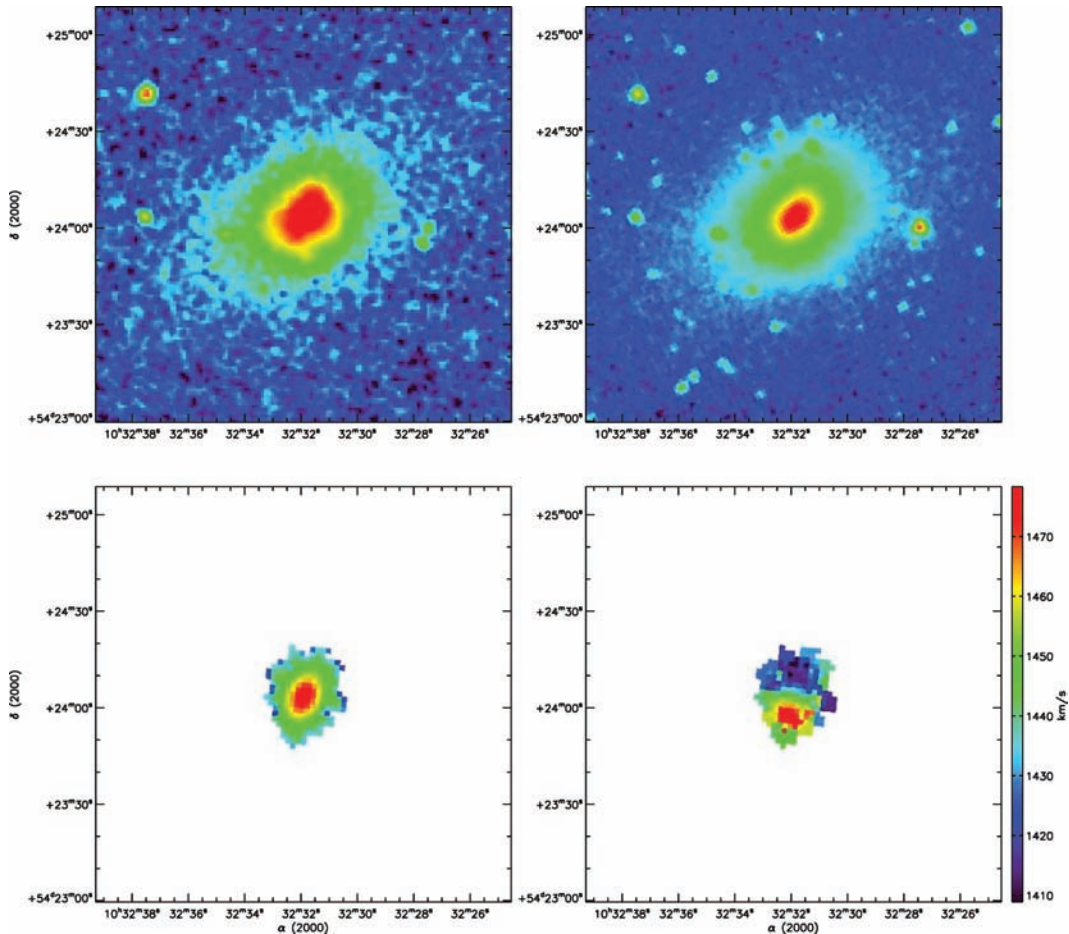


**Figure B19.** Mrk 33. Top left-hand panel: DSS blue-band image. Top right-hand panel: *Spitzer* IRAC 3.6- $\mu$ m image. Bottom left-hand panel: H $\alpha$  integrated map. Bottom right-hand panel: H $\alpha$  velocity field.

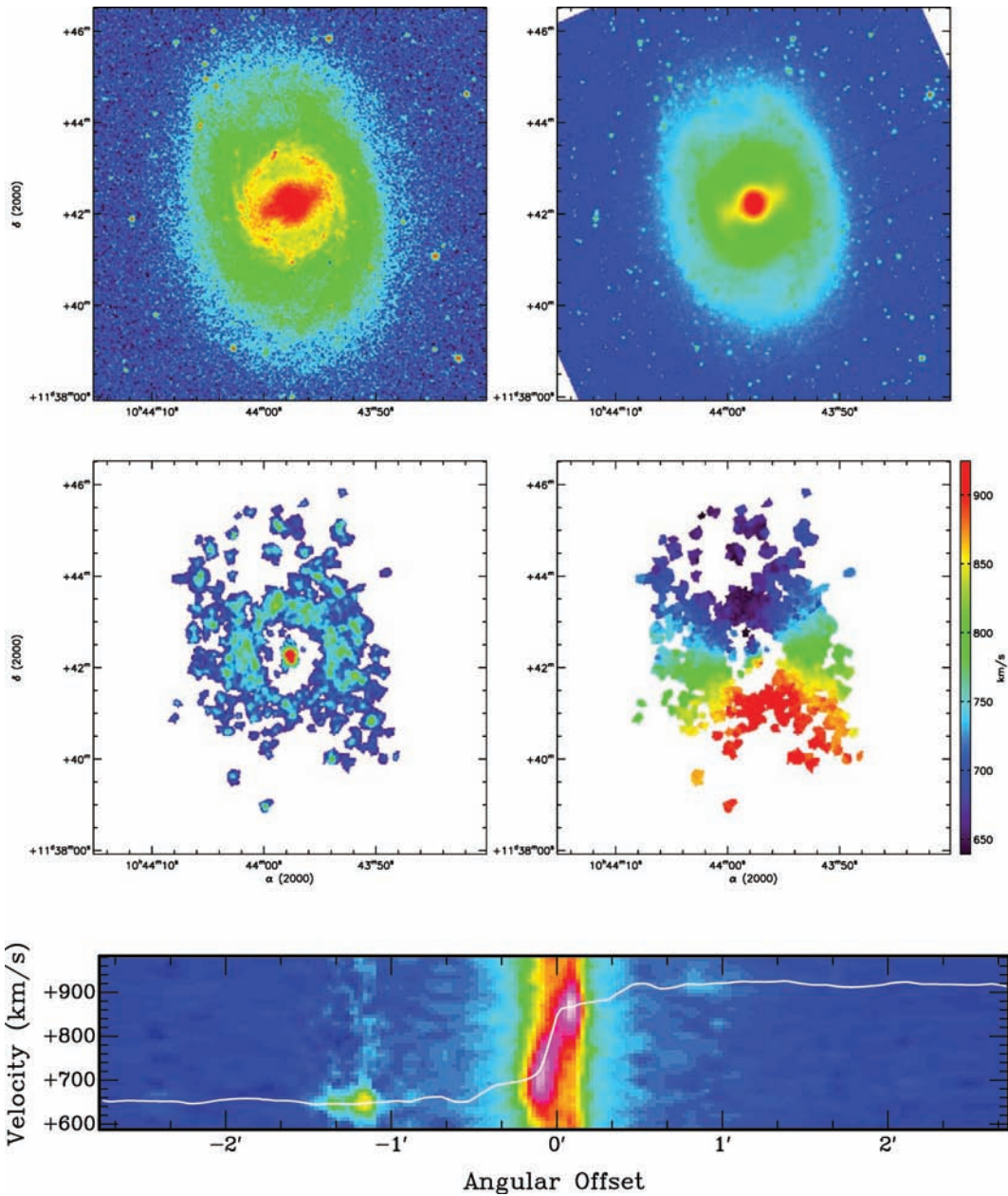


**Figure B20.** NGC 3351. Top left-hand panel: DSS blue-band image. Top right-hand panel: *Spitzer* IRAC 3.6-μm image. Middle left-hand panel:  $H\alpha$  integrated map. Middle right-hand panel:  $H\alpha$  velocity field. Bottom: PV diagram.

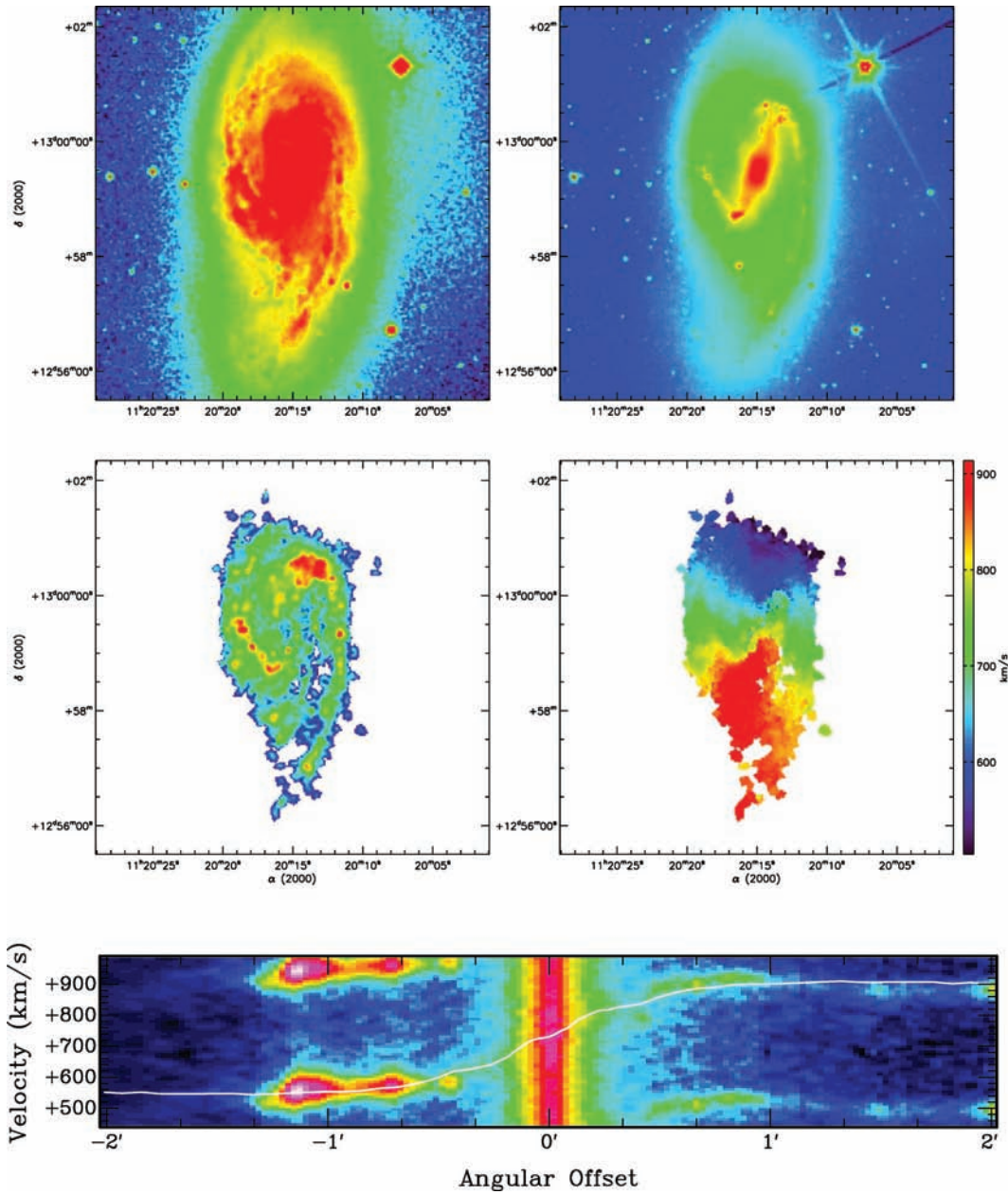


**Figure B21.** NGC 3627. Top left-hand panel: DSS blue-band image. Top right-hand panel: *Spitzer* IRAC 3.6-μm image. Middle left-hand panel:  $\text{H}\alpha$  integrated map. Middle right-hand panel:  $\text{H}\alpha$  velocity field. Bottom: PV diagram.

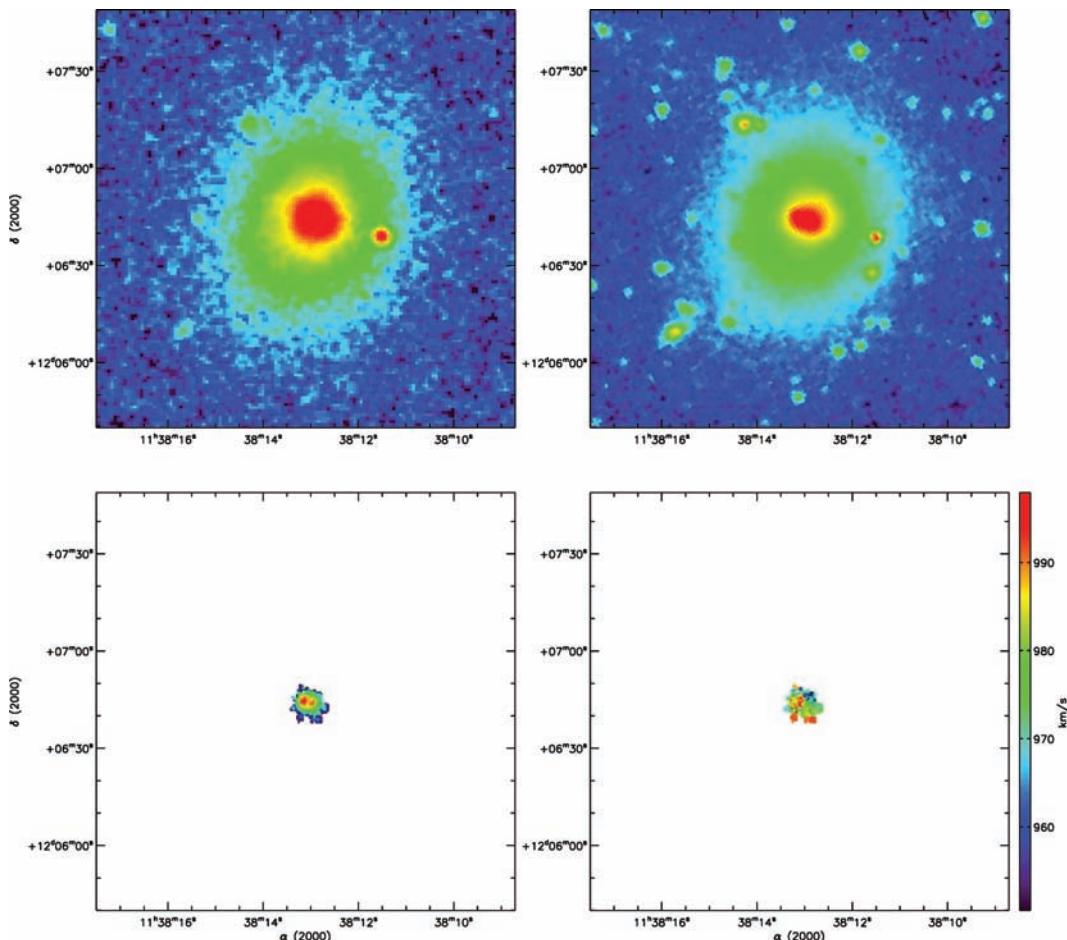


**Figure B22.** NGC 3773. Top left-hand panel: DSS blue-band image. Top right-hand panel: *Spitzer* IRAC 3.6- $\mu\text{m}$  image. Bottom left-hand panel:  $\text{H}\alpha$  integrated map. Bottom right-hand panel:  $\text{H}\alpha$  velocity field.

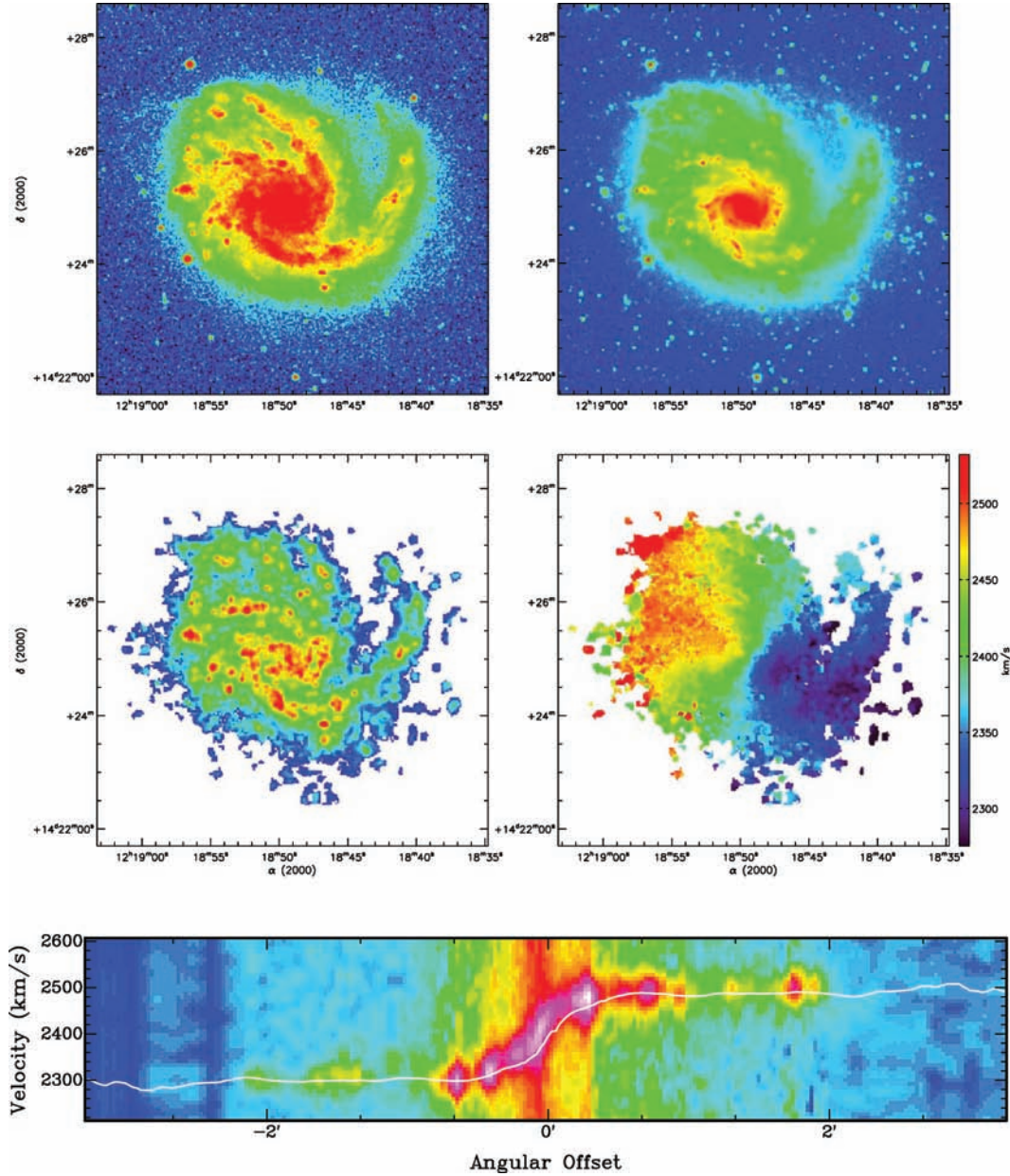


**Figure B23.** NGC 4254. Top left-hand panel: DSS blue-band image. Top right-hand panel: *Spitzer* IRAC 3.6- $\mu$ m image. Middle left-hand panel: H $\alpha$  integrated map. Middle right-hand panel: H $\alpha$  velocity field. Bottom: PV diagram.

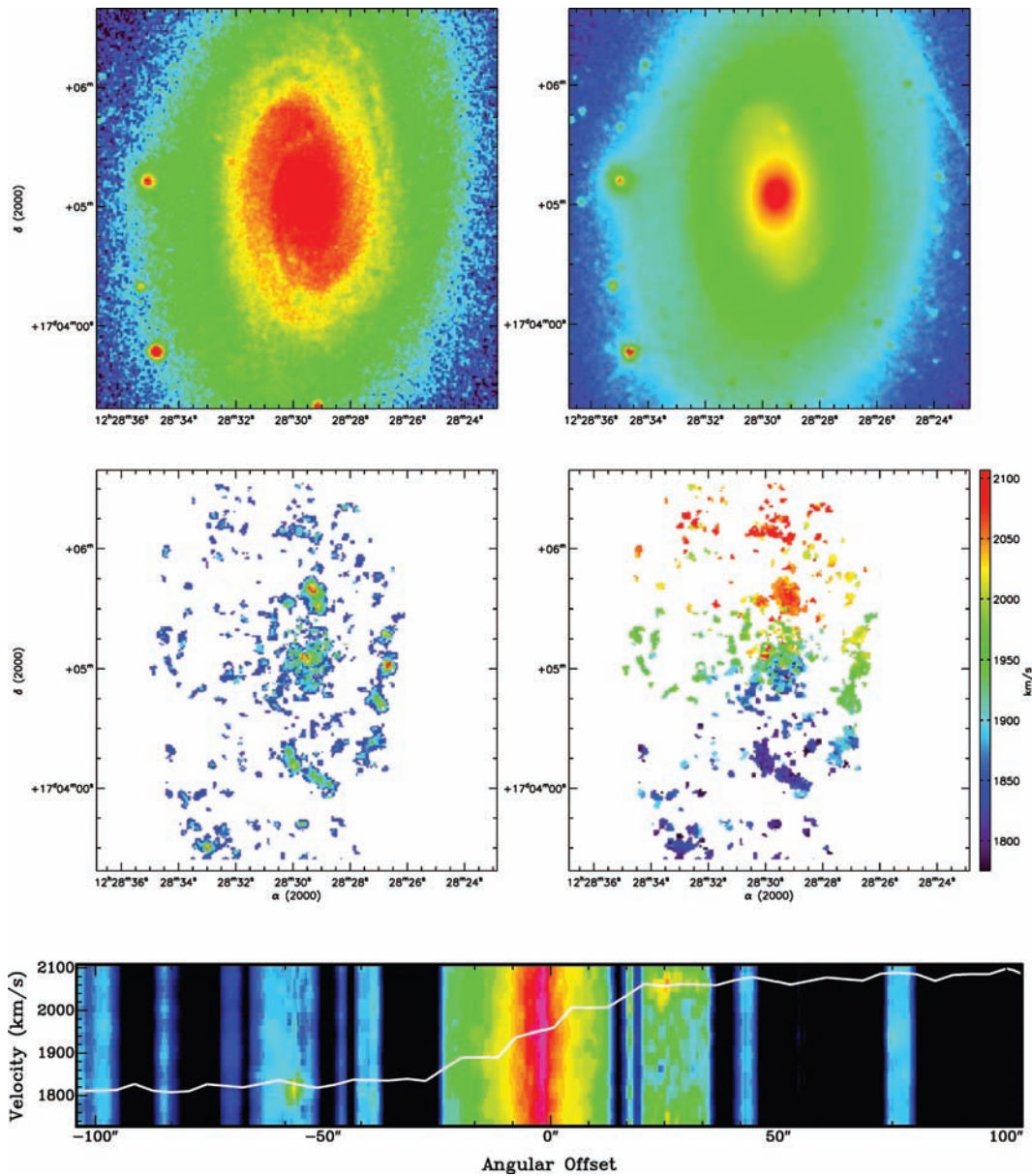


**Figure B24.** NGC 4450. Top left-hand panel: DSS blue-band image. Top right-hand panel: *Spitzer* IRAC 3.6-μm image. Middle left-hand panel: *H $\alpha$*  integrated map. Middle right-hand panel: *H $\alpha$*  velocity field. Bottom: PV diagram.

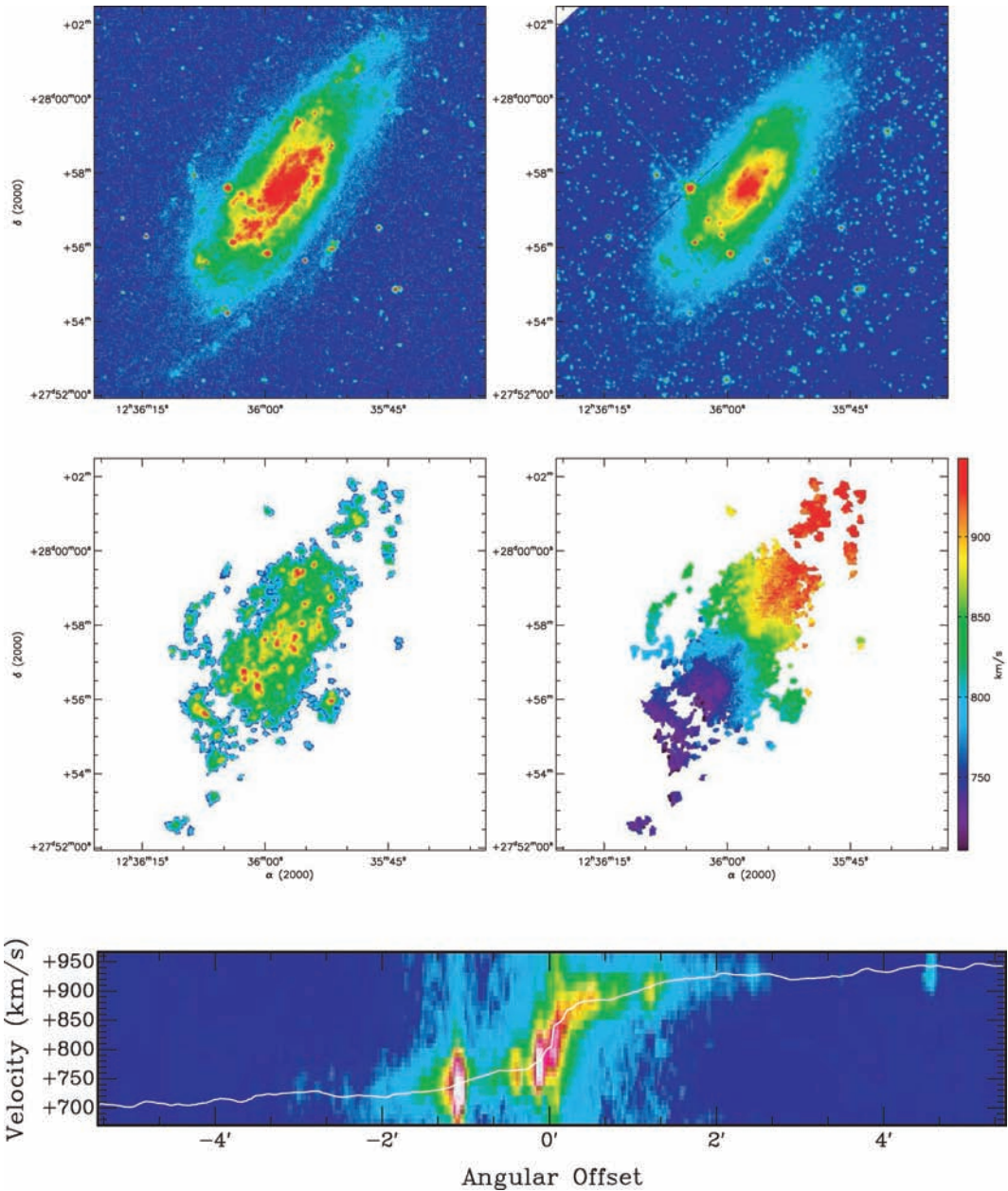


**Figure B25.** NGC 4559. Top left-hand panel: DSS blue-band image. Top right-hand panel: *Spitzer* IRAC 3.6- $\mu$ m image. Middle left-hand panel:  $H\alpha$  integrated map. Middle right-hand panel:  $H\alpha$  velocity field. Bottom: PV diagram.

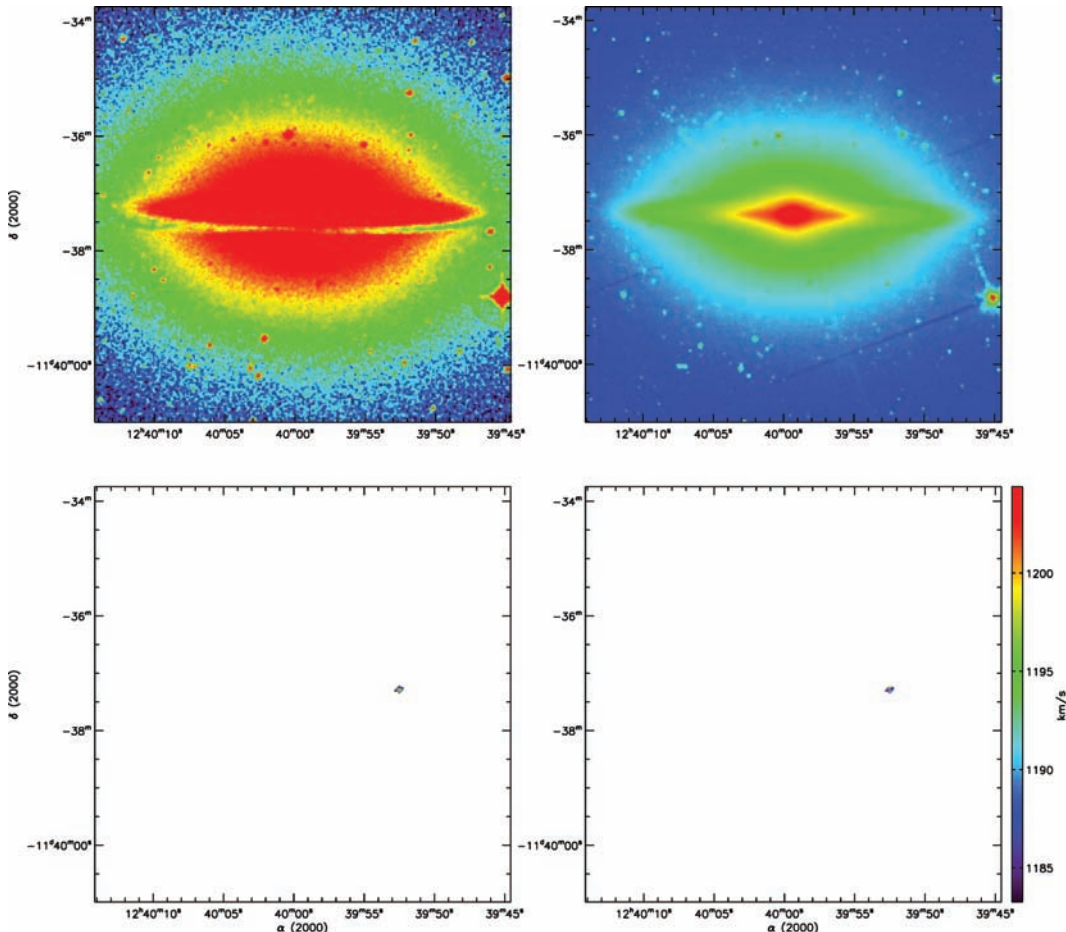


**Figure B26.** NGC 4594. Top left-hand panel: DSS blue-band image. Top right-hand panel: *Spitzer* IRAC 3.6- $\mu$ m image. Bottom left-hand panel: H $\alpha$  integrated map. Bottom right-hand panel: H $\alpha$  velocity field.

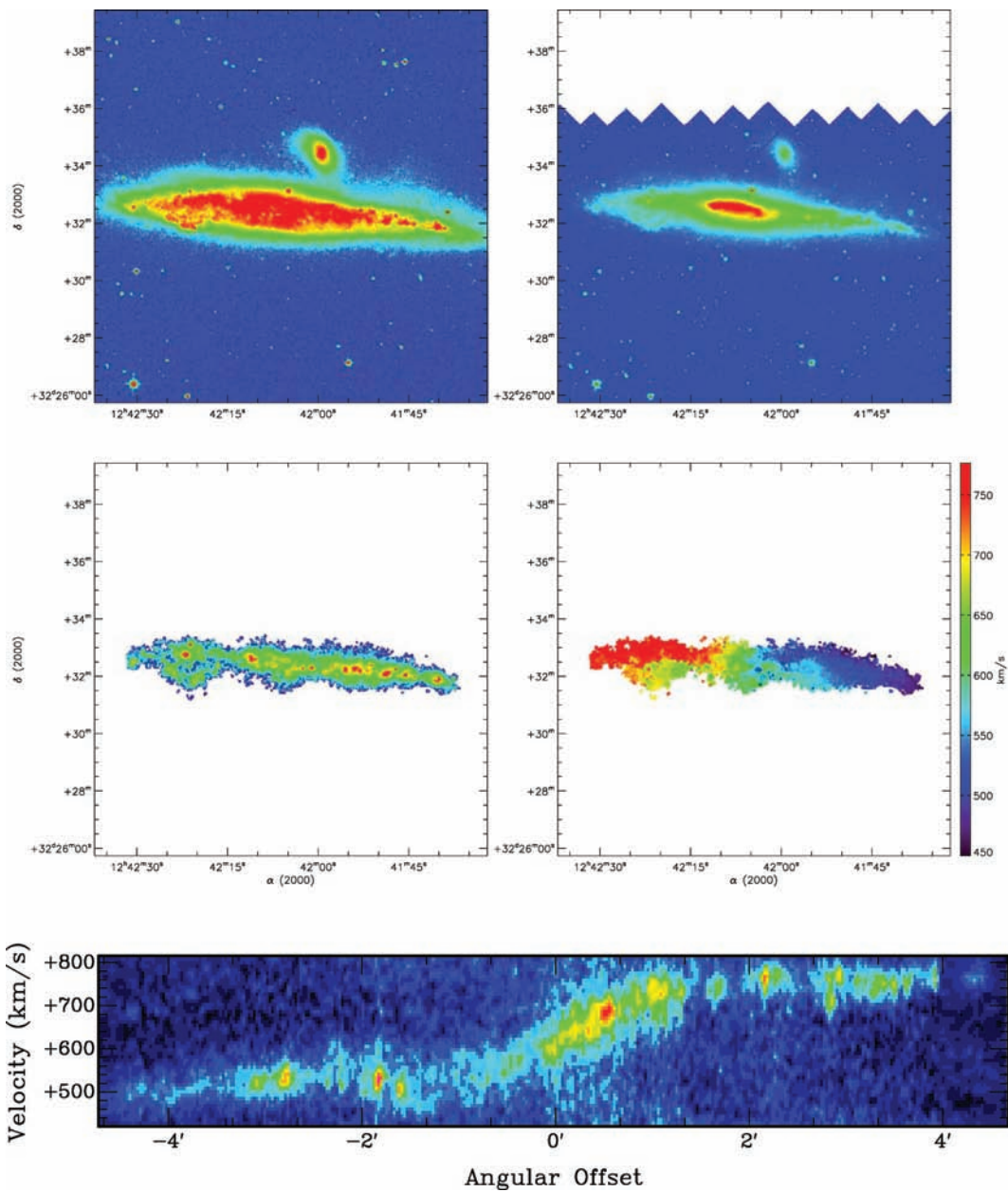


**Figure B27.** NGC 4631. Top left-hand panel: DSS blue-band image. Top right-hand panel: *Spitzer* IRAC 3.6- $\mu$ m image. Bottom left-hand panel: H $\alpha$  integrated map. Bottom right-hand panel: H $\alpha$  velocity field. Bottom: PV diagram.

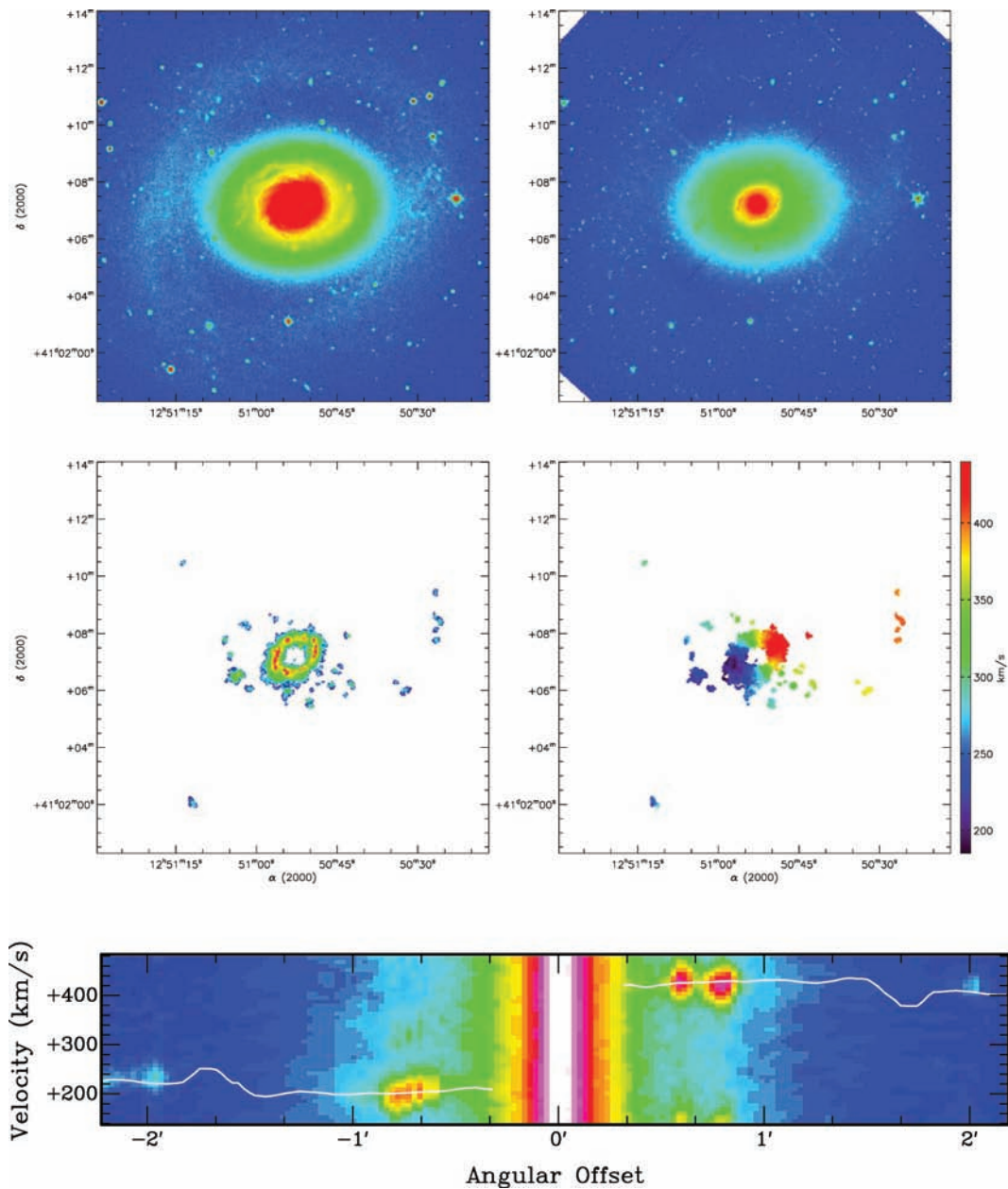


**Figure B28.** NGC 4736. Top left-hand panel: DSS blue-band image. Top right-hand panel: *Spitzer* IRAC 3.6-μm image. Middle left-hand panel: H $\alpha$  integrated map. Middle right-hand panel: H $\alpha$  velocity field. Bottom: PV diagram.

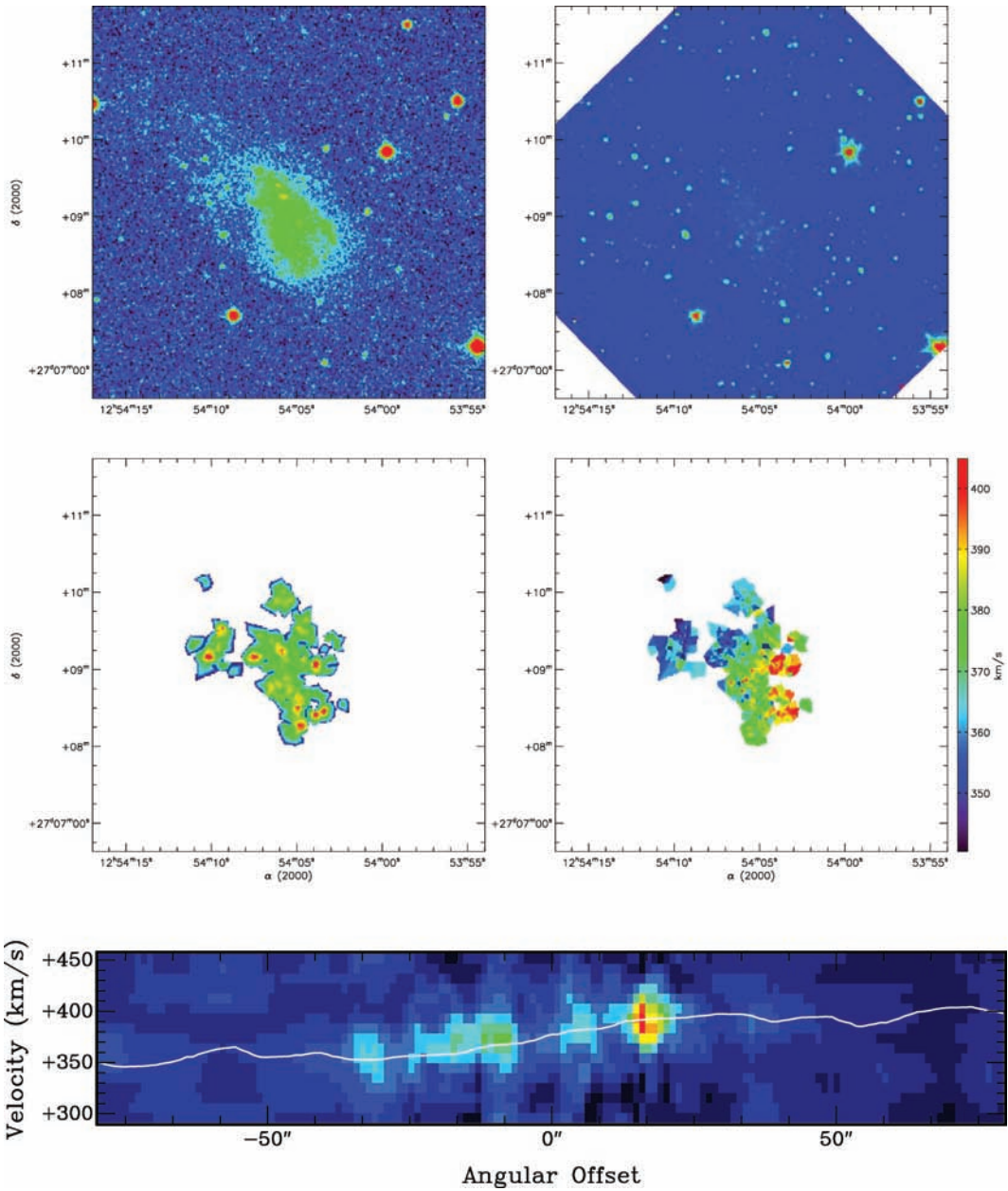


**Figure B29.** DDO 154. Top left-hand panel: DSS blue-band image. Top right-hand panel: *Spitzer* IRAC 3.6- $\mu\text{m}$  image. Middle left-hand panel:  $\text{H}\alpha$  integrated map. Middle right-hand panel:  $\text{H}\alpha$  velocity field. Bottom: PV diagram.

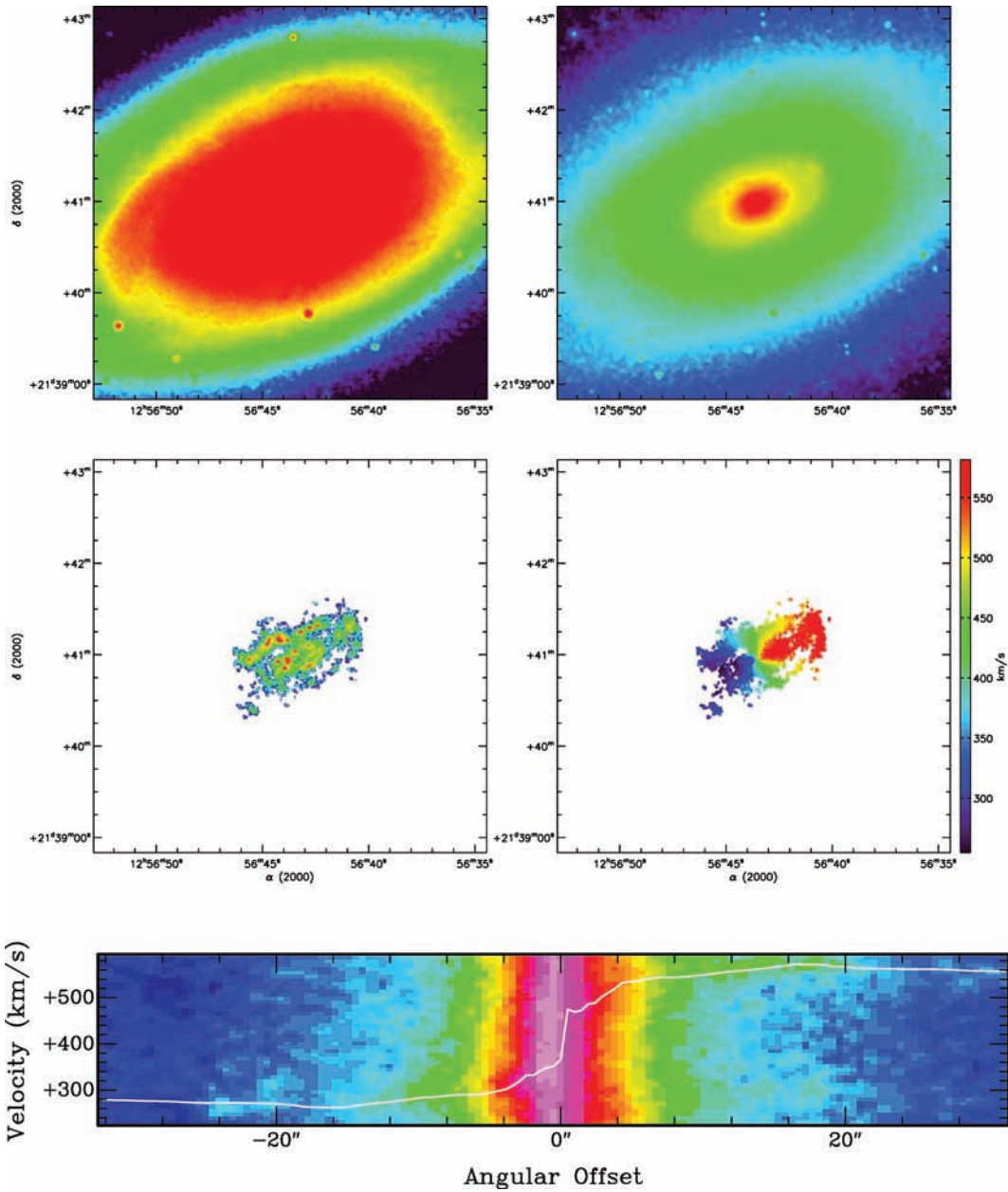


**Figure B30.** NGC 4826. Top left-hand panel: DSS blue-band image. Top right-hand panel: *Spitzer* IRAC 3.6- $\mu\text{m}$  image. Middle left-hand panel:  $\text{H}\alpha$  integrated map. Middle right-hand panel:  $\text{H}\alpha$  velocity field. Bottom: PV diagram.

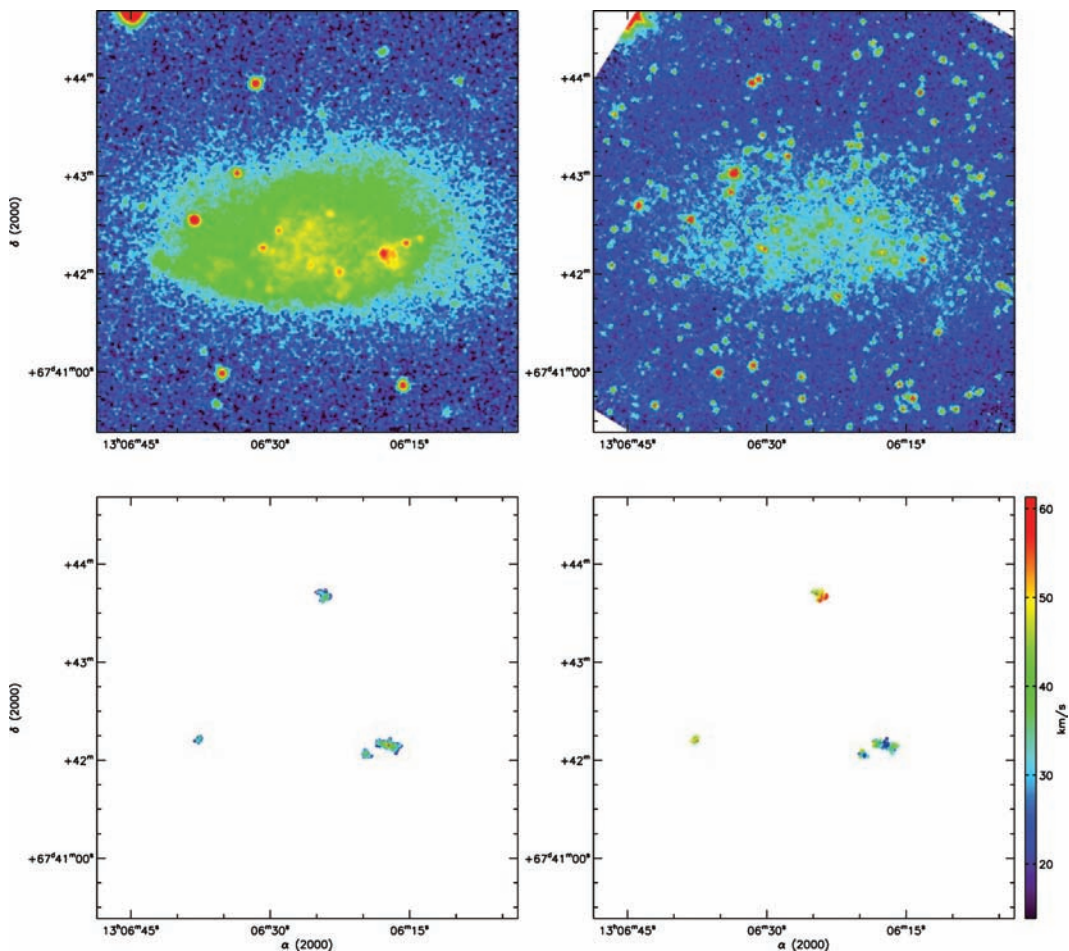


**Figure B31.** DDO 165. Top left-hand panel: DSS blue-band image. Top right-hand panel: *Spitzer* IRAC 3.6- $\mu$ m image. Bottom left-hand panel:  $H\alpha$  integrated map. Bottom right-hand panel:  $H\alpha$  velocity field.

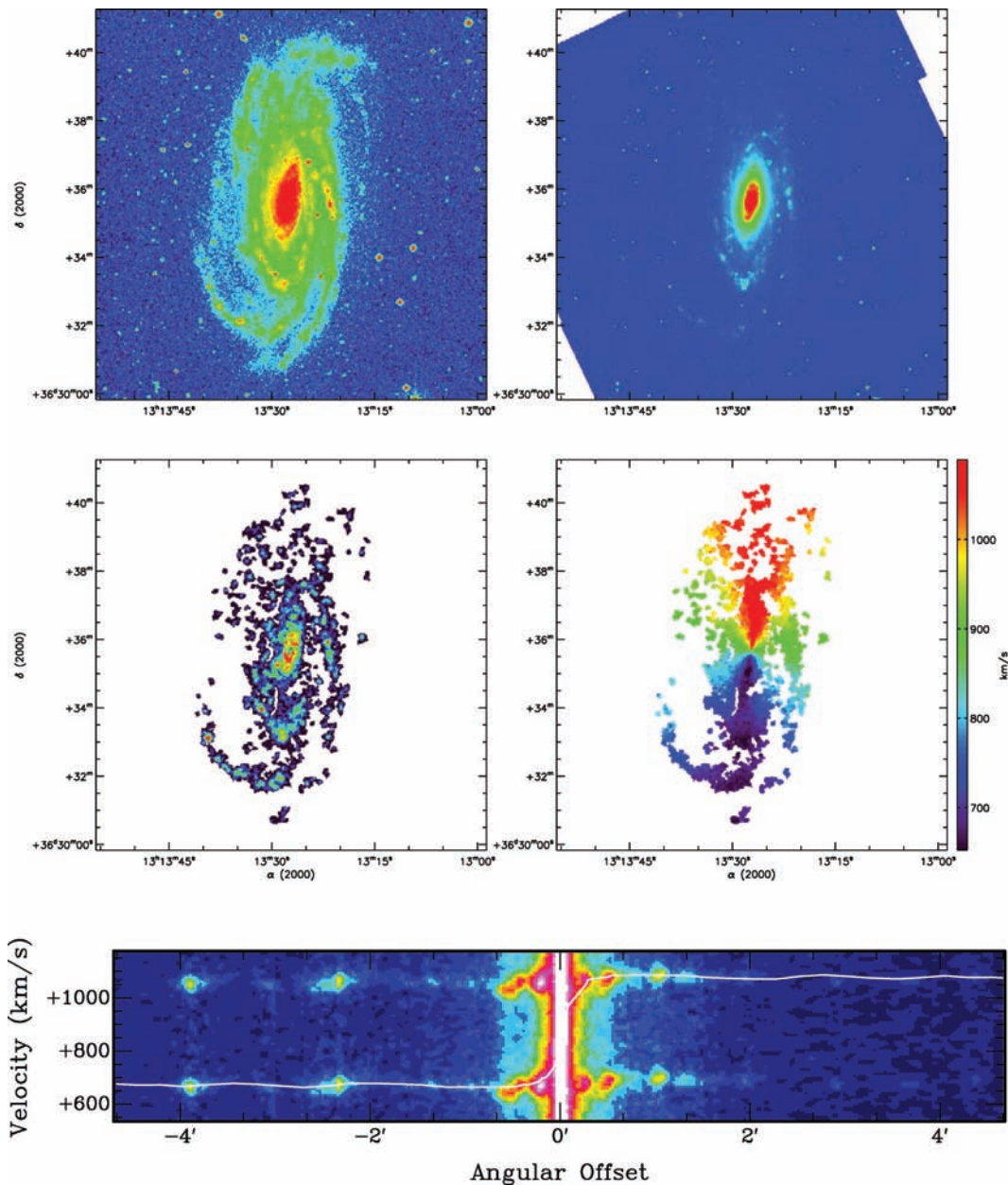


**Figure B32.** NGC 5033. Top left-hand panel: DSS blue-band image. Top right-hand panel: *Spitzer* IRAC 3.6-μm image. Middle left-hand panel:  $\text{H}\alpha$  integrated map. Middle right-hand panel:  $\text{H}\alpha$  velocity field. Bottom: PV diagram.

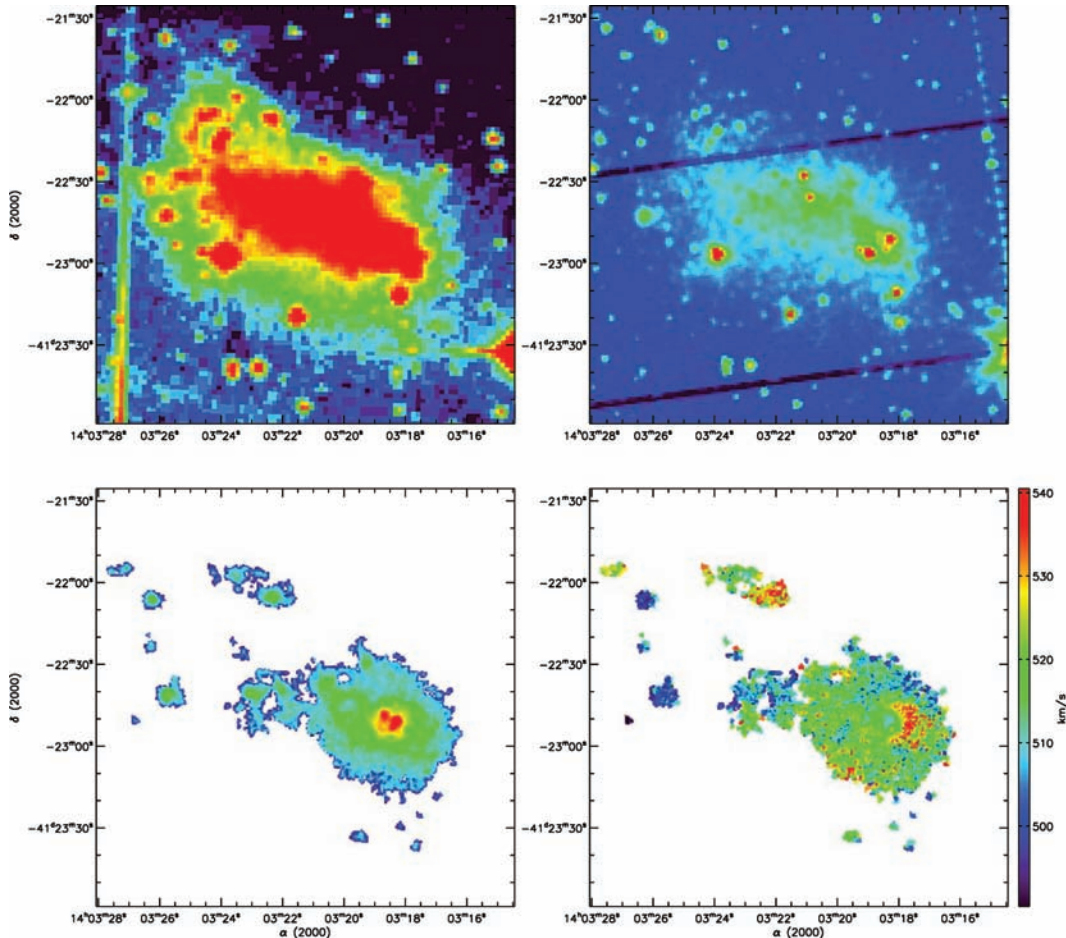


**Figure B33.** NGC 5408. Top left-hand panel: DSS blue-band image. Top right-hand panel: *Spitzer* IRAC 3.6- $\mu$ m image. Bottom left-hand panel: H $\alpha$  integrated map. Bottom right-hand panel: H $\alpha$  velocity field.

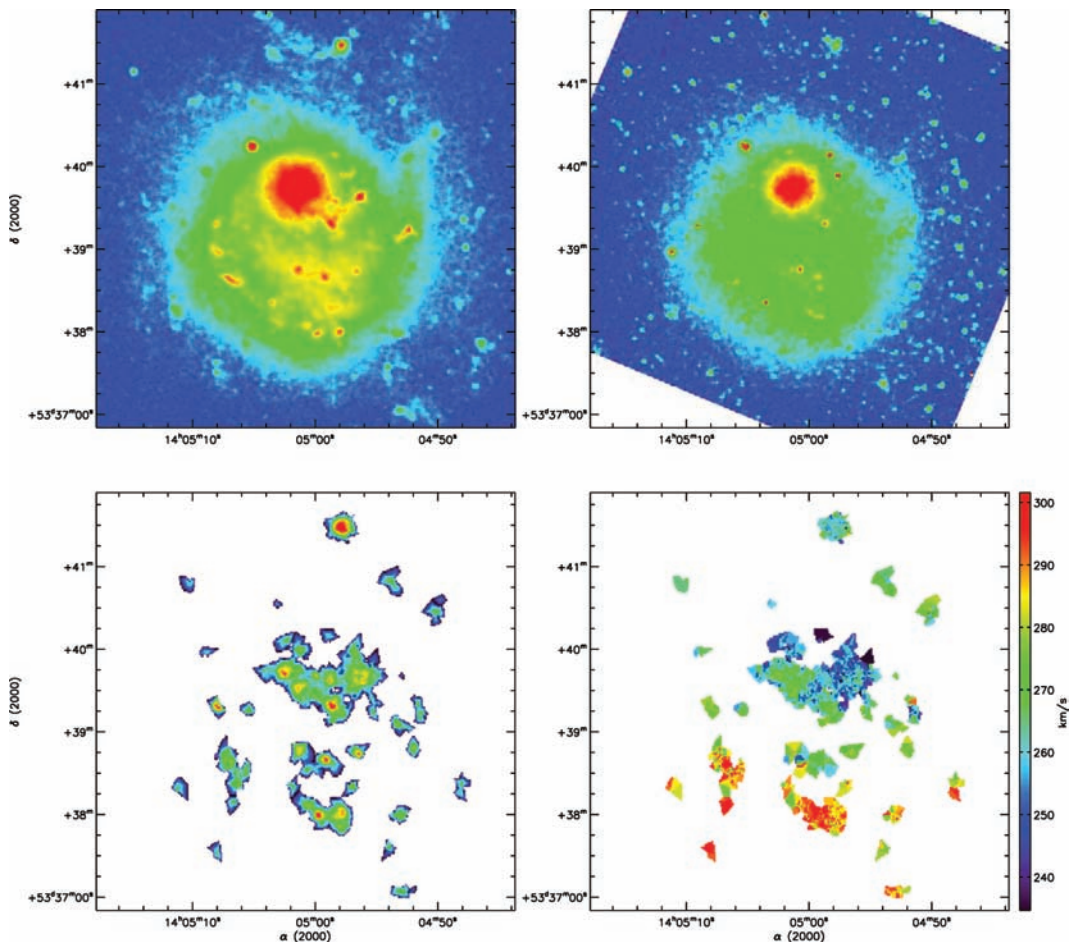


**Figure B34.** NGC 5474. Top left-hand panel: DSS blue-band image. Top right-hand panel: *Spitzer* IRAC 3.6- $\mu\text{m}$  image. Bottom left-hand panel:  $\text{H}\alpha$  integrated map. Bottom right-hand panel:  $\text{H}\alpha$  velocity field.

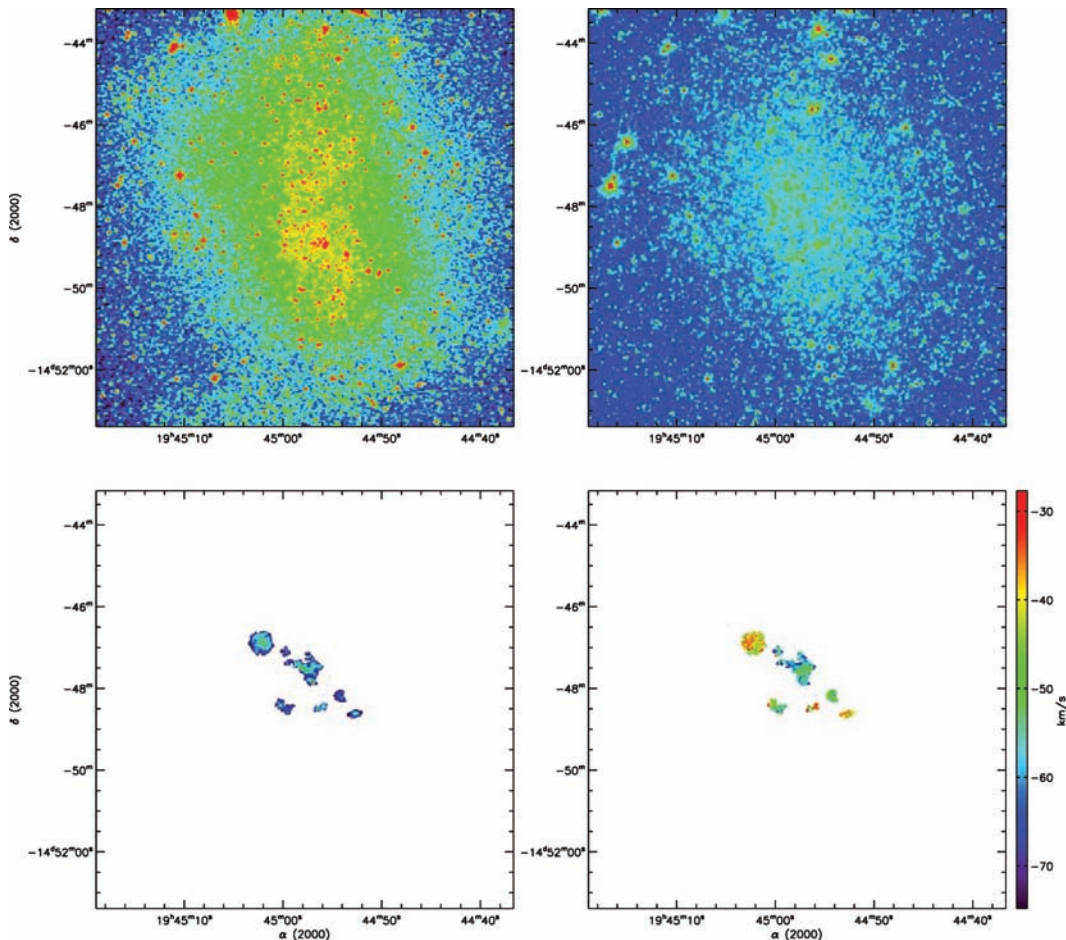


**Figure B35.** NGC 6822. Top left-hand panel: DSS blue-band image. Top right-hand panel: *Spitzer* IRAC 3.6- $\mu$ m image. Bottom left-hand panel: H $\alpha$  integrated map. Bottom right-hand panel: H $\alpha$  velocity field.

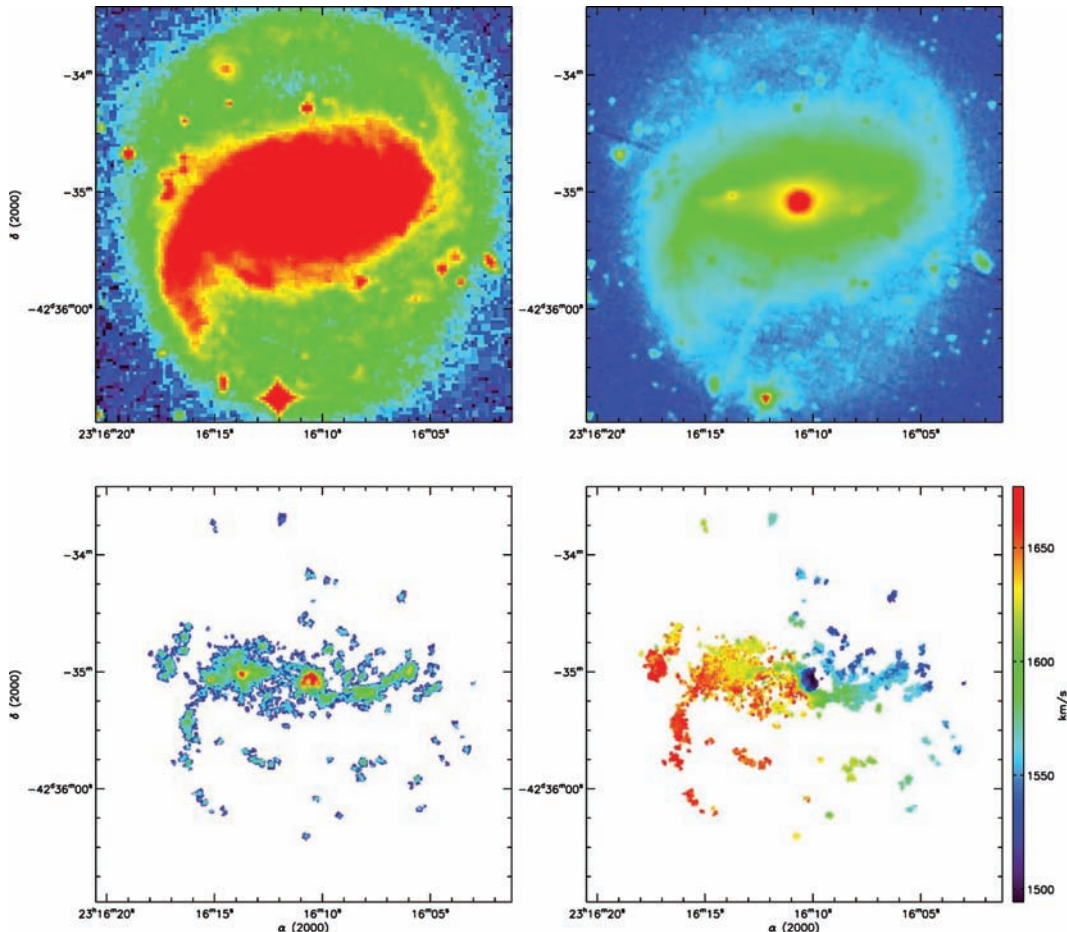


**Figure B36.** NGC 7552. Top left-hand panel: DSS blue-band image. Top right-hand panel: *Spitzer* IRAC 3.6- $\mu\text{m}$  image. Bottom left-hand panel:  $\text{H}\alpha$  integrated map. Bottom right-hand panel:  $\text{H}\alpha$  velocity field.

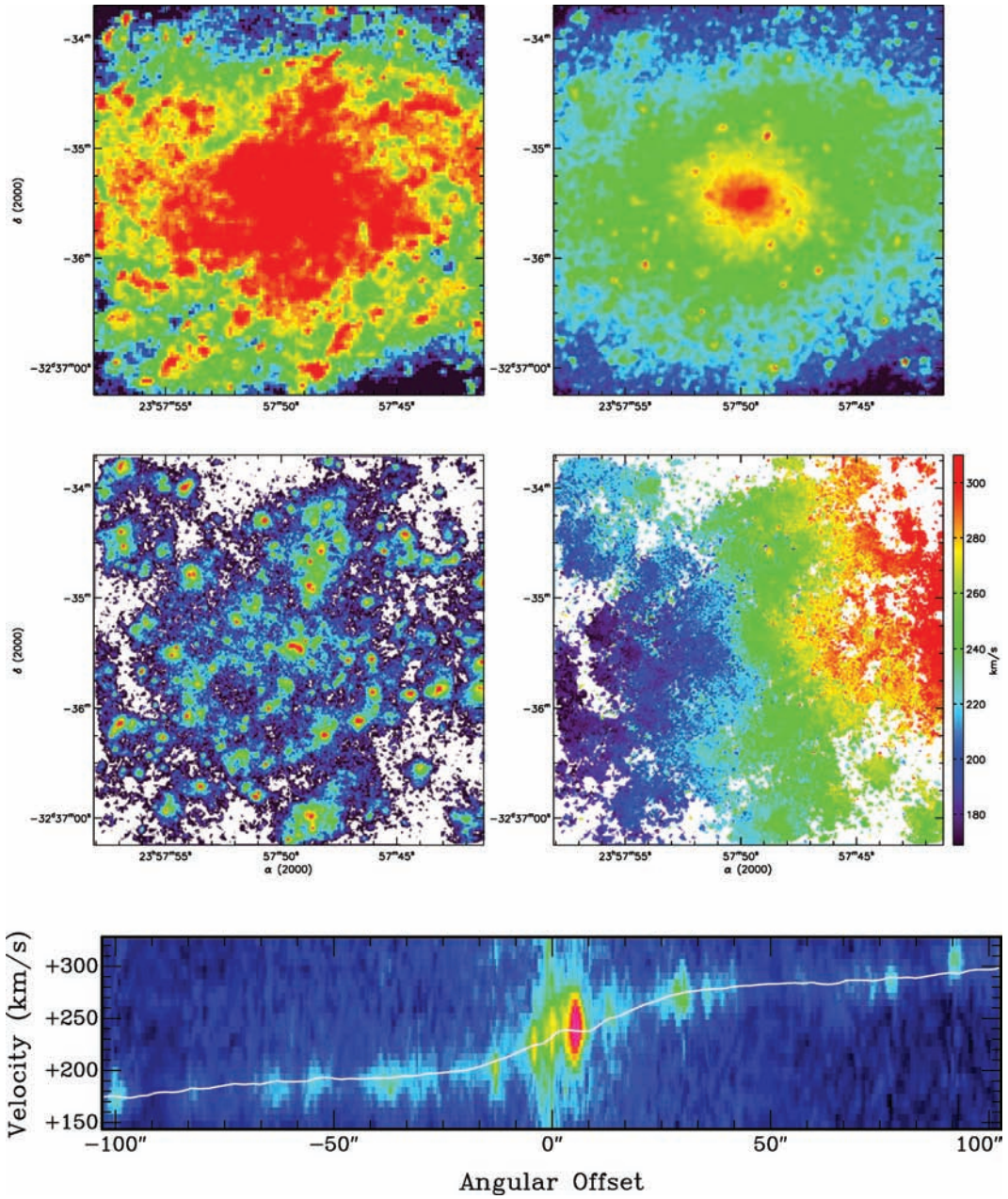


**Figure B37.** NGC 7793. Top left-hand panel: DSS blue-band image. Top right-hand panel: *Spitzer* IRAC 3.6- $\mu$ m image. Middle left-hand panel: H $\alpha$  integrated map. Middle right-hand panel: H $\alpha$  velocity field. Bottom: PV diagram.

## APPENDIX C: ROTATION CURVES

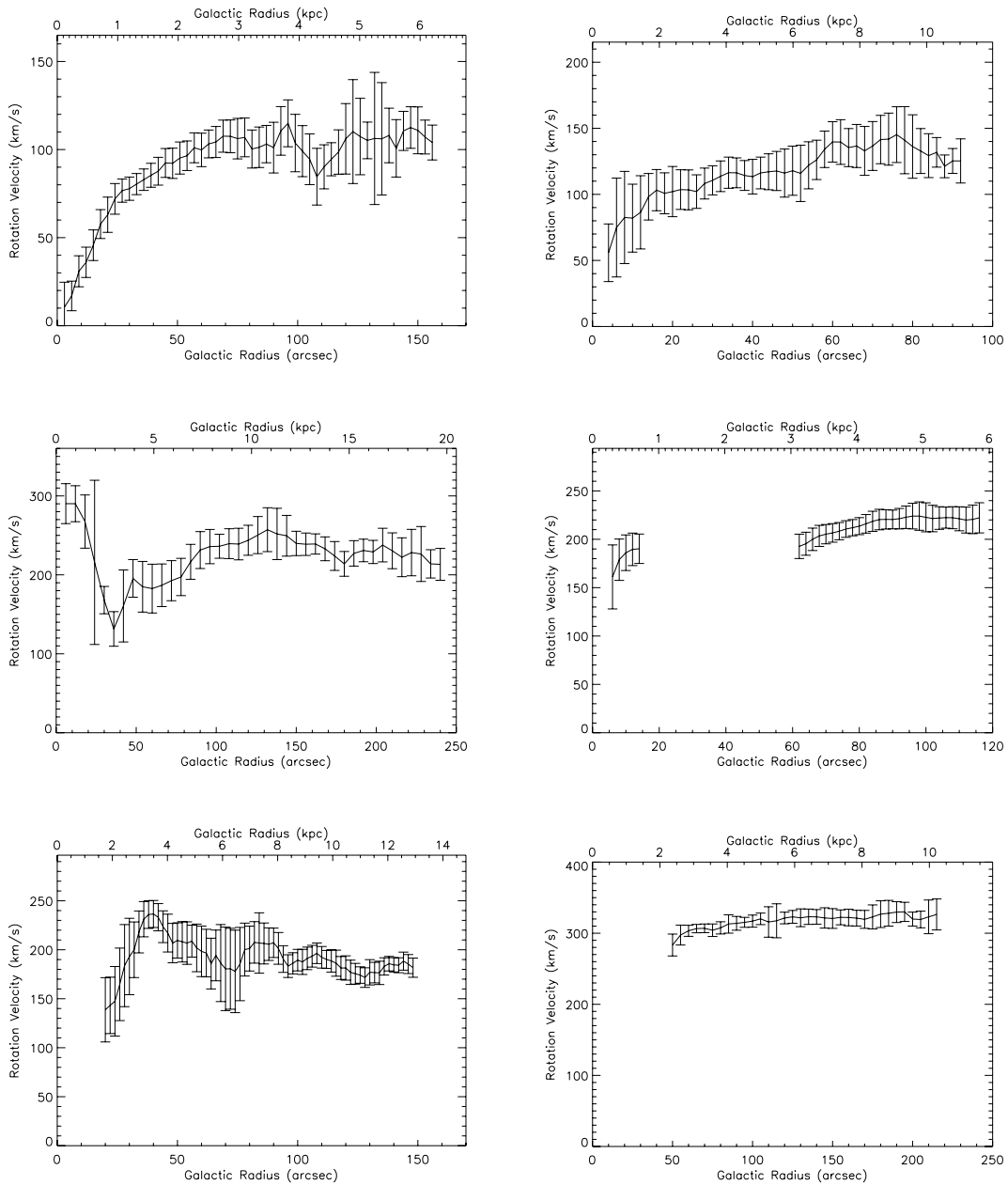


**Figure C1.** Rotation curves for the galaxies NGC 24 (top left-hand panel: PA = 226°,  $i$  = 75°), NGC 337 (top right-hand panel: PA = 121°,  $i$  = 52°), NGC 1097 (middle left-hand panel: PA = 133°,  $i$  = 55°), NGC 1512 (middle right-hand panel: PA = 260°,  $i$  = 35°), NGC 1566 (bottom left-hand panel: PA = 214°,  $I$  = 32°) and NGC 2841 (bottom right-hand panel: PA = 150°,  $i$  = 70°).

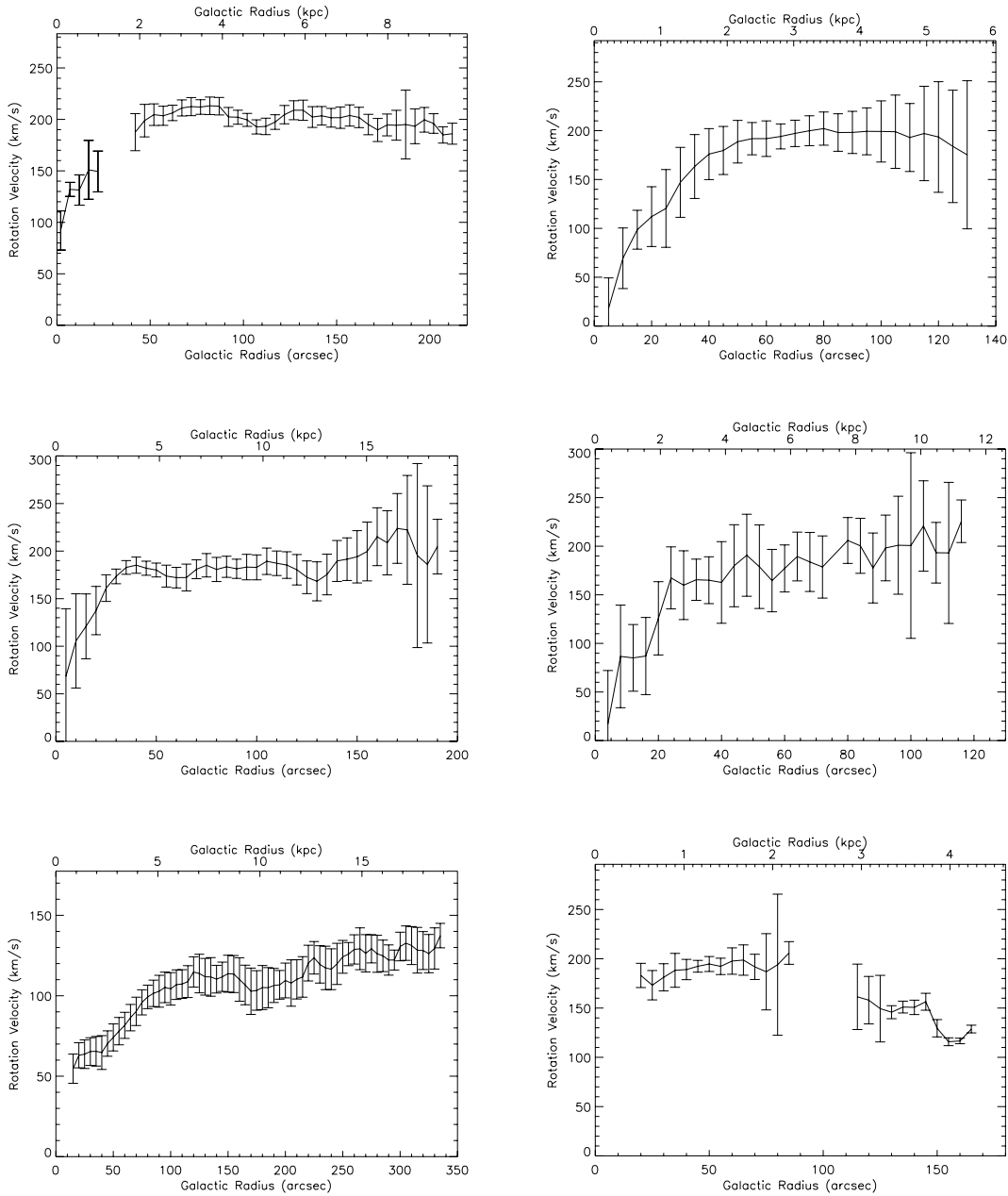


**Figure C2.** Rotation curves for the galaxies NGC 3351 (top left-hand panel: PA =  $193^\circ$ ,  $i = 41^\circ$ ), NGC 3627 (top right-hand panel: PA =  $173^\circ$ ,  $i = 65^\circ$ ), NGC 4254 (middle left-hand panel: PA =  $69^\circ$ ,  $i = 31^\circ$ ), NGC 4450 (middle right-hand panel: PA =  $353^\circ$ ,  $i = 43^\circ$ ), NGC 4559 (bottom left-hand panel: PA =  $323^\circ$ ,  $i = 68^\circ$ ) and NGC 4736 (bottom right-hand panel: PA =  $292^\circ$ ,  $i = 36^\circ$ ).

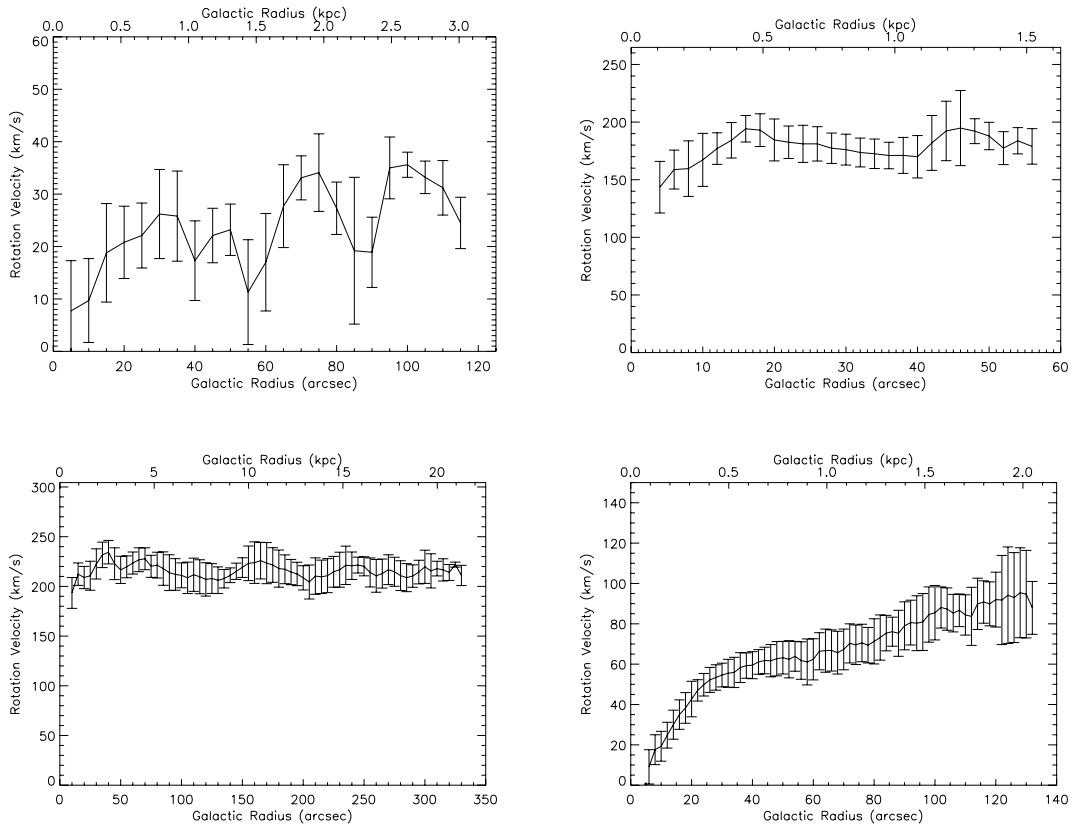


**Figure C3.** Rotation curves for the galaxies DDO 154 (top left-hand panel:  $PA = 236^\circ, i = 59^\circ$ ), NGC 4826 (top right-hand panel:  $PA = 291^\circ, i = 53^\circ$ ), NGC 5033 (bottom left-hand panel:  $PA = 353^\circ, i = 71^\circ$ ) and NGC 7793 (bottom right-hand panel:  $PA = 277^\circ, i = 47^\circ$ ).

This paper has been typeset from a TeX/LaTeX file prepared by the author.